SILICON PHOTONIC MICRORING RESONATORS FOR THE DEVELOPMENT OF CANCER PROTEIN BIOMARKER ASSAYS

BY

ADAM L. WASHBURN

DISSERTATION

Submitted in partial fulfillment of the requirements
for the degree of Doctor of Philosophy in Chemistry
in the Graduate College of the
University of Illinois at Urbana-Champaign, 2012

Urbana, Illinois

Doctoral Committee:

Professor Ryan C. Bailey, Chair
Professor John A. Katzenellenbogen
Professor Alexander Scheeline
Professor Jonathan V. Sweedler

Abstract

Although often referred to as simply "cancer," uncontrolled cell growth and division in a human body is often the result of a variety of biochemical perturbations. Efforts to improve diagnosis and treatment of cancer patients are increasingly relying upon more detailed individual biochemical information—i.e. a "personalized medicine" approach. One method to ascertain individual biochemical conditions is by measuring the levels of certain proteins in the blood stream, commonly referred to as cancer biomarkers. Traditional quantitative methods for biomarker analysis have typically relied on a single biomarker to provide information. However, single biomarker analyses have proven to be woefully incomplete in the information content needed for a personalized medical diagnosis. Multiplexed biomarker panels have the potential to overcome the limitations of single biomarker analysis due to the greater information content present in a panel of biomarkers, but technologies to rapidly, accurately, and reproducibly make multiplexed measurements, especially in a quantitative manner, are as yet undeveloped.

This doctoral dissertation presents the development of silicon photonic microring resonator technology in the Ryan Bailey research laboratory towards multiplexed cancer protein biomarker measurements. Microring resonator sensing technology relies upon changes in refractive index that induce a resonance shift in circular silicon waveguides. Taking advantage of standard semiconductor processing techniques and facilities, it has been possible to rapidly develop sensor chips with 32 active sensors with the potential to be scaled even higher. These chips have thus been developed for making multiplexed biomarker measurements.

This dissertation represents the development of microring resonator technology from a novel technology to applied multiplex detection in cancer patient blood serum samples. Chapter 1 introduces more fully the topic of microring resonators, followed by a discussion of the basic physical characteristics, properties, and abilities of the sensors in Chapter 2. Chapter 3 introduces singleplex protein biomarker detection with multiplex detection in buffer following in Chapter 4. Multiplexed capture agent screening, a necessity for multiplexed immunoassays, is covered in Chapter 5 followed by the singleplex detection of a protein biomarker in human serum in Chapter 6. The final work of this project concludes with Chapter 7 which describes the methods used to make multiplex cancer biomarker measurements in human serum.

Table of Contents

Chapter 1

Introduction to Microring Resonators for Multiplex Analysis

Notes and Acknowledgements

Sections 1.1 and 1.2 of this chapter have been adapted from the original paper "Photonics-on-a-Chip: Recent Advances in Integrated Waveguides as Enabling Detection Elements for Real-World, Lab-on-a-Chip Biosensing Applications" (Washburn, A. L.; Bailey, R.C. *Analyst* **2011**, *136*, 227-236). It has been reproduced here with permission from the Royal Society of Chemistry, Copyright © 2011.

The original article can be accessed online at: http://dx.doi.org/10.1039/C0AN00449A

1.1 Introduction to Waveguide-Based Biosensors

By enabling efficient solution transport, mixing, separation, and analysis of small sample volumes on a single integrated fluidic chip, recent advances in microfluidic technologies have made possible the miniaturization and integration of many standard bioanalytical assays.[1] Although many lab-on-a-chip devices feature elegant fluid handling capabilities, the actual process of sample quantitation is often achieved with far less grace, requiring bulky and cumbersome instrumentation which, at some level, diminishes the overall utility of these miniature analytical devices. Of particular relevance are optical detection schemes that, while providing high sensitivity and assay versatility, can require large and expensive microscopy instrumentation.

Over the past several decades, fiber optic probes have been demonstrated as promising tools for chemical and biological sensing within small sample volumes.[2] However, these methods typically remain reliant upon external optical components and their sensitivity is often directly tied to the physical length of the fiber-sample interaction, meaning that ultrasensitive measurements require larger probes that may no longer be amenable to small volume analyses.

Recent advances in microfabrication have enabled high density, chip-scale integration of optical components, such as light sources and photodetectors.[3-9] These devices offer substantial advantages for lab-on-a-chip applications by enabling integration of both fluidic handling and optical analysis onto a single chip. These types of integrated sensing devices have the potential to enable creation of high-density biosensors that can provide rapid, sensitive, and multiplexed measurements in point-of-care diagnostic applications.[10]

While significant advances have been made in the incorporation of light sources and detectors into chip-based analytical platforms, the research work of the Bailey lab and of my doctoral dissertation features another essential element of chip-integrated optical detection: waveguides. Propelled by advances in wafer-scale microfabrication over the past two decades, it is now relatively straightforward to incorporate many hundreds or even thousands of chip-integrated waveguides into a single sensor substrate, and this intrinsic scalability allows researchers to envision high levels of measurement multiplexing within small sample volumes.

Many examples, including several commercial products, exist in which integrated waveguides are used as excitation and/or collection elements for fluorescence-based sensors.[11, 12]

However, our work has primarily focused on chip-integrated biosensors that transduce the presence of a target analyte on the basis of binding-induced changes in the refractive index proximal to the waveguide surface. These types of devices provide promising detection elements for a myriad of biosensing applications, largely due to the fact that they do not require the labeling of any biomolecule, a procedure that can perturb native interactions, as well as increase assay cost and complexity.[13]

The governing physics of waveguide operation and the concept of their utility as an analytical device are quite simple. Due to the contrast in refractive index between the core and cladding of an optical waveguide, light is guided through the device on account of total internal reflection, which generates an evanescent optical field that decays exponentially from the sensor surface. Biomolecular binding events modulate the refractive index contrast and thus attenuate the propagation of light through the waveguide. By monitoring the coupling and/or propagation properties of light through an appropriately modified waveguide, it is possible to construct sensors responsive to target biomolecular analytes of interest. The literature has several examples of refractive index-sensitive, waveguide-based sensors such as grating-coupled,[14-16] interferometric,[17, 18] photonic crystal,[19-22] and microresonator-based[23] waveguide sensors.

1.2 Introduction to Resonant Optical Microcavity Sensors

Our group has focused on microresonator-based waveguide sensors for the detection of biomolecules, and thus my dissertation will center around the detection capabilities of this technology. These sensors, which can be fabricated out of a variety of materials and with several similar, but distinct, cavity geometries, generally function by coupling light from an adjacent linear waveguide into a circular microcavity.[23] Optical interference between photons in the linear waveguide and microcavity dictate that only specific wavelengths of light are resonantly supported, as defined by the equation:

$$m\lambda = 2\pi r n_{eff}$$

where m is an integer, λ is the wavelength of light, r is the radius of the ring, and n_{eff} is the effective refractive index of the waveguide mode.

When fabricated with very high precision and limited cavity surface roughness, the resonance peaks become incredibly spectrally narrow and the structures are referred to as high Q (quality) factor cavities. The narrow peaks facilitate resolution of small shifts in the spectral position of the resonance, making these devices very sensitive to the local refractive index near the resonator. By functionalizing the microcavities with appropriate biomolecular capture agents, binding-induced changes in refractive index are transduced via a shift in the optical wavelengths resonantly supported by the structure. This concept is schematically illustrated for the case of a microring resonator in Figure 1.1A wherein biomolecular (protein) binding to a capture agent modified cavity (shown functionalized with antibody) causes the resonance wavelength to shift (black trace to red trace).

Microsphere,[24] microtoroid,[25] and microcapillary[26] cavities have been reported to have tremendous detection sensitivities. However, these devices are not readily fabricated in a chip-based format and optical interrogation of such cavities is not trivial (often requiring positioning of extruded optical fibers with nanometer precision and alignment). For this reason, microring resonators with chip-integrated linear access waveguides have emerged as promising candidates for scalable and multiplexable biosensing. Although the Q factor is lower for planar microcavity formats, as opposed to sphere, microtoroid, or capillary designs, the robust nature of the device in terms of ease in sensor interrogation, fabrication scalability, and functionalization offers advantages for applications in multiplexed biomolecular detection.[27]

Microring resonators sensors can be fabricated from a variety of materials, including polymers,[28] silicon oxide,[29, 30] silicon nitride,[31, 32] and SOI.[33-35] Figure 1.1B shows a scanning electron micrograph of a single microring resonator with corresponding linear access waveguide fabricated in the top layer of SOI. Typical sensitivities enable discrimination of changes in refractive index of 10^{-6} or better.[27, 32, 36, 37] In their most basic format, these sensors feature a single microring coupled horizontally to a linear waveguide, but methods have been devised for vertical coupling.[37] Furthermore, coiled[38] and slotted[31, 39] microring waveguides have also been demonstrated as well as Mach-Zehnder-integrated microrings, which show promise for increased sensitivity but at present face a potential drawback of reduced thermal stability.[40, 41]

Because the microring resonator format is readily amenable to highly scalable and commercially validated microfabrication approaches, several groups have demonstrated the ability to fabricate arrays of microring resonators on a single chip. These sensors have been used

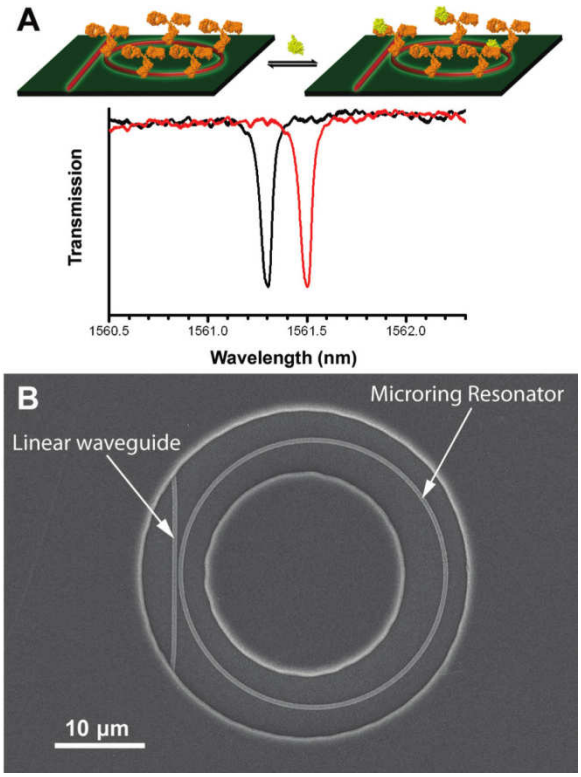

Figure 1.1 (A) Illustration of proteins binding to a microring resonator and the subsequent shift of the resonance frequency. (B) SEM image of a SOI microring resonator as revealed through an annular opening in a polymeric cladding layer that confines solution flow and biological binding events to the area immediately surrounding the microring.

for quantitative analysis of biological samples as well as multiplexed sensing. For example, Ramanchandran et al. have demonstrated a chip with five microring sensors and have shown that they could derivatize the rings with antibodies against E. coli.[30] These functionalized rings respond specifically to E. coli in comparison to unresponsive control rings. In the same paper the authors also showed specific binding of nucleic acids, as well as quantifying IgG binding. Subsequently, Wang and co-workers used an identical microring resonator array to monitor physical changes in cell behavior upon exposure to cytotoxic chemicals.[42]

Carlborg and co-workers have demonstrated the utility of slotted microring resonators by developing a chip that contains eight integrated microring resonators, six of which can be used as active sensing rings and two of which are employed as thermal controls.[32] Furthermore, this sensor chip was incorporated into a microfluidic casing that enabled independent fluidic access to each microring, which was then used to monitor the attachment of anti-BSA antibodies to the microcavities with good sensitivity.

1.3 Introduction to Protein Biomarker Detection and Dissertation Work

The overarching goal of my dissertation work has been to utilize microring resonator sensors for detecting protein biomarkers. In particular, my research has taken many progressive steps towards developing a multiplexed sensor chip that can detect multiple protein cancer biomarkers from human blood serum samples. The driving motivation behind the development of a multiplex biomarker chip is for personalized medicine applications. The fundamental tenet underlying personalized medicine is that multi-faceted diseases, such as cancer, are derived from a multitude of biochemical pathway perturbations, even though identical clinical symptoms are presented.[43] Or as the Canadian physician Sir William Osler (1849–1919) said,[44] “variability is the law of life, and as no two faces are the same, so no two bodies are alike, and no two individuals react alike and behave alike under the abnormal conditions we know as disease.”

The ultimate goals of personalized medicine are embodied in the rising field of theragnostics, which seeks to utilize molecular diagnostics to confirm which specific treatments or drug would help or harm a particular patient. For example, the drug trastuzumab (Herceptin) is particularly effective for patients that overexpress the HER2 protein. Thus corresponding diagnostic tests for HER2 overexpression in tumors make it possible to limit trastuzumab

treatment to only those patients who will be most likely to benefit.[45] Similarly, molecularly targeted therapies for *glioblastoma multiforme* have been under development for quite some time, but unlike HER2 protein, there exists no clinically available test to determine which patients would benefit from targeted treatments.[46]

Protein cancer biomarkers in blood serum have been investigated as a means to effectively diagnose and treat cancer. Unfortunately, single biomarker analysis has been shown to be rather limited in the personalized treatment of cancer. For example, prostate specific antigen (PSA) has been used as a stand-alone biomarker to inform the diagnosis and treatment of prostate cancer, but recent studies have questioned the efficacy of such screening.[47, 48] To improve upon this performance, it has been suggested that panels of protein biomarkers could provide a much more informative diagnostic and theragnostic picture.[49] The recent FDA approval of the OVA1 biomarker panel test for evaluation of ovarian tumor malignancy illustrates progress in the development of biomarker panels.

Microring resonators provide a convenient technology for the development of protein biomarker panels for several reasons. First, the ability to incorporate multiple sensors onto one microchip makes it possible to develop a single chip that can measure multiple cancer biomarkers from a single sample. Second, such chips can be manufactured in a scalable manner via standard semiconducting processing technologies that would enable sensor chips to be fabricated on a scale necessary for clinical use. Third, unlike other protein biomarker immunoassays which rely on fluorescent or enzymatic signal read-out strategies, microring resonator using refractive-index-based sensing can detect the binding of antigen, secondary antibodies, as well as any amplification step. By being to measure the binding at all steps of an assay, it is possible to rapidly evaluate capture agents, cross-reactivity, and appropriate immunoassay conditions.

The chapters of this dissertation are indicative of the stepwise progression towards developing a multiplex cancer biomarker chip using the novel silicon photonic microring resonator platform. Chapter 2 contains initial experiments done to evaluate and characterize the performance and sensitivity of the microring resonator chips. Chapter 3 similarly demonstrates the proof-of-principle label-free detection of a single cancer biomarker. This chapter also illustrates some of the challenges facing label-free detection in complex matrices. Chapter 4 builds on the work done in Chapter 3 by demonstrating the ability to create a multiplex cancer

biomarker chip. However, the work at this stage is still proof-of-principle in that the analytes are detected in a simple buffer environment rather than a complex matrix like blood serum. In continuing on to develop a larger multiplex array and to obtain sufficient sensitivity, the proper capture antibodies must be obtained. Chapter 5 discusses the means to evaluate antibody kinetics via a screening approach as well as how to utilize DNA-encoded antibodies for a more advanced surface chemistry development. Chapter 5 also shows how secondary antibodies can be screened for developing sandwich-type immunoassays. Chapter 6 finally demonstrates the ability to detect a single protein biomarker (cardiac) in human blood serum samples by using a sandwich immunoassay detection methodology followed by a bead-based signal amplification process. The ability to amplify signal without a large background is critical for detecting a multiplex panel of cancer biomarkers in human blood serum. Thus, Chapter 7 chronicles the use of all the previous advances in the development and creation of an eight-plex cancer biomarker chip. The detection of all eight cancer biomarkers from human serum samples from cancer patients illustrates the viability of microring resonators for personalized medicine applications.

1.4 Other Microring Resonator Work

In addition to my work with protein cancer biomarkers, the Bailey lab has also utilized microring resonators for other analytical applications, of which I will make brief mention here. For example, Luchansky et al. demonstrated the monitoring of interleukin-2 (IL-2) secretion from stimulated Jurkat T-cells in cell-free culture media using a sandwich assay approach.[50] Changes in secreted IL-2 levels were monitored over a period of 24-hours post stimulation and the results were found to be in excellent correlation with a commercial ELISA assay, with an added advantage of enhanced measurement precision. Byeon et al. demonstrated the monitoring of aniline-catalyzed antibody surface ligation, and determined the conditions under which optimal antibody attachment to the surface can be achieved.[51] Byeon et al. also used the multiplexing capabilities of microring resonators to compare the performance of an aptamer and antibody against the same antigen target.[52]

In addition to protein detection, the Bailey group has also demonstrated the ability to detect nucleic acids via microring resonators. Using a direct hybridization assay with DNA capture probes, Qavi et al. were able to detect four different micro RNAs (miRNAs) on a single

sensor chip.[53] Those four-plex chips were then used to detect those same four miRNAs isolated from a cell line model of glioblastoma. As follow-up work, Qavi et al. demonstrated that DNA:RNA duplexes can be specifically detected with an anti-DNA:RNA antibody.[54] This not only adds greater specificity to a miRNA assay but also enables amplification of the RNA-binding signal. In addition to miRNA detection, direct detection of DNA was demonstrated using multiplexed microring resonator sensors.[55] In this work, it was possible to discriminate single-nucleotide polymorphisms by comparing real-time dissociation rates of DNA duplexes.

Beyond detection of biomolecules, microring resonators can be utilized for monitoring surface chemistry such as surface-bound polymer growth. Limpoco et al. demonstrated that microring resonators can be used to measure the rates of growth of polymer brushes on silicon surfaces via an atom transfer radical polymerization process.[56] This detection methodology opens the door to studying surface polymer growth in a combinatorial fashion.

Overall, microring resonators have proven to be a promising technology that can be used in a vast array of detection schemes. Although the remainder of this dissertation will focus on cancer biomarker detection, a multitude of other analytical applications are available using the multiplexable microring resonator technology. Future developments of microring resonator technology—including the development of 128-plex chips with integrated fluidic cartridges—should only enhance the possibilities available with this technology.

1.5 References

(1) Haeberle, S.; Zengerle, R. *Lab Chip* **2007**, *7*, 1094-1110.

(2) Wolfbeis, O. S. *Anal. Chem.* **2008**, *80*, 4269-4283.

(3) Jokerst, N. M.; Luan, L.; Palit, S.; Royal, M.; Dhar, S.; Brooke, M. A.; Tyler, T. *IEEE Transactions on Biomedical Circuits and Systems* **2009**, *3*, 202-211.

(4) Monat, C.; Domachuk, P.; Eggleton, B. J. *Nature Photonics* **2007**, *1*, 106-114.

(5) Lin, L.; Evans, R. D.; Jokerst, N. M.; Fair, R. B. *IEEE Sens. J.* **2008**, *8*, 628-635.

(6) Banerjee, A.; Shuai, Y.; Dixit, R.; Papautsky, I.; Klotzkin, D. *J. Lumin.* **2010**, *130*, 1095-1100.

(7) Vengasandra, S.; Cai, Y.; Grewell, D.; Shinar, J.; Shinar, R. *Lab Chip* **2010**, *10*, 1051-1056.

(8) Wang, X.; Hofmann, O.; Das, R.; Barrett, E. M.; deMello, A. J.; deMello, J. C.; Bradley, D. D. C. *Lab Chip* **2007**, *7*, 58-63.

(9) Wojciechowski, J. R.; Shriver-Lake, L. C.; Yamaguchi, M. Y.; Füreder, E.; Pieler, R.; Schamesberger, M.; Winder, C.; Prall, H. J.; Sonnleitner, M.; Ligler, F. S. *Anal. Chem.* **2009**, *81*, 3455-3461.

(10) Ligler, F. S. *Anal. Chem.* **2008**, *81*, 519-526.

(11) Mukundan, H.; Anderson, A. S.; Grace, W. K.; Grace, K. M.; Hartman, N.; Martinez, J. S.; Swanson, B. I. *Sensors* **2009**, *9*, 5783-5809.

(12) Taitt, C. R.; Anderson, G. P.; Ligler, F. S. *Biosensors & Bioelectronics* **2005**, *20*, 2470-2487.

(13) Qavi, A. J.; Washburn, A. L.; Byeon, J.-Y.; Bailey, R. C. *Anal. Bioanal. Chem.* **2009**, *394*, 121-135.

(14) Tiefenthaler, K.; Lukosz, W. *J. Opt. Soc. Am. B* **1989**, *6*, 209-220.

(15) Székács, A.; Adanyi, N.; Székács, I.; Majer-Baranyi, K.; Szendrő, I. *Appl. Opt.* **2009**, *48*, B151-B158.

(16) Cottier, K.; Wiki, M.; Voirin, G.; Gao, H.; Kunz, R. E. *Sensors Actuators B: Chem.* **2003**, *91*, 241-251.

(17) Heideman, R. G.; Lambeck, P. V. *Sensors Actuators B: Chem.* **1999**, *61*, 100-127.

(18) Dumais, P.; Callender, C. L.; Noad, J. P.; Ledderhof, C. J. *Opt. Express* **2008**, *16*, 18164-18172.

(19) Lee, M.; Fauchet, P. M. *Opt. Express* **2007**, *15*, 4530-4535.

(20) Lee, M. R.; Fauchet, P. M. *Opt. Lett.* **2007**, *32*, 3284-3286.

(21) Dorfner, D.; Zabel, T.; Hürlimann, T.; Hauke, N.; Frandsen, L.; Rant, U.; Abstreiter, G.; Finley, J. *Biosens. Bioelectron.* **2009**, *24*, 3688-3692.

(22) Buswell, S. C.; Wright, V. A.; Buriak, J. M.; Van, V.; Evoy, S. *Opt. Express* **2008**, *16*, 15949-15957.

(23) Vollmer, F.; Arnold, S. *Nat. Methods* **2008**, *5*, 591-596.

(24) Arnold, S.; Khoshsima, M.; Teraoka, I.; Holler, S.; Vollmer, F. *Opt. Lett.* **2003**, *28*, 272-274.

(25) Armani, A. M.; Kulkarni, R. P.; Fraser, S. E.; Flagan, R. C.; Vahala, K. J. *Science* **2007**, *317*, 783-787.

(26) Zhu, H.; White, I. M.; Suter, J. D.; Dale, P. S.; Fan, X. *Opt. Express* **2007**, *15*, 9139-9146.

(27) Iqbal, M.; Gleeson, M. A.; Spaugh, B.; Tybor, F.; Gunn, W. G.; Hochberg, M.; Baehr-Jones, T.; Bailey, R. C.; Gunn, L. C. *IEEE J. Sel. Top. Quantum Electron.* **2010**, *16*, 654-661.

(28) Chao, C. Y.; Fung, W.; Guo, L. J. *IEEE J. Sel. Top. Quantum Electron.* **2006**, *12*, 134-142.

(29) Yalçin, A.; Popat, K. C.; Aldridge, J. C.; Desai, T. A.; Hryniewicz, J.; Chbouki, N.; Little, B. E.; King, O.; Van, V.; Chu, S.; Gill, D.; Anthes-Washburn, M.; Ünlü, M. S. *IEEE J. Sel. Top. Quantum Electron.* **2006**, *12*, 148-155.

(30) Ramachandran, A.; Wang, S.; Clarke, J.; Ja, S. J.; Goad, D.; Wald, L.; Flood, E. M.; Knobbe, E.; Hryniewicz, J. V.; Chu, S. T.; Gill, D.; Chen, W.; King, O.; Little, B. E. *Biosens. Bioelectron.* **2008**, *23*, 939-944.

(31) Barrios, C. A.; Bañuls, M. J.; González-Pedro, V.; Gylfason, K. B.; Sánchez, B.; Griol, A.; Maquieira, A.; Sohlström, H.; Holgado, M.; Casquel, R. *Opt. Lett.* **2008**, *33*, 708-710.

(32) Carlborg, C. F.; Gylfason, K. B.; Kaźmierczak, A.; Dortu, F.; Bañuls Polo, M. J.; Catala, A. M.; Kresbach, G. M.; Sohlström, H.; Moh, T.; Vivien, L.; Popplewell, J.; Ronan, G.; Barrios, C. A.; Stemme, G.; van der Wijngaart, W. *Lab Chip* **2010**, *10*, 281-290.

(33) De Vos, K.; Girones, J.; Popelka, S.; Schacht, E.; Baets, R.; Bienstman, P. *Biosens. Bioelectron.* **2009**, *24*, 2528-2533.

(34) De Vos, K. M.; Bartolozzi, I.; Bienstman, P.; Baets, R.; Schacht, E. *Proc. SPIE* **2007**, *6447*, 64470K.

(35) Washburn, A. L.; Gunn, L. C.; Bailey, R. C. *Anal. Chem.* **2009**, *81*, 9499-9506.

(36) Debackere, P.; Taillaert, D.; De Vos, K.; Scheerlinck, S.; Bienstman, P.; Baets, R., San Jose, CA, USA 2007; SPIE; 647719-647710.

(37) Kim, G.-D.; Son, G.-S.; Lee, H.-S.; Kim, K.-D.; Lee, S.-S. *Optics Communications* **2008**, *281*, 4644-4647.

(38) Xu, D.-X.; Densmore, A.; Delâge, A.; Waldron, P.; McKinnon, R.; Janz, S.; Lapointe, J.; Lopinski, G.; Mischki, T.; Post, E.; Cheben, P.; Schmid, J. H. *Opt. Express* **2008**, *16*, 15137-15148.

(39) Li, X.; Zhang, Z.; Qin, S.; Wang, T.; Liu, F.; Qiu, M.; Su, Y. *Appl. Opt.* **2009**, *48*, F90-F94.

(40) Terrel, M.; Digonnet, M. J. F.; Fan, S. H. *Appl. Opt.* **2009**, *48*, 4874-4879.

(41) Yi, H.; Citrin, D. S.; Chen, Y.; Zhou, Z. *Appl. Phys. Lett.* **2009**, *95*, 191112-191113.

(42) Wang, S.; Ramachandran, A.; Ja, S.-J. *Biosens. Bioelectron.* **2009**, *24*, 3061-3066.

(43) Chan, I. S.; Ginsburg, G. S. *Annual Review of Genomics and Human Genetics* **2011**, *12*, 217-244.

(44) Silverman, M. E.; Murray, T. J.; Bryan, C. S., Eds. *The Quotable Osler*; American College of Physicians: USA, 2008.

(45) Pene, F.; Courtine, E.; Cariou, A.; Mira, J. P. *Crit. Care Med.* **2009**, *37*, S50-S58.

(46) Huang, T. T.; Sarkaria, S. M.; Cloughesy, T. F.; Mischel, P. S. *Neurotherapeutics* **2009**, *6*, 500-512.

(47) Schroder, F. H.; Hugosson, J.; Roobol, M. J.; Tammela, T. L. J.; Ciatto, S.; Nelen, V.; Kwiatkowski, M.; Lujan, M.; Lilja, H.; Zappa, M.; Denis, L. J.; Recker, F.; Berenguer, A.; Maattanen, L.; Bangma, C. H.; Aus, G.; Villers, A.; Rebillard, X.; van der Kwast, T.; Blijenberg, B. G.; Moss, S. M.; de Koning, H. J.; Auvinen, A.; the ERSPC Investigators *N. Engl. J. Med.* **2009**, *360*, 1320-1328.

(48) Andriole, G. L.; Crawford, E. D.; Grubb, R. L., III; Buys, S. S.; Chia, D.; Church, T. R.; Fouad, M. N.; Gelmann, E. P.; Kvale, P. A.; Reding, D. J.; Weissfeld, J. L.; Yokochi, L.

A.; O'Brien, B.; Clapp, J. D.; Rathmell, J. M.; Riley, T. L.; Hayes, R. B.; Kramer, B. S.; Izmirlian, G.; Miller, A. B.; Pinsky, P. F.; Prorok, P. C.; Gohagan, J. K.; Berg, C. D.; the PLCO Project Team *N. Engl. J. Med.* **2009**, *360*, 1310-1319.

(49) Rhea, J. M.; Molinaro, R. J. *MLO. Med. Lab. Obs.* **2011**, *43*, 10-18.

(50) Luchansky, M. S.; Bailey, R. C. *Anal. Chem.* **2010**, *82*, 1975-1981.

(51) Byeon, J.-Y.; Limpoco, F. T.; Bailey, R. C. *Langmuir* **2010**, *26*, 15430-15435.

(52) Byeon, J.-Y.; Bailey, R. C. *Analyst* **2011**, *136*, 3430-3433.

(53) Qavi, A. J.; Bailey, R. C. *Angew. Chem. Int. Ed.* **2010**, *49*, 4608-4611.

(54) Qavi, A. J.; Kindt, J. T.; Gleeson, M. A.; Bailey, R. C. *Anal. Chem.* **2011**, *83*, 5949-5956.

(55) Qavi, A. J.; Mysz, T. M.; Bailey, R. C. *Anal. Chem.* **2011**, *83*, 6827-6833.

(56) Limpoco, F. T.; Bailey, R. C. *J. Am. Chem. Soc.* **2011**, *133*, 14864-14867.

Chapter 2

Characterization of the Evanescent Field Profile and Bound Mass Sensitivity of a Label-free Silicon Photonic Microring Resonator Biosensing Platform

Notes and Acknowledgements

This chapter has been reproduced from the original paper "Characterization of the Evanescent Field Profile and Bound Mass Sensitivity of a Label-free Silicon Photonic Microring Resonator Biosensing Platform" (Luchansky, M. S.; Washburn, A. L.; Martin, T. A.; Iqbal, M; Gunn, L. C.; Bailey, R. C. *Biosens. Bioelectron.* **2010**, *26*, 1283–1291). It has been reproduced here with permission from Elsevier © 2010.

Matthew Luchansky is acknowledged for his joint assistance in this project. His work is represented in the antibody-strepatividin layer-by-layer data and figures, as well as the joint collection of the radiolabeled streptavidin data. Teresa Martin is acknowledged for her assistance in performing the radiolabel experiments and for generating the radiolabled compounds. In addition, this work would not have been completed without the assistance of F. Ted Limpoco for assistance with polyelectrolyte multilayer thickness determination via ellipsometry, and of Ji-Yeon Byeon for acquiring the SEM image of the microring, and of Abraham Qavi for assistance in creating the robot automation.

The work in this chapter was funded by the NIH Director's New Innovator Award Program, part of the NIH Roadmap for Medical Research, through grant number 1-DP2-OD002190-01, and by the Camille and Henry Dreyfus Foundation. Eastman Chemical Company provided funds used to construct the LEGO robot used for multilayer growth automation. M.S.L. was supported via a National Science Foundation Graduate Research Fellowship and a Robert C. and Carolyn J. Springborn Fellowship from the Department of Chemistry at the University of Illinois at Urbana-Champaign. A.L.W. was supported via a National Science Foundation Graduate Research Fellowship. This research was carried out in part in the Frederick Seitz Materials Research Laboratory Central Facilities, University of Illinois, which are partially supported by the U.S. Department of Energy under grants DE-FG02-07ER46453 and DE-FG02-07ER46471.

This article can be accessed online at: http://dx.doi.org/10.1016/j.bios.2010.07.010

2.1 Introduction

Waveguides, including fiber optics, have become valuable tools for detecting chemical and biological species through a range of optical transduction mechanisms, including absorbance, fluorescence, and refractive index-induced phase or transmission intensity modulation.[1-6] For all waveguide materials and geometries, light propagates through the waveguide on account of total internal reflection that occurs due to the contrast in refractive index between the core and cladding materials. At the core/cladding interface, an evanescent optical field extends from the surface and decays exponentially with distance.[7] Regardless of the particular transduction mechanism utilized for sensing, the measured signal is elicited through light-matter interactions between this evanescent field and proximal target molecules.

Most relevant to this report are label-free transduction methods whereby the presence of a particular analyte causes a fundamental change in the optical transmission properties of the waveguide, thus eliminating requirements for chromophoric or fluorescent labels.[8] In most examples, the waveguide is chemically modified to present a target-specific capture element, and localization of the analyte at the core-cladding interface leads to an attenuation in the power of the transmitted light.

Recently there have been reports of chemical and biomolecular sensors based upon waveguides fabricated from a range of different materials, many of which leverage advances in semiconductor processing for micro- or nano-scale device fabrication.[1] A particularly promising waveguide material is silicon-on-insulator (SOI), a feedstock of the microelectronics industry.[9] SOI waveguides are patterned into the top layer of silicon, and light is effectively guided due to the high refractive index contrast between Si and the cladding layers, which include the buried oxide and the top/side cladding layers. In addition to the obvious advantages of SOI in terms of scalability and potential for mass production, silicon photonic devices also feature good modal overlap between the guided optical mode and an analyte recognition layer.[10] The high refractive index of the waveguide core layer leads to a high sensitivity towards surface-confined binding events. Several groups have demonstrated silicon photonic waveguide configurations for chemical or biological sensing applications, including Mach-Zehnder interferometers,[10-12] resonant gratings,[13] and microcavity resonators.[14-18] Using arrays of SOI microring resonators,

we previously reported a bulk refractive index sensitivity of 7.6 x 10^{-7} refractive index units (RIU)[19] and have demonstrated the sensitive, label-free detection of multiple proteins and nucleic acid sequences in both single and multiparameter analytical applications.[20-23]

Another label-free optical method that is particularly well-suited to analyzing biomolecular binding, thus serving as a basis for comparison, is surface plasmon resonance (SPR). SPR measures the interaction of an evanescent field extending from a metallic film, usually gold, in contact with the analyte-containing solution. Binding events that change the refractive index at the gold-solution interface are measured either as a change in the angle or wavelength of light which is maximally coupled into the metal film. SPR has been actively investigated as a biosensing technique over the past several decades with a number of reported sensor geometries and modes of operation, several of which are available commercially.[24-26] For SPR sensors, the evanescent field penetration depth, which is a function of wavelength and dielectric environment, is on the order of hundreds of nanometers[27] with bulk refractive index sensitivities usually varying between 10^{-5} and 10^{-7} RIU.[25, 28] For reference,[25] a bulk index sensitivity of 10^{-6} RIU corresponds to a surface coverage resolution of 0.91 pg/mm^2.

Presented in this chapter is a simulation of the waveguide optical intensity profile as well as a direct, experimental interrogation of the evanescent intensity decay profile of a silicon photonic microring resonator. We empirically measured the distance dependence of the sensing platform utilizing layer-by-layer electrostatic polymer multilayer deposition.[29, 30] We also directly determined the bound mass sensitivity and limit of detection (LOD) of our system by correlating the resonance wavelength shifts with the amount of bound ^{125}I-lableled streptavidin, measured via radiometric methods. Importantly, this chapter presents key, experimentally determined sensitivity metrics for an emerging silicon photonic biomolecular sensing platform. In addition to providing a benchmark for comparison, the dependence of device sensitivity on distance from the sensor surface will be important when designing coatings for optimal analyte recognition and localization within the evanescent intensity profile of the guided optical mode.

2.2 Materials and methods

2.2.1 Materials

N-hydroxysuccinimidobiotin (NHS-Biotin), streptavidin, Zeba spin filter columns, and pre-coated iodination tubes were obtained from Pierce (Rockford, IL). 3-aminopropyltriethoxysilane (APTES) was purchased from Gelest (Morrisville, PA). Succinimidyl 4-formylbenzoate (S-4FB) and 3-N-((6-(N'-Isopropylidene-hydrazino))nicotinamide)propyltriethoxysilane (HyNic silane), were purchased from SoluLink (San Diego, CA). Shipley 1813 photoresist, MF 319 developer, and 1165 photoresist stripper were purchased from MicroChem Corp. (Newton, MA). Poly(sodium 4-styrene-sulfonate) (PSS, MW~70,000 Da) , polyethyleneimine (PEI, 50% w/w in H_2O, MW~750,000 Da), and poly(allylamine hydrochloride) (PAH, MW~56,000 Da) were obtained from Sigma Aldrich (St. Louis, MO). Biotinylated, monoclonal mouse anti-human IL-2 antibody (catalog# 555040, clone B33-2 was purchased from BD Biosciences (San Jose, CA). All other chemicals were used as received from Sigma Aldrich (St. Louis, MO).

All buffers were made with purified water (ELGA PURELAB filtration system; Lane End, UK), and the pH was adjusted using 1 M HCl or 1 M NaOH. Tris buffer consisted of 0.5 mM Tris and 100 mM NaCl adjusted to pH 7.1. Tris/ EDTA buffer was made by dissolving 1.21 g Tris base, 0.558 g disodium EDTA, and 0.2 g sodium azide in 1 L water and adjusting to pH 7.4. PBS was made by dissolving 9.6 g Dulbecco's phosphate buffered saline mixture into 1 L water and adjusting to pH 7.4. Antibody immobilization buffer consisted of 100 mM PBS with 150 mM NaCl adjusted to pH 6.0. BSA-PBS buffer consisted of 0.1 mg/mL BSA in PBS. For blocking, StartingBlock blocking buffer (Pierce) was used.

2.2.2 Microring Resonator Array Chips and Instrumentation

The design and fabrication of microring resonator array chips, the accompanying instrumentation, and the fluidics have been described in other papers.[19, 22] Briefly, chips having 32 individually addressable microrings were used for the experiments. The entire substrate was coated with a fluoropolymer cladding layer that was removed from annular openings over 24 of the sensors. The remaining eight microrings were left occluded by the cladding and were utilized

as thermal controls, since they were not exposed to the solution. Microring resonance frequencies were measured as described previously. Briefly, the beam of a 1560-nm center wavelength tunable, external cavity diode laser is focused onto an input grating coupler on the chip surface to couple light into the linear waveguide adjacent to a given microring. The laser output is then rapidly swept through a 12-nm spectral window, and the intensity of light projected from the output grating coupler is monitored as a function of laser wavelength. Resonance wavelengths are determined as minima in output coupler intensity. This process is repeated for each interrogated microring sensor by rastering the laser across all 32 input grating couplers , allowing resonance determination with ~250-ms time resolution. Thermal control ring responses are used to control for ambient thermal drift.

2.2.3 Layer-by-layer Deposition

For the layer-by-layer electrostatic deposition of polymers, PEI, PSS, and PAH were dissolved in Tris buffer to 5 mg/mL. After cleaning the microring surface with piranha solution (3:1 H_2SO_4:H_2O_2) and loading the chip into a previously described microfluidic flow cell,[22] chips are exposed to PEI for 5 min at 30 µL/min. Maintaining constant flow conditions with a P625 peristaltic pump from Instech Laboratories (Plymouth Meeting, PA), the surface is then rinsed with Tris buffer and exposed to PSS for 10 min followed by a buffer rinse. The surface is then exposed to PAH for 4 minutes with a 5 minute buffer rinse. The PSS and PAH deposition cycles (with the PSS time reduced to 6 minutes) and buffer rinses were repeated until a total of 72 bilayers had been grown.

To facilitate automated solution switching, we constructed a robot using the LEGO (Billund, Denmark) MINDSTORMS NXT 2.0 system that automatically moved the inlet tubing between solutions (see Figure 2.1). To automate fluid delivery, 0.38-mm inner diameter Teflon inlet tubing was connected from the ring resonator microfluidic system to the sipper arm motor of the robot which rotated up and down ~55° to raise and lower the tubing into the six different solutions used for the multilayer experiments. Typically, solutions 1–3 contained running buffer and the two components of the multilayer experiment while solutions 4–6 contained buffer rinses so that solution on the tip of the tubing would not contaminate the other vials. To switch solutions, first the arm was raised, and then the rotating platform turned 60°, and then the arm

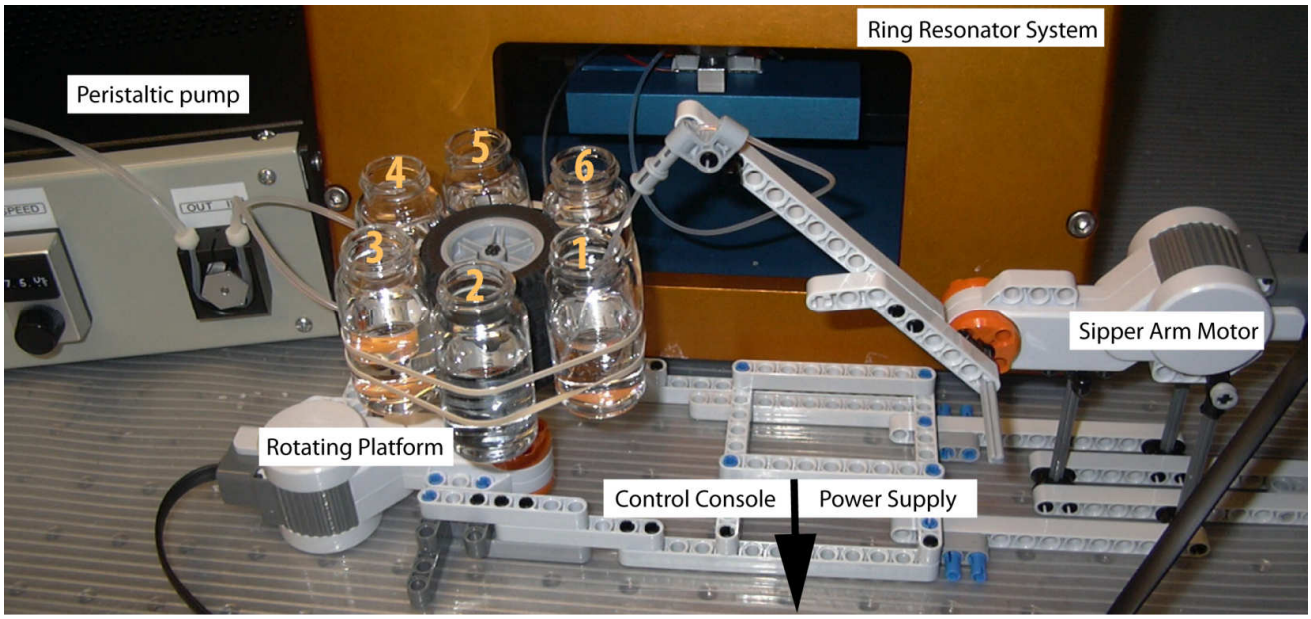

Figure 2.1 Picture of LEGO MINDSTORMS NXT 2.0 robot for automation of multilayer formation with labels on each component. The LEGO control console loaded with customized software for the solution switching process and the 9.0 V power supply are not shown.

was lowered into the next vial. The control console was programmed using LEGO MINDSTORMS NXT 2.0 software and powered with a 9.0 V DC power supply. Constant fluid flow was maintained via the peristaltic pump fitted with 0.79-mm inner diameter silicone tubing which was connected to the 0.5-mm inner diameter Tygon outlet tubing of the microring resonator system.

To verify PAH/PSS bilayer thickness, we performed a large-area layer-by-layer experiment on four different silicon substrates. In order to confirm both the layer thickness and the growth linearity, the layer growth process was halted at a different point for each wafer section prior to performing ellipsometry. Because ellipsometry requires a wider area than what our microfluidic channels provide, we created the multilayers on the silicon wafer pieces using a dipping approach rather than a microfluidic flow-based approach. We utilized the same concentrations and exposure times for the microfluidics setup, and we reconfigured the LEGO robot to dip the pieces of silicon wafer into the solution vials. At the end of the layer growth, each substrate was washed briefly with water and then dried under a gentle stream of nitrogen. Ellipsometry was performed using a J.A. Woollam variable angle spectroscopic ellipsometer (Lincoln, NE). For each spot, three different angles of incidence were measured (65°, 75°, 85°) and the thicknesses were calculated assuming a SiO_2 thickness of 2.4 nm, and a Cauchy layer model for the dried polyelectrolyte bilayers with an assumed refractive index of 1.68.[31]

Prior to performing layer-by-layer deposition of proteins, hydrazine moieties were installed on the silicon oxide chip surface by flowing a solution of HyNic-silane (1 mg/mL in 95% ethanol and 5% dimethyl formamide) over the surface for 30 min at 5 µL/min followed by rinsing with ethanol. Separately aldehyde groups were introduced to biotinylated IgG antibodies by reaction with a 5-fold molar excess of 0.2 mg/mL S-4FB for 2 h at room temperature. After buffer exchanging with a Zeba spin column into 100 mM PBS pH 6.0 to remove excess S-4FB, the antibody solution was diluted to 0.1 mg/mL and flowed over the entire sensor array for covalent attachment via a hydrazone linkage. Aniline (100 mM) was added to catalyze the formation of the hydrazone bond between the antibody aldehyde and the hydrazine-functionalized surface.[32] After rinsing the chip in buffer, the surface was blocked in StartingBlock overnight at 4 ˚C.

For layer-by-layer protein deposition, biotinylated anti-IL-2 and streptavidin were diluted in BSA-PBS to 2 µg/mL. After loading the antibody-functionalized chip into the flow cell, BSA-

PBS buffer was flowed at 23 μL/min . Maintaining the same flow conditions, the surface was exposed to streptavidin for 20 min, followed by a 2-min buffer rinse, and then to biotinylated antibody for 20 min, followed by a 2-min buffer rinse. This cycle was repeated for a total of 75 layers (37 bilayers on top of an antibody-functionalized surface). The LEGO robot was again used to facilitate automated solution switching over the ~30-hr multilayering process.

2.2.4 ^{125}I-Streptavidin Experiments

Streptavidin was labeled with ^{125}I, a γ-emitter, according to the manufacturer's instructions using pre-coated iodination tubes (Pierce). Labeled streptavidin was purified from free ^{125}I using a G-25 Sephadex-packed glass column. The concentration of radiolabeled streptavidin (> 90% purity) was determined to be 1-2 μg/mL for each of three trials.

The Storm 840 PhosphorImager (GE Healthcare) utilized to image the amount of ^{125}I-streptavidin deposited on the substrate did not have adequate spatial resolution to allow visualization of individual sensing elements. Therefore, the fluoropolymer cladding layer was removed in its entirety from half of each chipusing photolithography and reactive ion etching (RIE).

To remove the fluoropolymer layer, the chip was spin-coated with Shipley 1813 (2000 RPM, 30 sec) photoresist, followed by a 1-min post-bake at 115 ˚C. Half of the chip was then exposed for 1 min to a 30 mW/cm^2 dose of 350-nm light through a mask covering half of the chip. The photoresist was then developed for 5 min in MF-319, and the fluoropolymer was removed on the exposed half of the chip by performing oxygen RIE (4 min, 9.8 sccm O_2, 50 sccm Ar, 16 mTorr, 100 W, 310 V DC bias) on a PlasmaLab RIE System. The protective photoresist layer was subsequently removed by a 15-min soak in 1165 stripper followed by a 10-min sonication in acetone, an isopropanol rinse, and drying in a nitrogen stream.

Before flowing ^{125}I-streptavidin over the sensor surface, the chip was piranha cleaned as and loaded in the microfluidic flow cell with a gasket that allowed exposure of the entire array to a single solution volume. The surface was first modified with an amine-terminated silane by flowing a 2% solution of APTES in ethanol over the surface at 30 μL/min for 10 minutes, followed by rinsing with ethanol. A 0.4-mM NHS-Biotin solution (in 100mM PBS, pH 7.4 with 4% DMF) was flowed over the surface at 30 μL/min for 30 min, followed by rinsing with PBS.

Finally, the sensor surface was exposed to the ^{125}I-streptavidin solution for 10-30 min and washed with buffer. After the microring resonance shift determination, the chip was imaged on the phosphorimager along with a set of spotted protein standard solutions that were allowed to evaporate onto a glass slide. The bound streptavidin surface density was determined by comparison to protein standards and correlated with the wavelength shifts from rings on the side of the chip from which the cladding layer had been removed. This process was performed in triplicate.

2.3 Calculations

For waveguide sensors, the sensing modality is based on the interaction of the propagating evanescent field with the molecules of interest at or near the waveguide surface. In our silicon-on-insulator platform, light is coupled into linear Si waveguides that access the microring waveguides. As shown in Figure 2.2, each 30-μm ring is separated from the linear waveguide by 200 nm to allow for efficient light coupling between the waveguides only at wavelengths (λ) that match the resonance condition defined by:

$$m\lambda = 2\pi r n_{eff}$$

where m is an integer, r is the microring radius, and n_{eff} is the effective refractive index of the optical mode. Since organic and biological molecules have higher refractive indices (n = 1.4-1.6) than water (n = 1.33), their binding to the sensor surface increases the effective refractive index sampled by the optical mode.[33] The monitoring of resonant wavelength shift as a function of target binding provides the label-free sensing modality.

The equations describing the evanescent field propagation are derived from the boundary conditions of the electromagnetic wave equations that require a non-zero electric field at the reflective dielectric interface. As a result, the evanescent wave decays exponentially from the surface and, ignoring light scattering, the rate at which the field intensity decays can be described by:

$$I(z) = I_0 e^{-2\gamma z}$$

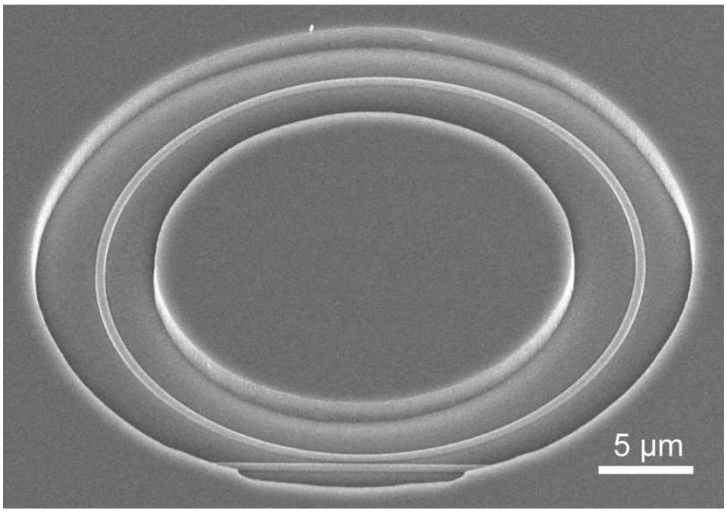

Figure 2.2 Scanning electron micrograph of a Si microring resonator waveguide adjacent to a linear waveguide. An annular opening in the fluoropolymer cladding layer exposes the surrounding SiO_x surface only in the immediate vicinity of the ring.

where $I(z)$ is the intensity of the evanescent as a function of perpendicular distance z from the surface, I_0 is the initial intensity, and γ is the exponential decay constant. As described previously, the shift in resonance wavelength is proportional to the intensity of the evanescent field extending into the surrounding environment.[34]

Simulations of the waveguide optical intensity profile were performed using the classic eigenfunction approach as described previously.[35] Briefly, Maxwell's equations are solved satisfying the boundary conditions at the dielectric interfaces of the waveguides, resulting in a set of transcendental equations that were solved for the wavenumber of the transverse optical mode. The mode is oscillatory in the core of the waveguide, but in the evanescent region external to the core, it decays exponentially as shown in Figure 2.3. The physical constants used in the calculation were matched to those in the experimental system, characterized by a 200-nm thick by 500-nm wide waveguide having $n_{core} = 3.43$, $n_{substrate} = 1.46$, $n_{surroundings} = 1.33$, and $\lambda = 1.56$ µm. The exponential decay coefficient, γ, in Eq. 2 was found to be 9.56 μm^{-1} for the optical field at the surface of the waveguide extending into the analyte sensing region. At a distance of $z = 1/2\gamma = 52.3$ nm from the waveguide, the intensity of the evanescent field, $I(z)$, has decreased to $(1/e) \times I_0$ or 36.7% of its initial value.

2.4 Results and discussion

2.4.1 Polyelectrolyte Layer-by-layer Results

To experimentally profile the evanescent decay from our microrings, we utilized layer-by-layer assembly of alternating anionic and cationic polymers onto the surface to map the intensity of the sensor response as a function of z. Specifically, PSS and PAH were selected due to the extensive literature describing PSS/PAH multilayers with linear growth over a wide range of thicknesses.[36-38] Following these previous reports, we prepared our silicon oxide-passivated surface with a layer of the highly branched polymer PEI to ensure sufficient coverage of the initial polyelectrolyte, followed by the addition of subsequent layers of PSS and PAH. Figure 2.4A illustrates the growth process, starting with the negatively charged silicon oxide surface. After addition of a PEI layer, PSS and then PAH are added in sequence. This process is repeated to form 72 PSS/PAH bilayers. Figure 2.4B shows the real-time shift in resonance wavelength from a representative microring corresponding to the addition of each electrostatic polymer layer.

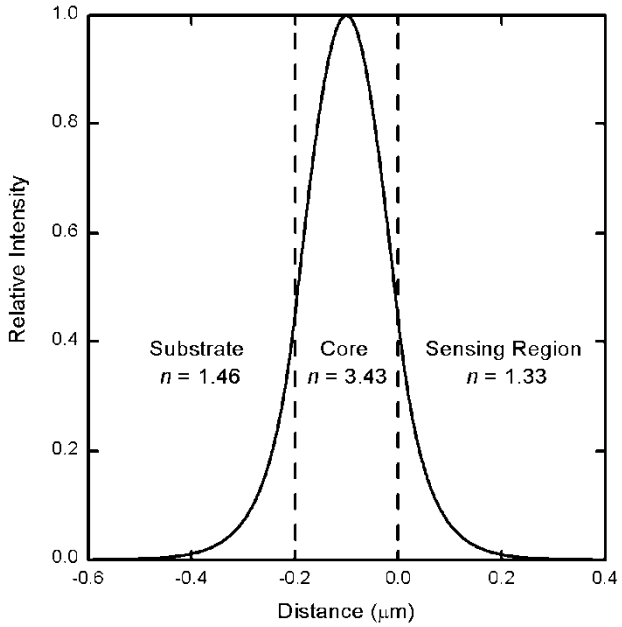

Figure 2.3 Cross-sectional plot of the evanescent field intensity for the 0.2 x 0.5- micron optical waveguide. The dashed lines represent the top and bottom extents of the waveguide core. The top surface of the waveguide exposed to the chemical reactions is at $x = 0$. Refractive indices of each region utilized in the simulation of the evanescent profile are depicted.

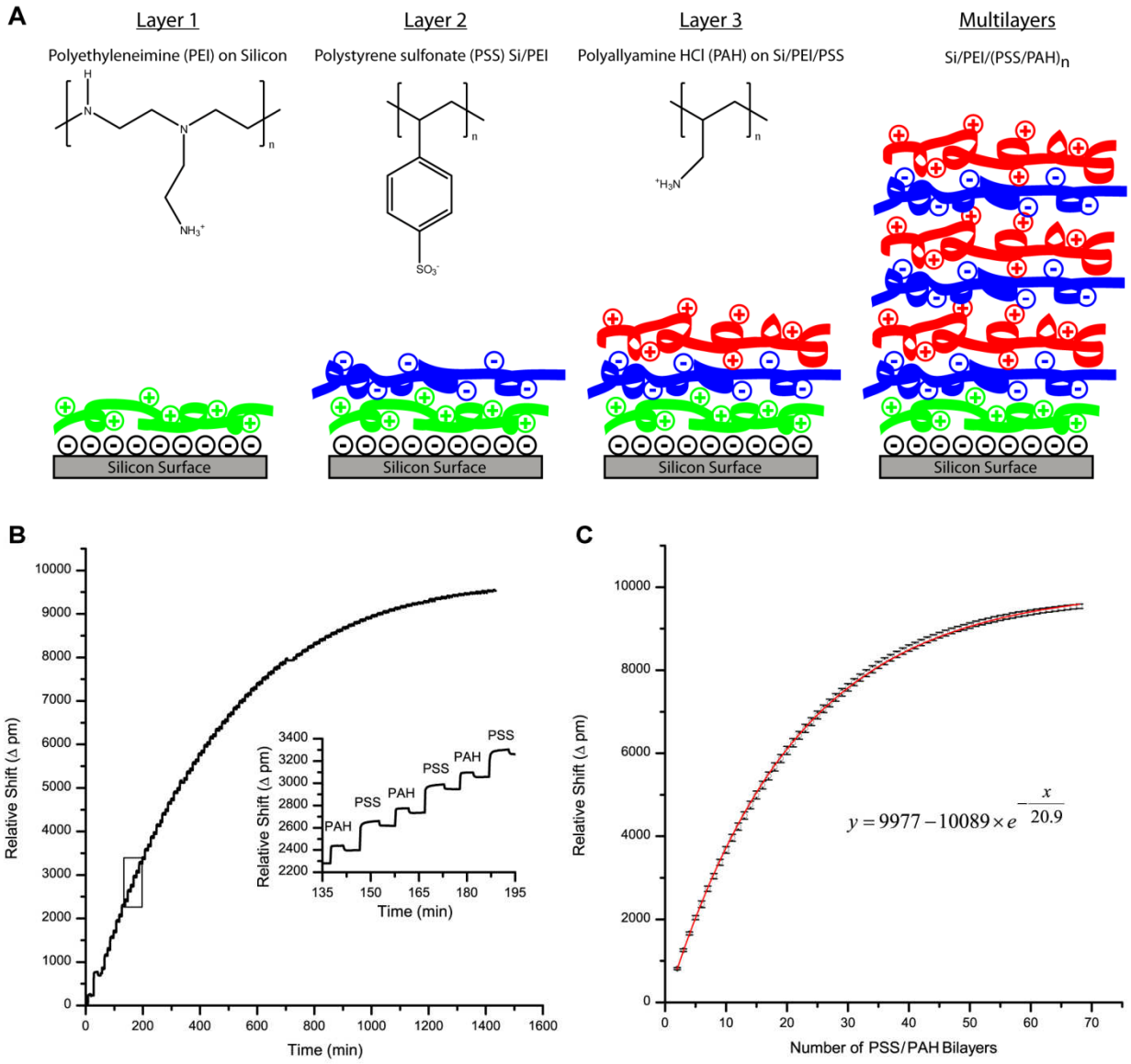

Figure 2.4 (A) Schematic showing the layer-by-layer addition of polyelectrolytes to a negatively charged silicon oxide surface. Layer 1 involves addition of positively charged, highly branched PEI, and Layer 2 involves addition of negatively charged PSS on top of the PEI. Layer 3 consists of positively charged PAH adhering to the PSS layer. Multilayers are added by alternating deposition of PSS and PAH layers. (B) Real time data showing the relative shift in resonance frequency (Δ pm) upon addition of PAH and PSS layers. Inset shows six layer-by-layer depositions at higher resolution. (C) Plot showing the relative resonance wavelength shift for each successive PAH/PSS bilayer as a function of bilayer number. The exponential fit shown in the plot models the decay rate as the polyelectrolyte multilayers grow further from the surface and experience the decreasing evanescent field intensity, as evidenced by the reduced response for each subsequent layer. Error bars represent the standard deviation for n = 23 rings.

With each additional layer, the differential sensor response decreases as multilayer assembly occurs at a greater distance from the surface. The decreasing sensitivity to refractive index changes corresponds to the evanescent intensity decay profile extending off of the microring waveguide. Figure 2.4C shows the average net sensor response (n = 23 rings) for each successive polymer bilayer as a function of the number of PSS/PAH bilayers added.

By fitting the points in Figure 2.4C to an exponential function, it becomes apparent that the response for each subsequent layer decays exponentially. From the exponential fitting function, the 1/e decay length for sensor response is 20.9 bilayers, which can be converted to a decay distance of 63 ± 4 nm using a 3.0 ± 0.2 nm thickness for each hydrated bilayer.[37, 38]

The literature value for PSS/PAH bilayer thickness was also experimentally confirmed through ellipsometry performed at several points during a layer-by-layer deposition process on a large area substrate. Based on the ellipsometry data shown in Figure 2.5, the thickness at each point in the growth process shows a highly linear correlation to the number of bilayers. The slope of a linear regression fit to these points was found to be 2.44 ± 0.04 nm/bilayer (R^2 = 0.999). This corresponds well with the dry thickness of PAH/PSS bilayers given in previous reports.[36, 38, 39] By incorporating a ~30% increase[38, 40] in size due to swelling in water, the hydrated thickness can be calculated to be 3.17 nm. This confirms the 3.0-nm value we use to calculate our layer thickness.

This experimentally determined decay distance of 63 nm is in reasonable agreement with the evanescent intensity simulation, which yielded a value of 52 nm. Possible sources of discrepancy include: uncertainty in hydrated bilayer thickness and film uniformity; the difference in surrounding index of buffer solution (experimental) versus water (simulation); dynamic changes in the mode profile during the course of multilayer growth; and other experimental deviations from idealized conditions. However, both simulation and empirical measurement provide sufficient information regarding the evanescent decay to interpret the results from the following protein multilayer study.

2.4.2 Antibody/Streptavidin Layer-by-layer Results

After verifying the exponential decay length experimentally using the electrostatic polymer system, we turned to a biological layer-by-layer system with more complex growth

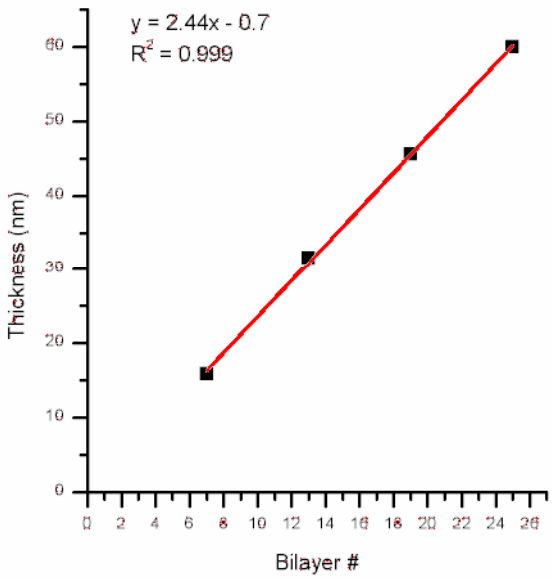

Figure 2.5 Thickness of PSS/PAH polyelectrolyte multilayers as a function of bilayer # based on ellipsometric measurement of the dry multilayers.

characteristics. As a test case, we constructed multilayers of an antibody (biotinylated mouse anti-human IL-2 IgG) functionalized with ~10 biotin molecules, and streptavidin, which binds with high-affinity ($K_d \sim 10^{-15}$ M) to up to four biotin molecules. The multivalent nature of both biomolecules ensures that extended assemblies can be grown. As shown in Figure 2.6A, the surface is first functionalized with SFB-modified biotinylated antibody (Ab) as has been described previously,[20] followed by addition of a streptavidin (SA) layer. Additional biotinylated Ab was attached to the bound SA. This process was repeated, resulting in multilayer growth (75 total layers). The resonance wavelength shift associated with the growth of each layer was monitored in real time under conditions empirically optimized to insure complete layer formation. As shown in Figure 2.6B, the resonant wavelength shift for each layer initially follows a non-linear growth trend, as will be further discussed below, before the effect of the decaying evanescent intensity dominates as the distance from the ring increases. This leads to a pseudo-inflection point in Figure 2.6B at ~300 min. Following this inflection point, the average cumulative shift arising from protein layers 16 through 75 can be fit to an exponential function, as shown in Figure 2.6C. This fit is in the same form as the exponential function used to model the response to polymer multilayers. The shifts corresponding to layers 1-15 were not included since layer growth during this stage not only involves propagation through a decaying evanescent field, but also likely variations in the physical characteristics of each protein layer (packing density, surface coverage, protein orientation, etc.).

From the protein multilayer exponential fitting equation, we can determine that the 1/e decay length is 9.6 layers. In other words, after 9.6 protein layers, the evanescent intensity has decreased to 1/e (or ~37%) of its initial value at the ring surface. Using the 1/e distance of 63 nm determined experimentally with electrostatic polymer layers, these 9.6 monolayers each represent a 6.6-nm thickness on average (or ~13 nm per Ab/SA bilayer). IgG antibodies have a molecular weight (MW) of ~150 kDa with approximate molecular dimensions of 15 x 7 x 3.5 nm, and their four-polypeptide-chain structure is highly flexible.[41, 42] Streptavidin (MW ~ 53 kDa) is roughly one-third the size of an antibody with dimensions of 5.8 x 5.4 x 4.8 nm [43, 44], and a densely packed streptavidin monolayer has a thickness of 4.5-5 nm from studies using ellipsometry and electron microscopy.[45, 46] By simple addition of thicknesses, an Ab/SA bilayer is expected to be between 8 and 21 nm thick. Considering that the Abs are randomly oriented on

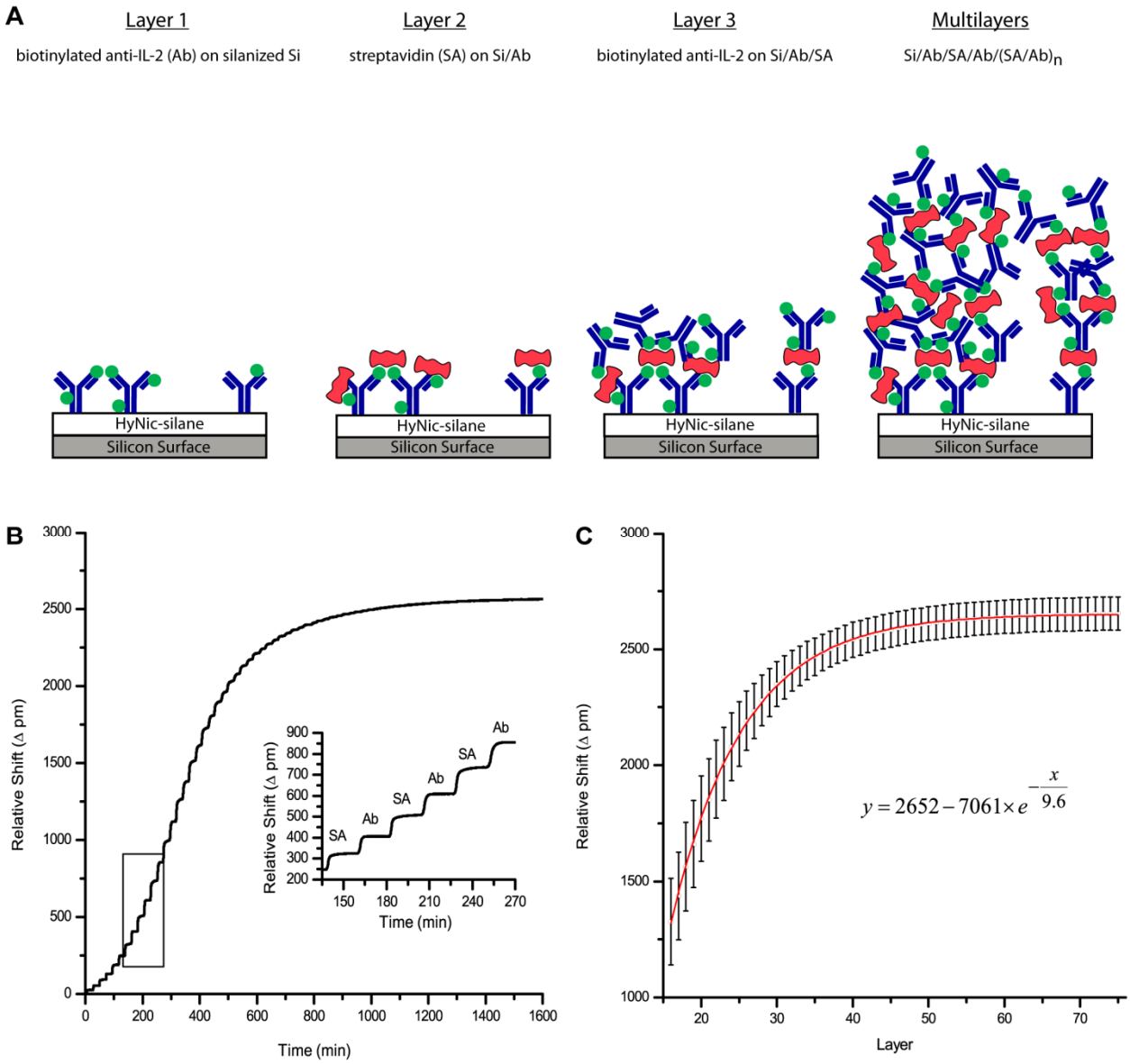

Figure 2.6 (A) Schematic showing the layer-by-layer addition of biotinylated antibody (Ab) and streptavidin (SA) to the ring resonator surface. Layer 1 shows covalent attachment of 4FB-modified, biotinylated antibody to the HyNic-silane functionalized silicon surface. We hypothesize that initial antibody functionalization yields incomplete surface coverage, which is followed by an annealing process that initially results in non-linear layer growth as vacancies are filled. Layers 2 and 3 show subsequent addition of streptavidin and biotinylated antibody, respectively. Extended multilayers are formed by alternating deposition of streptavidin and biotinylated antibody. Though each antibody is functionalized with ~10 biotins, fewer are shown for clarity. (B) Real time data showing the relative shift in resonance frequency (Δ pm) upon addition of SA and Ab layers. Inset shows six layer-by-layer depositions at higher resolution. (C) Plot showing the cumulative relative shift per antibody or streptavidin layer (each individual addition of streptavidin or antibody is counted as a single layer). The exponential fit shown in the plot indicates the decay rate starting from layer 16. Error bars represent the standard deviation for n = 4 rings.

the surface and that this disorder propagates with the addition of SA, the average thickness of 13 nm per bilayer seems quite reasonable.

Comparing the cumulative sensor response of the electrostatic polymer and the protein multilayers provides additional insights into the nature of the assemblies. In Figure 2.4C, the signal arising from 72 polymer bilayers effectively levels off at a maximum cumulative wavelength shift of ~10,000 pm. These 72 bilayers extend ~210 nm from the ring surface before the additional signal arising from subsequent layers becomes increasingly negligible due to the evanescent intensity decay. However, in the case of the protein multilayers, as depicted in Figure 2.6C, the cumulative wavelength shift arising from 37 protein bilayers levels off at ~2,700 pm, approximately four times less than the maximum signal from polymer multilayers. This implies that, given the similar refractive indices of the proteins and polymers ($n \approx 1.5$), the polymers form a higher density assembly that yields a larger total response within the bounds of the same evanescent field profile.

In contrast to the linear trend of the initial electrostatic polymer multilayers, the first 15 protein layers display a non-linear growth profile in which each layer yields a larger resonance wavelength shift than the previous layer. This effect can be observed in Figure 2.7, where the differential resonance shift between each layer is plotted as a function of layer number. Prior to bilayer 8 (the first 15 protein layers), each successive layer corresponds to an increasing differential shift despite the decreasing evanescent field intensity, with a maximum shift of 250 pm/protein bilayer at bilayer 8. Following this maximum shift, the observed resonance shift behavior is dominated by the decay of the evanescent intensity. We attribute this interesting multilayer assembly behavior to an increasing protein binding density throughout the early phase of growth (layers 1-15) where later layers are more complete than those initially deposited. We imagine initial antibody surface loading yields an incomplete monolayer, and subsequent biomolecular layers effectively anneal the initial holes in the film. After the addition of 15 protein layers (8 bilayers), we suspect that most holes have been filled as further layer growth appears linear. This means that subsequent resonance wavelength shifts for the remaining layers are completely dictated by the decay in the evanescent intensity. This model of linear layer growth following complete annealing by layer 15 is consistent with the measured shift in resonance wavelength for layers 16-75. A simple exponential decay function effectively fits the behavior of layers 16-75 (Figure 2.6C), where we assume linear growth of the protein

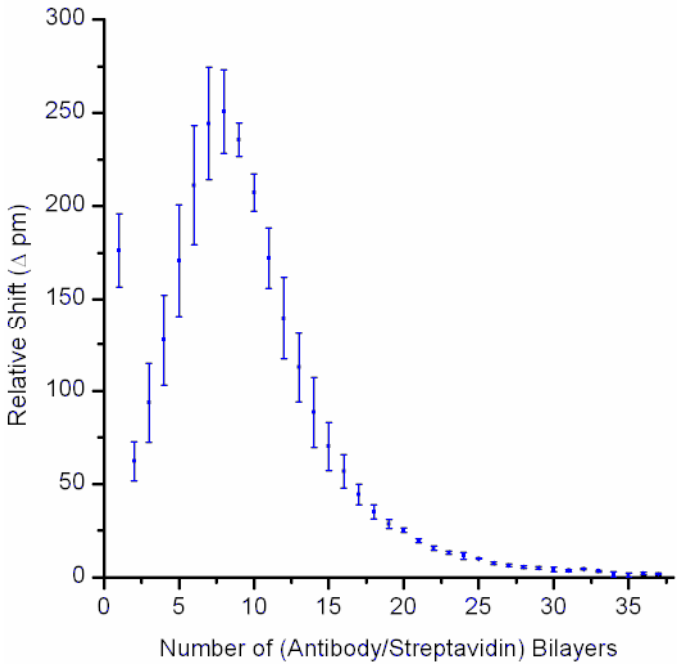

Figure 2.7 Plot displaying the relative differential shift per antibody/streptavidin bilayer. Notably, the signal increases initially to a maximum shift of ~250 pm at bilayer 8. Beyond this point the signal from subsequent layers decreases in an exponential fashion as they are deposited further away from the surface where there is a lower evanescent field intensity. Error bars represent the standard deviation for n = 4 rings.

multilayers and calculate an average protein layer thickness of 6.6 nm. This analysis reveals that our understanding of the evanescent intensity decay at increasing distances from the sensor surface allows for the isolation of contributions from non-linear layer growth and estimation of the protein layer thickness. Most importantly, however, we can directly observe the diminishing signal measured as capture agents are localized farther away from the sensor surface.

2.4.3 Absolute Mass Sensitivity via ^{125}I-labeled Streptavidin

Another metric that is valuable for comparing the relative performance of different sensing methodologies is the number of target molecules required to elicit a measureable sensor response. Clearly, the mode of signal transduction, the sensor configuration and geometry, and the size or mass of the target molecule play a critical role in determining how best to define this metric. Therefore, we decided to determine the absolute LOD of the microring resonator biosensing platform in terms of the minimum mass that can be detected. Since most biological molecules have similar refractive indices, we assert that this metric can be converted to the LOD in terms of the number of molecules for any bound analyte of known molecular weight.

In order to probe the mass sensitivity of the microring resonator platform, the amount of material bound at the surface must be carefully measured and correlated with the resonance wavelength shift upon binding. Our approach involves (1) measuring the wavelength shift of radioactive streptavidin binding to a biotinylated microring surface and then (2) determining the mass of bound streptavidin using standard radiometric techniques. Specifically, we used ^{125}I-labeled streptavidin and phosphorimaging to determine the amount of mass bound to the surface. The relationship between ^{125}I-streptavidin surface density and net resonance wavelength shift response was measured for three different sensor chips and used to determine the mass sensitivity and LOD for the biosensing platform.

The phosphorimager utilized for streptavidin mass quantitation has a spatial resolution of 50 µm, which is not sufficient to resolve individual microring sensing elements, especially considering that the fluoropolymer cladding material is only removed from an 8-µm wide annular opening over each microring (see Figure 1). Furthermore, we observed a non-zero radioactive response from the cladding material, meaning not all signal in a single phosphorimager pixel can be attributed to a microring. Therefore, we utilized RIE to remove the

cladding layer from one half of the chip before the surface was functionalized. Etching only half of the chip allowed half of the rings to remain unaltered to ensure that no binding artifacts or inconsistencies resulted from the etching process and to preserve unexposed thermal control rings for drift correction.

Given that the silicon microrings possess a native layer of silicon oxide, we feel it is a reasonable assumption that the binding density of ^{125}I-streptavidin on a microring will be comparable to that of the freshly-exposed bulk silicon oxide surface. To ensure that replicate measurements were independent of chip-to-chip variations, we tested the refractive index sensitivity of each chip by measuring the relative wavelength shift elicited by switching the surrounding solution from water to 1 M NaCl. All rings on all chips responded to 1 M NaCl with a 475 ± 25 pm shift. This variation falls well within the precision tolerance required to assess the absolute mass bound to the microring surface.

Each chip was functionalized with APTES and NHS-biotin, and then exposed to ^{125}I-streptavidin, creating a protein layer as shown in Figure 2.8A. To obtain a range of surface densities for calculating mass sensitivity, variable streptavidin loadings were produced by monitoring the real-time binding of streptavidin and initiating a buffer rinse after different exposure times (from 10 to 30 minutes). Figure 2.8B shows a representative binding curve where 1.2 µg/mL ^{125}I-streptavidin is introduced at t = 12. With varied streptavidin exposure times, we were able to obtain net sensor responses of 46 pm (low coverage), 165 pm (medium coverage), and 216 pm (high/saturated coverage). Following the buffer rinse and net binding shift determination, the chips were imaged, and the amount of bound mass was determined by comparison with spotted standards.

As shown in Figure 2.8C, ^{125}I-streptavidin bound to all areas over which flow was directed, including the half of the chip where the cladding layer was intact (although to a lesser extent). A rectangular region directly over the rings on the etched half of the substrate was selected on each chip, and the integrated total image intensity from the selected area was converted to a mass of bound streptavidin based on calibration with the ^{125}I-streptavidin standards (see Figure 2.9). Based on the pixel count of the sampled channel area and the pixel size of the phosphorimager, the bound mass was converted to a surface density. By dividing the surface density by the average net shift of the rings from within the sampled channel area, the

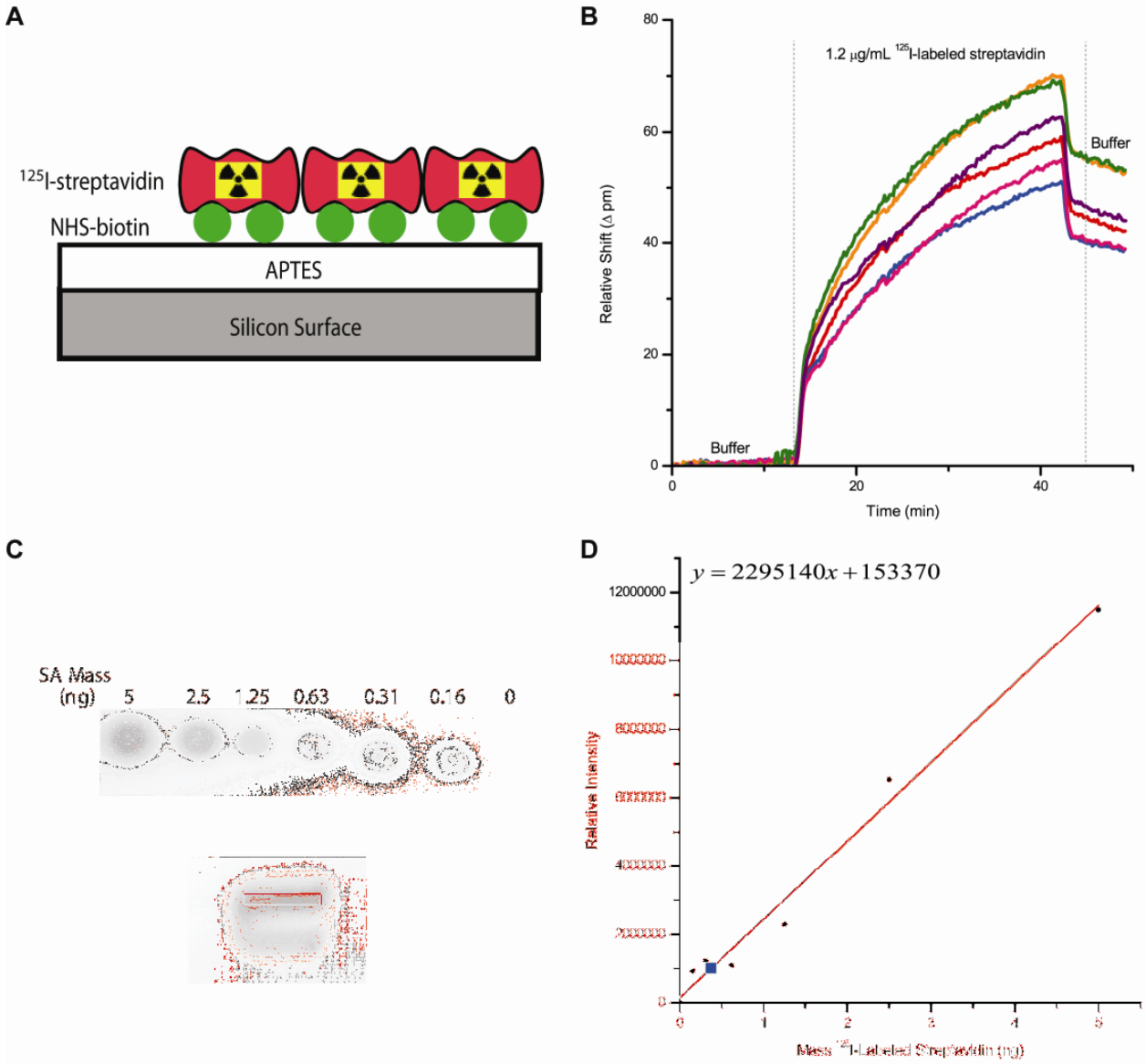

Figure 2.8 (A) Schematic showing the APTES-modified silicon surface coated with a layer of NHS-biotin followed by a layer of ^{125}I-labeled streptavidin. (B) Real time data showing binding of ^{125}I-labeled streptavidin to a biotin-functionalized surface. After rinsing the surface with buffer, the average net shift (relative shift after streptavidin minus relative shift before streptavidin) is measured for multiple rings. (C) Phosphorimage showing the relative intensity of ^{125}I-streptavidin standards compared with that bound on the U-shaped area of the chip to which flow was directed by microfluidics. The red rectangle highlights the region of interest directly over the rings on the chip where the radioactivity intensity was measured. In this selected area, the cladding layer was etched off exposing silicon oxide over the entire surface. (D) Calibration curve relating the mass of spotted protein standards (black dots) from (C) to the phosphorimager intensity obtained. The blue square represents the signal arising from the selected area (box in C).

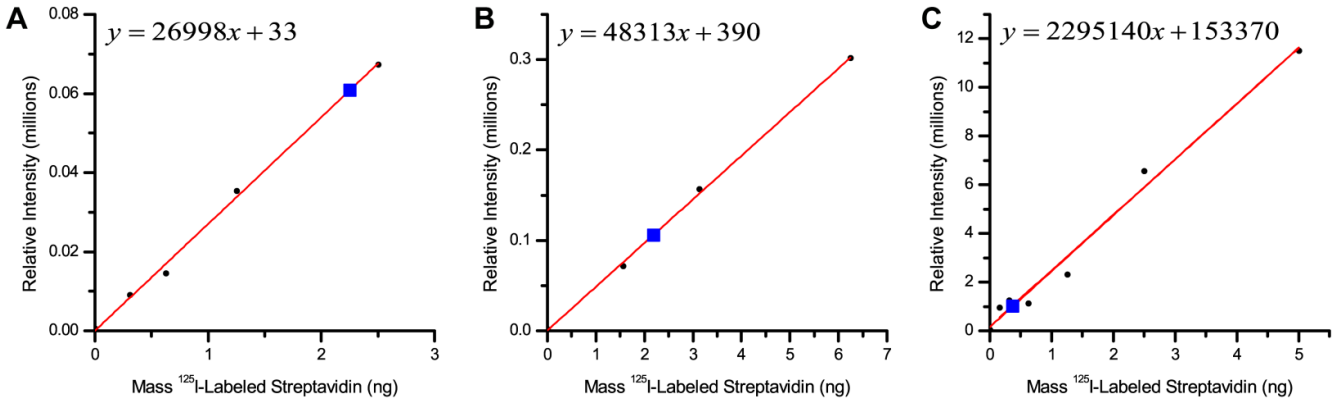

Figure 2.9 (A) Phosphorimager calibration curve for Chip 1, medium coverage ^{125}I-streptavidin (B) Calibration curve for Chip 2, high/saturated coverage ^{125}I-streptavidin (C) Calibration curve for Chip 3, low coverage ^{125}I-streptavidin (same as Figure 6D). The blue squares represent the phosphorimager intensity of the selected area on each chip used to calculate the mass of streptavidin bound.

Table 2.1 Radiolabeled Streptavidin Surface Density Data

Chip	Phosphorimager Intensity	^{125}I-SA Mass (ng)	Area Sampled (mm^2)	^{125}I-SA Density (pg/mm^2)	Average Net Shift (Δpm)	Sensitivity ($[pg/mm^2]/\Delta pm$)	Shift Resolution (Δpm)	LOD (pg/mm^2)
1	60844	2.25	0.65	3465	165	21.0	0.1	2.1
2	105948	2.18	0.65	3361	216	15.6	0.1	1.6
3	1011272	0.37	1.05	356	46	7.7	0.1	0.8

average mass sensitivity of the three chips was determined to be 14.7 ± 6.7 [pg/mm^2]/Δpm (see Table 2.1). Thus, a resonance wavelength shift of 1 pm represents 15 ± 7 pg/mm^2 of bound protein, or inversely, each 1 pg/mm^2 of protein density generates a 0.07 ± 0.03 pm shift in resonant wavelength.

To determine a LOD for the platform, we determined the noise floor to be 0.1 pm based on the minimal resolvable peak shift. To obtain the minimal resolvable peak shift, we utilize a calculation based on the ability to differentiate two different sets of data at the 95% confidence interval. Because measurements are made in real time, we can measure the average microring resonance wavelength shift value for 5 minutes (initial baseline) before a certain amount of substance is added to a ring surface, and then measure the average shift over a 5-min period after the addition of the substance to the surface. Given a baseline noise level with a standard deviation of 0.2 pm,[19] we can calculate the t-statistic for the two sets of data using the formula[47] as shown below:

$$t_{calculated} = \frac{\Delta\bar{x}}{s}\sqrt{n/2}$$

where $\Delta\bar{x}$ is the average difference between the two mean values, *s* is the pooled standard deviation (in this case, we assume that both the standard deviations and sample sizes are exactly the same, so the pooled standard deviation equals the standard deviation of the single sample), and *n* is the number of points in the sample. To be significantly different at the 95% confidence interval, $t_{calculated}$ must be greater than 2.02. Solving for $\Delta\bar{x}$ using *n* = 40 (number of data points for each ring collected in a 5-min span) and *s* = 0.2 pm, we get $\Delta\bar{x}$ = 0.09 pm. Thus, assuming a minimum resolvable peak difference of 0.1 pm for calculating the absolute mass sensitivity is a reasonable assumption.

Based on a 0.1 pm peak shift resolution, the platform's LOD was calculated at 1.5 ± 0.7 pg/mm^2.Using the surface area of 66 μm^2/ring and the surface density LOD described above, we determine the absolute mass LOD to be 97 ag of bound protein. This mass sensitivity signifies the ability to detect just 0.6 zmol (~400 molecules) of an antibody bound to the microring in a direct and label-free assay. The use of secondary antibodies in sandwich assay formats can

further augment the sensitivity of the platform to a protein target, especially for lower molecular weight protein targets.[20]

2.5 Conclusions

Through a combination of two multilayer studies on a silicon photonic microring resonator biosensing platform, the experimentally determined evanescent intensity decay profile was found to be in reasonable agreement with simulation results. The 1/e decay distance of binding sensitivity was measured to be 63 nm, highlighting the outstanding overlap of the waveguide mode with the biomolecular sensing region. Since most biological binding interactions with a capture probe (i.e. antibody, nucleic acid strand) and target analyte have dimensions on the order of tens of nanometers, this platform is well-suited for sensing specific binding events near the ring without large contributions from the surrounding environment.[48] Furthermore, with an empirical measure of the decay length characteristics of the microrings, it may be possible to design and optimize capture strategies to maximally utilize this property. For example, it is clear that assay designs involving non-fouling surface modifications (i.e. PEG chains, polymer brushes, etc) and secondary/tertiary signal amplification steps should take under consideration the strong evanescent decay distance dependence of sensor response. These considerations become especially clear in the protein multilayer data where the signal is reduced by 63% after only 5 SA/Ab bilayers. Understanding the decay length also enables elucidation of non-linear growth processes such as those observed in the protein multilayer system.

Beyond characterizing the sensing modality and the extent to which the evanescent intensity propagates through the sample, the inherent mass sensitivity of the platform was also empirically determined. Through the use of radio-labeled protein binding to the sensor surface, it was possible to directly relate a given resonance wavelength shift to an empirically determined protein surface density. This allowed for determination of the platform's inherent sensitivity, which is 15 [pg/mm^2]/Δpm. The high sensitivity of ring resonators to biological binding events at this early stage of technology development, with a ~1.5 pg/mm^2 LOD, is comparable to that of SPR [25] and other label-free techniques.[3, 8, 15] By improving peak resolution and reducing system noise, this sensitivity may be improved further. In both the multilayering and surface density

studies, the ability to monitor each ring's response in real time was vital to the characterization of platform performance metrics.

This paper presents important empirical determinations of key sensitivity metrics for a promising silicon photonic microring resonator chemical and biomolecular sensing platform. This information will be useful not only in comparing this platform to others, both optical and non-optical, but also provides key insights into the current limitations of sensor response which will be used to further optimize the technology for detection in complex, real-world environments.

2.6 References

(1) Passaro, V. M. N.; Dell'Olio, F.; Casamassima, B.; De Leonardis, F. *Sensors* **2007**, *7*, 508-536.

(2) Mukundan, H.; Anderson, A. S.; Grace, W. K.; Grace, K. M.; Hartman, N.; Martinez, J. S.; Swanson, B. I. *Sensors* **2009**, *9*, 5783-5809.

(3) Fan, X.; White, I. M.; Shopoua, S. I.; Zhu, H.; Suter, J. D.; Sun, Y. *Anal. Chim. Acta* **2008**, *620*, 8-26.

(4) Wolfbeis, O. S. *Anal. Chem.* **2008**, *80*, 4269-4283.

(5) Wolfbeis, O. S. *Anal. Chem.* **2006**, *78*, 3859-3873.

(6) Wolfbeis, O. S. *Anal. Chem.* **2002**, *74*, 2663-2677.

(7) Tsai, D. P.; Jackson, H. E.; Reddick, R. C.; Sharp, S. H.; Warmack, R. J. *Appl. Phys. Lett.* **1990**, *56*, 1515.

(8) Qavi, A. J.; Washburn, A. L.; Byeon, J.-Y.; Bailey, R. C. *Anal. Bioanal. Chem.* **2009**, *394*, 121-135.

(9) Jokerst, N. M.; Luan, L.; Palit, S.; Royal, M.; Dhar, S.; Brooke, M. A.; Tyler, T. *IEEE Trans. Biomed. Circuits Syst.* **2009**, *3*, 202-211.

(10) Densmore, A.; Xu, D. X.; Waldron, P.; Janz, S.; Cheben, P.; Lapointe, J.; Delage, A.; Lamontagne, B.; Schmid, J. H.; Post, E. *IEEE Photon. Technol. Lett.* **2006**, *18*, 2520-2522.

(11) Densmore, A.; Vachon, M.; Xu, D. X.; Janz, S.; Ma, R.; Li, Y. H.; Lopinski, G.; Delage, A.; Lapointe, J.; Luebbert, C. C.; Liu, Q. Y.; Cheben, P.; Schmid, J. H. *Opt. Lett.* **2009**, *34*, 3598-3600.

(12) Densmore, A.; Xu, D. X.; Janz, S.; Waldron, P.; Mischki, T.; Lopinski, G.; Delage, A.; Lapointe, J.; Cheben, P.; Lamontagne, B.; Schmid, J. H. *Opt. Lett.* **2008**, *33*, 596-598.

(13) Schmid, J. H.; Sinclair, W.; García, J.; Janz, S.; Lapointe, J.; Poitras, D.; Li, Y.; Mischki, T.; Lopinski, G.; Cheben, P.; Delâge, A.; Densmore, A.; Waldron, P.; Xu, D. X. *Opt. Express* **2009**, *17*, 18371-18380.

(14) De Vos, K. M.; Bartolozzi, I.; Bienstman, P.; Baets, R.; Schacht, E. *Proc. SPIE* **2007**, *6447*, 64470K.

(15) Carlborg, C. F.; Gylfason, K. B.; Kazmierczak, A.; Dortu, F.; Polo, M. J. B.; Catala, A. M.; Kresbach, G. M.; Sohlstrom, H.; Moh, T.; Vivien, L.; Popplewell, J.; Ronan, G.; Barrios, C. A.; Stemme, G.; van der Wijngaart, W. *Lab Chip* **2010**, *10*, 281-290.

(16) De Vos, K.; Girones, J.; Popelka, S.; Schacht, E.; Baets, R.; Bienstman, P. *Biosens. Bioelectron.* **2009**, *24*, 2528-2533.

(17) Ramachandran, A.; Wang, S.; Clarke, J.; Ja, S. J.; Goad, D.; Wald, L.; Flood, E. M.; Knobbe, E.; Hryniewicz, J. V.; Chu, S. T.; Gill, D.; Chen, W.; King, O.; Little, B. E. *Biosens. Bioelectron.* **2008**, *23*, 939-944.

(18) Xu, D. X.; Densmore, A.; Delâge, A.; Waldron, P.; McKinnon, R.; Janz, S.; Lapointe, J.; Lopinski, G.; Mischki, T.; Post, E.; Cheben, P.; Schmid, J. H. *Opt. Express* **2008**, *16*, 15137-15148.

(19) Iqbal, M.; Gleeson, M. A.; Spaugh, B.; Tybor, F.; Gunn, W. G.; Hochberg, M.; Baehr-Jones, T.; Bailey, R. C.; Gunn, L. C. *IEEE J. Sel. Top. Quantum Electron* **2010**, *16*, 654-661.

(20) Luchansky, M. S.; Bailey, R. C. *Anal. Chem.* **2010**, *82*, 1975-1981.

(21) Qavi, A. J.; Bailey, R. C. *Angew. Chem. Int. Ed.* **2010**, *49*, 4608-4611.

(22) Washburn, A. L.; Gunn, L. C.; Bailey, R. C. *Anal. Chem.* **2009**, *81*, 9499-9506.

(23) Washburn, A. L.; Luchansky, M. S.; Bowman, A. L.; Bailey, R. C. *Anal. Chem.* **2010**, *82*, 69-72.

(24) Scarano, S.; Mascini, M.; Turner, A. P. F.; Minunni, M. *Biosens. Bioelectron.* **2010**, *25*, 957-966.

(25) Homola, J. *Chem. Rev.* **2008**, *108*, 462-493.

(26) Piliarik, M.; Homola, J. In *Surface Plasmon Resonance Based Sensors*, 2006, pp 95-116.

(27) Homola, J. In *Surface Plasmon Resonance Based Sensors*, 2006, pp 3-44.

(28) Fu, E.; Chinowsky, T.; Nelson, K.; Yager, P. In *Handbook of Surface Plasmon Resonance*; Schasfoort, R. B. M., Tudos, A. J., Eds.; Royal Society of Chemistry, 2008, pp 313-332.

(29) Mandal, S.; Goddard, J. M.; Erickson, D. *Lab Chip* **2009**, *9*, 2924-2932.

(30) Ganesan, P. G.; Wang, X.; Nalamasu, O. *Appl. Phys. Lett.* **2006**, *89*, 213107-213103.

(31) Ramsden, J. J.; Lvov, Y. M.; Decher, G. *Thin Solid Films* **1995**, *254*, 246-251.

(32) Byeon, J.-Y.; Limpoco, F. T.; Bailey, R. C. *Langmuir* **2010**, *26*, 15430-15435.

(33) Vörös, J. *Biophys. J.* **2004**, *87*, 553-561.

(34) Arnold, S.; Khoshsima, M.; Teraoka, I.; Holler, S.; Vollmer, F. *Opt. Lett.* **2003**, *28*, 272-274.

(35) Marcatili, E. A. J. *Bell Labs Technical Journal* **1969**, *48*, 2071-2102.

(36) Decher, G.; Schmitt, J. In *Trends in Colloid and Interface Science VI*, 1992, pp 160-164.

(37) Ladam, G.; Schaad, P.; Voegel, J. C.; Schaaf, P.; Decher, G.; Cuisinier, F. *Langmuir* **1999**, *16*, 1249-1255.

(38) Wong, J. E.; Rehfeldt, F.; Hanni, P.; Tanaka, M.; Klitzing, R. V. *Macromolecules* **2004**, *37*, 7285-7289.

(39) Wang, F.; Li, L.; Gao, C. *Macromol. Chem. Phys.* **2009**, *210*, 2022-2028.

(40) Kolasinska, M.; Krastev, R.; Gutberlet, T.; Warszynski, P. *Prog. Colloid Polym. Sci.* **2008**, *134*, 30-38.

(41) Jung, Y.; Jeong, J. Y.; Chung, B. H. *Analyst* **2008**, *133*, 697-701.

(42) Saphire, E. O.; Stanfield, R. L.; Crispin, M. D. M.; Parren, P. W. H. I.; Rudd, P. M.; Dwek, R. A.; Burton, D. R.; Wilson, I. A. *J. Mol. Biol.* **2002**, *319*, 9-18.

(43) Hendrickson, W. A.; Pähler, A.; Smith, J. L.; Satow, Y.; Merritt, E. A.; Phizackerley, R. P. *Proc. Natl. Acad. Sci. U. S. A.* **1989**, *86*, 2190-2194.

(44) Cassier, T.; Lowack, K.; Decher, G. *Supramol. Sci.* **1998**, *5*, 309-315.

(45) Herron, J. N.; Mueller, W.; Paudler, M.; Riegler, H.; Ringsdorf, H.; Suci, P. A. *Langmuir* **1992**, *8*, 1413-1416.

(46) Darst, S. A.; Ahlers, M.; Meller, P. H.; Kubalek, E. W.; Blankenburg, R.; Ribi, H. O.; Ringsdorf, H.; Kornberg, R. D. *Biophys. J.* **1991**, *59*, 387-396.

(47) Harris, D. C. *Quantitative Chemical Analysis*, 5th ed.; W. H. Freeman and Company: New York, 1999.

(48) Kunz, R.; Cottier, K. *Anal. Bioanal. Chem.* **2006**, *384*, 180-190.

Chapter 3

Label-Free Quantitation of a Cancer Biomarker in Complex Media using Silicon Photonic Microring Resonators

Notes and Acknowledgements

This chapter has been reproduced from the original paper "Label-Free Quantitation of a Cancer Biomarker in Complex Media using Silicon Photonic Microring Resonators" (Washburn, A. L.; Gunn, L. C.; Bailey, R. C. Anal. Chem. **2009**, *81*, 9499–9506). It has been reproduced here with permission from the American Chemical Society © 2009.

Cary Gunn is acknowledged in behalf of Genalyte, Inc. for getting the microring resonator project initiated.

This work in this chapter was funded by the NIH Director's New Innovator Award Program, part of the NIH Roadmap for Medical Research, through grant number 1-DP2-OD002190-01 and the Camille and Henry Dreyfus Foundation. ALW was supported via a National Science Foundation Graduate Research Fellowship. We acknowledge Matthew Luchansky for his assistance in creating the unknown CEA solutions and Ji-Yeon Byeon for the SEM image of the microring resonator. This research was carried out in part in the Frederick Seitz Materials Research Laboratory Central Facilities, University of Illinois, which are partially supported by the U.S. Department of Energy under grants DE-FG02-07ER46453 and DE-FG02-07ER46471.

This article can be accessed online at: http://dx.doi.org/10.1021/ac902006p

3.1 Introduction

Fluorescent,[1] nanoparticle,[2] or enzymatic labels[3] are utilized in many common biomolecular assays and can provide exceptional sensitivity down to the single molecule level. However, they may also introduce challenges in terms of cost, complexity, labeling heterogeneity,[4] and perturbations to the native biomolecular interaction of interest.[5] For these reasons, the development of label-free approaches for bioanalysis, especially those that can measure multiple analytes simultaneously, has been an active area of research over the past 20 years.[6] Particularly relevant to this report are optical methods of label-free analysis,[7] including surface plasmon resonance,[8] photonic crystals,[9] and interferometric devices,[10] which have all been utilized to sensitively detect biomolecules as well as determine binding kinetics.

High quality factor (Q factor) microcavity resonators represent a promising class of optical devices that have only recently been utilized for biomolecular analysis.[11, 12] In microcavity resonator sensors, which include microspheres,[13-15] microtoroids,[16] capillaries,[17-21] microdisks,[22, 23] and microrings,[24-30] light is coupled into the cavity via an adjacent linear waveguide positioned within the evanescent field. Optical modes are supported along the circumference of the cavity according to the resonance condition:

$$m\lambda = 2\pi r n_{eff}$$

where m is an integer, λ is wavelength of light, r is the radius of the resonator, and n_{eff} is the effective refractive index. Precise fabrication leads to high Q factor cavities which, from a practical analytical standpoint, lead to a dramatic increase in the effective optical pathlength as well as a sharpening of the resonance to an extraordinarily narrow spectral dispersion. Chemical and biomolecular binding events at the surface of the microcavity lead to an increase in the effective refractive index, n_{eff}, and thus a shift in the resonance frequency, as shown in Figure 3.1A. The narrow resonance allows resolution of small shifts, and thus tiny binding-induced changes in n_{eff}, can be clearly discerned, directly facilitating highly sensitive detection.

Silicon-on-insulator (SOI) optical microring resonators are an attractive technology for applications in label-free biomolecular analysis holding significant promise for multiplexed biomolecular detection. Since both the ring and waveguide are physically anchored to the same underlying substrate (see SEM image in Figure 3.1B), these devices can be routinely fabricated

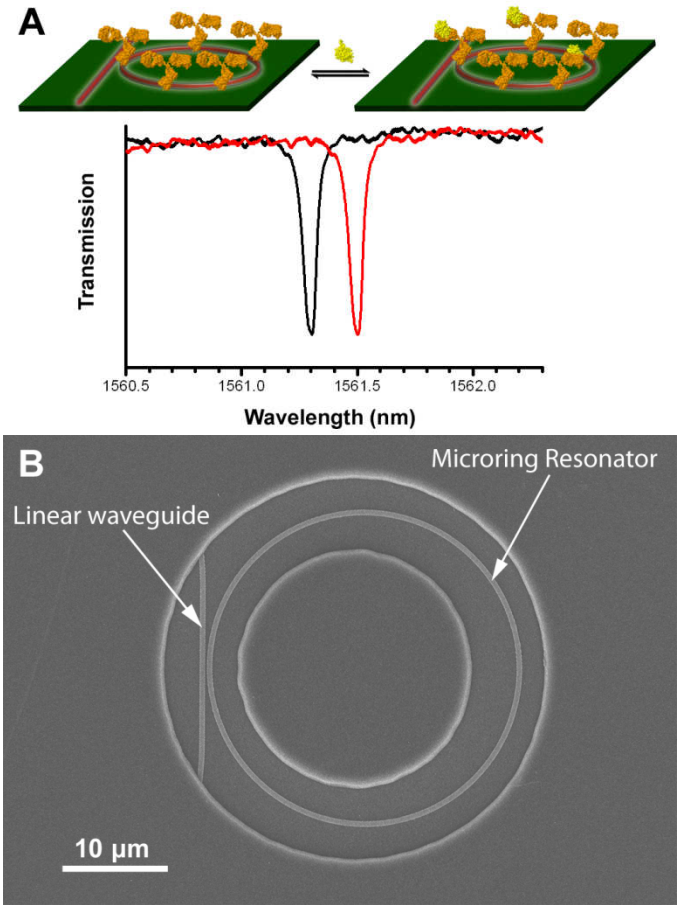

Figure 3.1 (A) Schematic diagram illustrating the principle of microring optical resonator biosensing, including a representative transmission spectrum. (B) Top-view scanning electron micrograph image of a microring resonator and linear waveguide, visible through an annular opening in the fluoropolymer cladding layer.

using well-characterized semiconductor processing techniques and easily interrogated via chip-integrated optics.

Prior reports of optical microring resonators for protein sensing have generally focused on proof-of-principle demonstrations, such as measurements in buffer of avidin-biotin interactions[24, 26-28] or detection of polyclonal IgG.[30] Besides demonstrating the ability to monitor in real time the steps involved in the chemical and biomolecular functionalization of the sensor surface, we also utilize multiple types of integrated on-chip control sensors for nonspecific response normalization and implement a time-based quantitation method that enables rapid calibration and precise concentration determination. As a demonstration of the impact of these features, we focus on the direct and label-free quantitation of carcinoembryonic antigen (CEA), a 185 kDa glycoprotein that is secreted into the blood and has been established as a biomarker for many human cancers, including colorectal,[31] cervical,[32] lung,[33] and breast[34] cancers. We show that the detection limit of our platform is comparable to that of a commercial enzyme-linked immunosorbent assay (ELISA) kit and is satisfactory for the quantitation of CEA over the clinically-relevant range of 5-100 ng/mL. We also report for the first time operation of microring optical resonators in undiluted fetal bovine serum and show that CEA can be detected in this complex medium at concentrations found in patients with advanced cancers, from 20 to well over 70 ng/mL.[35] This report establishes microring resonator arrays as a promising tool for a variety of real-world protein detection applications.

3.2 Materials and Methods Sections

3.2.1 Materials

The silane 3-aminopropyltriethoxysilane (APTES), was purchased from Gelest (Morrisville, PA). Succinimidyl 6-hydrazinonicotinamide acetone hydrazone (S-HyNic) and succinimidyl 4-formylbenzoate (S-4FB) were purchased from SoluLink (San Diego, CA). Monoclonal mouse antibody to human CEA (Cat# M37401M) and human CEA (Cat# A32030H) were purchased from Meridian Life Science (Saco, ME). CEA ELISA kits were purchased from GenWay Biotech (San Diego, CA) and Signosis (Sunnyvale, CA). Fetal bovine serum (FBS) was purchased from Gemini Bio-Products (West Sacramento, CA). Zeba spin filter columns were purchased from Pierce (Rockford, IL). PBS was reconstituted from Dulbecco's Phosphate

Buffered Saline packets purchased from Sigma-Aldrich (St. Louis, MO). All other chemicals were obtained from Sigma-Aldrich and used as received.

All buffers were made with purified water (ELGA PURELAB filtration system; Lane End, UK), and the pH was adjusted using 1 M HCl or 1 M NaOH. PBS pH 7.4. Acetate buffer consisted of 50 mM sodium acetate and 150 mM sodium chloride adjusted to pH 4.75. Glycine buffer was 10 mM glycine and 160 mM NaCl adjusted to pH 2.2. BSA-PBS buffer was made by dissolving solid bovine serum albumin (BSA) in PBS (pH 7.4) to a final concentration of 0.1 mg/mL.

3.2.2 Substrate Design, Fabrication, and Sensor Chip Layout

Microring resonator array substrates were designed as previously described[36] and fabricated on 8" silicon-on-insulator (SOI, 200 nm thick top-layer Si) wafers by the silicon foundry at LETI (Grenoble, France). The entire 8" wafer was spin-coated with a fluoropolymer cladding material, and windows were opened over selected individual sensor elements via photolithography and reactive ion etching. Individual sensor chips having sixty-four 30 µm diameter microrings on a 6 x 6 mm footprint were diced from the 8" wafers by Grinding and Dicing Services, Inc. (San Jose, CA). Next to each microring was a linear waveguide that had input and output diffractive grating couplers at either end, allowing the optical cavity spectrum of each microring resonator to be determined independently.

3.2.3 Instrumentation

The instrumentation used to measure shifts in microring resonance frequency is described in detail in a separate manuscript.[36] Briefly, the beam of a tunable, external cavity diode laser operating with a center frequency of 1560 nm is rapidly rastered across the surface and the back reflection is monitored as a function of position to image the substrate. This image is used to register the location of the input and output grating couplers associated with each individual microring. To determine the resonance frequency of an individual microring, the beam is focused onto a single input grating coupler. The intensity of light projected off of the chip by the corresponding output grating coupler is measured as the frequency of the laser is rapidly swept

through a suitable spectral bandwidth. In this mode of operation, a resonance appears as a decrease in the intensity of light projected out of the output coupler at a given laser frequency, since under resonance conditions light is nearly completely coupled into the microring and no longer propagates down the adjacent linear waveguide. Resonance frequencies and shifts in frequency are determined and displayed on-screen in near real time with up to ~250 ms resolution using the provided instrument control software. Multiple resonator sensors in an array are probed by serially positioning the laser beam on different input grating couplers that address unique microrings and then the resonance frequency is recorded as described above. Up to 32 microring sensors can be monitored during an experiment. Eight of the sensors monitored are not exposed to the solution and serve as controls for thermal drift.

Sensor chips are loaded into a custom cell with microfluidic flow channels defined by a 0.010" thick laser-cut Mylar gasket (fabricated by RMS Laser; El Cajon, CA) that is aligned over top of the microring arrays and sandwiched between an aluminum chip holder and a Teflon lid (see Figure 3.2 for a diagram of the microring layout, including an overlay of the Mylar gasket). Solutions are introduced to the chip at controlled flow rates using an 11 Plus syringe pump (from Harvard Apparatus; Holliston, MA) operated in withdraw mode.

3.2.4 Surface Functionalization and Biomolecule Attachment

To remove any residual organic contaminants remaining from fabrication, silicon microring surfaces are first cleaned by a one-minute immersion in piranha solution[37] (3:1 H_2SO_4:30% H_2O_2) and are then rinsed with copious amounts of water and dried under a stream of nitrogen. Following cleaning, the silicon microrings are then organically modified using standard silanization chemistry. The entire chip is exposed to a 2% solution of APTES in 95% ethanol for 10-20 min, followed by a removal of residual siloxane by rinsing in 95% ethanol. Covalent attachment of biomolecules to the sensor surface is achieved in two steps using hydrazone-bond-formation chemistry. The freshly silanized surfaces are exposed to a 17 mM solution of S-HyNic in PBS (with 4% dimethylformamide (DMF) to dissolve S-HyNic) for 3–4 h. In parallel, a reactive aldehyde moiety is conjugated to the antibody (1 mg/mL) by reaction with a 5-fold molar excess of S-4FB (dissolved first in DMF and diluted in PBS to less than 5% DMF). This S-4FB:protein ratio introduces an average of two pendant reactive aldehyde groups

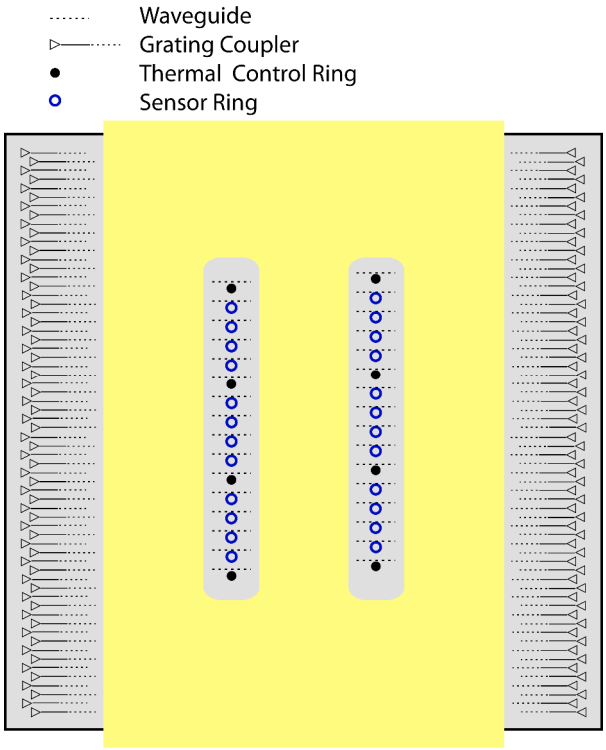

Figure 3.2 Schematic (not to scale) showing a layout of 32 microrings on a 6 × 6 mm silicon chip. The yellow overlay indicates the portion of the Mylar gasket used to define flow channels. The entire gasket is not shown as it extends beyond the boundaries of the chip. A duplicate set of 32 microrings (offset by 0.5 mm) are also not shown as they are hidden beneath the Mylar gasket.

per antibody, according to the manufacturer, and was empirically determined to be optimal. After reacting for 2 h at room temperature, unreacted S-4FB is removed by buffer-exchanging the antibody into acetate buffer using Zeba spin filter columns. HyNic-functionalized surfaces are exposed to solutions of 4FB-functionalized antibodies (generally 0.1 mg/mL or higher) for at least 1 h to maximize the amount of covalently immobilized antibody. A glycine buffer rinse is then used to remove noncovalently bound antibody. A final blocking step is accomplished by exposing the sensor surface to a 2% solution (w/w) of BSA in PBS. In a typical assay, half of the sensor rings are functionalized with antibody while the other half are not exposed to antibody. These nonfunctionalized sensors are used as internal references to correct for temperature and instrument drift, as well as for bulk refractive index shifts associated with switching solutions.

All silanization and HyNic conjugation reactions, as well as detection experiments, are performed in linear microfluidic channels defined by the Mylar gasket. For experiments in which antibodies are immobilized only onto certain regions of the substrate, a different Mylar gasket is used that directs fluid to only selected portions of the sensor chip. While microfluidics alone provide adequate spatial resolution for the measurements in this paper, preliminary work in our group has indicated that higher order multiplexing can be achieved by interfacing with conventional microarray spotting technologies.

3.2.5 CEA Detection

For CEA detection experiments in buffer, BSA-PBS (0.1 mg/mL BSA in PBS) was used as a running buffer to help prevent nonspecific adsorption of protein in the tubing and flow cell. CEA solutions were made by serial dilution in BSA-PBS starting from an original 2.5 mg/mL stock solution. Those solutions were then flowed through the sample chamber and over the sensor chip surface at a rate of 30 µL/min. For CEA detection in serum, 100% FBS was used as a running buffer. To detect CEA in serum, CEA-spiked FBS samples were made by adding CEA stock solution to 100% FBS. Additional solutions were made by directly diluting the CEA-spiked FBS stock solution with 100% FBS to dilute the CEA to the appropriate concentration. Because of the viscosity of 100% FBS, the flow rate was reduced to 10 µL/min for sensing experiments in serum. For all of the sensing assays, the original surfaces were regenerated after CEA exposure using a 1–2 minute rinse of glycine buffer that disrupted protein-antibody

complexes, followed by a return to the running buffer to reestablish the sensor baseline. Single-blind solutions having unknown CEA concentrations were generated—by a laboratory worker otherwise not involved in this study—by adding an aliquot of an original stock solution into either BSA-PBS buffer or 100% FBS.

For the CEA ELISA, absorbance was measured at 450 nm using a SpectraMax Plus384 spectrophotometer from (Molecular Devices; Sunnyvale, CA).

3.2.6 Data Processing

All microring detection data was corrected for drift related to thermal and instrumental fluctuations, as well as minimal amounts of non-specific binding by referencing to “unmodified” rings that were exposed to solution in the same sample flow chamber but were masked during the antibody immobilization step. Graphs of sensor responses have been processed post-acquisition by subtracting the unmodified reference ring responses from the antibody-conjugated sensor rings. All data fitting was performed using the OriginPro 8 software package (OriginLab Corporation; Northampton, MA).

3.3 Results and Discussion

3.3.1 Surface Derivatization of Microring Resonator Surface

For sensitive detection of biomolecules, a robust capture agent immobilization strategy is needed. Figure 3.3 schematically outlines the multiple steps used to covalently attach antibodies to the silicon surface of a microring sensor. As shown in Figures 3.3A and 3.3B, the oxide-passivated silicon surface is first modified with 3-aminopropyltriethoxysilane (APTES). Because addition of organic molecules and biomolecules to the sensor surface changes the local refractive index, each surface reaction can be monitored in real time. Figure 3.4A shows the real-time response of twelve individual microrings simultaneously exposed to a 2% solution of APTES. Following addition of the silane, an immediate shift in resonance frequency is observed that contains contributions from the bulk refractive index change associated with the 2% APTES as

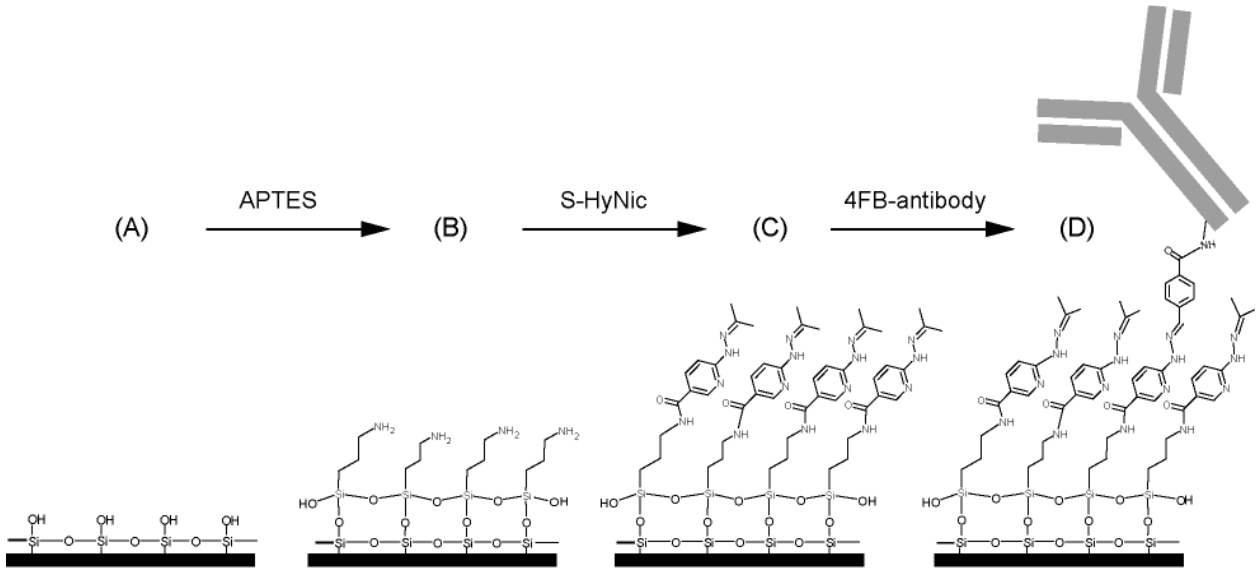

Figure 3.3 Schematic showing surface functionalization. (A) Silicon surface of microring sensors prior to modification. (B) APTES reacts with the surface siloxane groups to generate an amino-terminated surface. (C) S-HyNic reacts with primary amines to create a HyNic-displaying surface. (D) Addition of 4FB-modified antibodies results in hydrazone bond formation between the 4FB moieties on the antibodies and the HyNic moieties on the surface.

well as from rapid surface silanization. As the sensors are rinsed with 95% EtOH and returned to the original bulk refractive index environment, the sensors decrease in signal but a residual shift in the resonance wavelength of approximately 75 pm indicates the covalent attachment of APTES to the surface.

As indicated by the schematic in Figure 3.3C, the amine-reactive succinimidyl 6-hydrazinonicotinamide acetone hydrazone (S-HyNic) is added to the APTES-functionalized surface. This hydrazide group is then used to covalently immobilize the antibody capture agent using hydrazone-bond-formation chemistry. Figure 3.4B shows in real time the addition of S-HyNic to the same twelve microrings shown in Figure 3.4A. Similar to the silanization reaction, a large bulk refractive index shift is observed, but this time it is even larger due to the transition from PBS to PBS containing 4% DMF and S-HyNic. The bulk shift is followed by a much slower increase over approximately two hours due to the reaction of the succinimidyl esters of the S-HyNic reacting with surface amines. Returning to PBS reveals a residual shift of 50–100 pm which is the result of covalently immobilized HyNic. The reasons behind the differential response at each ring are still under investigation, but it likely is the result of heterogeneous chemical reactivity of individual sensors.

Following the generation of a hydrazine-presenting surface, antibodies tagged with succinimidyl 4-formylbenzoate (S-4FB) are covalently coupled to the surface via hydrazone bond formation between the aryl aldehydes on the antibodies and the hydrazine moieties on the surface, as illustrated in Figure 3.3D. Figure 3.4C shows the real-time data for the addition of 4FB-tagged anti-CEA antibodies to five identical HyNic-modified microrings resulting in a 300–350 pm shift in the resonance frequencies of each ring. A rinse with glycine buffer helps remove any noncovalently bound antibody, and after returning to the original acetate buffer, the remaining 260–280 pm shift for each ring corresponds to antibody attached to the microring surface via a hydrazone bond linkage.

By monitoring each surface derivatization step, it is possible to verify that each individual chemical modification of the surface has occurred. In addition, it is possible to determine the sensor-to-sensor consistency of antibody loading. Since inconsistency in antibody loading is a common source of assay variability, this is a very significant feature of our detection system that will be critical for future work in the creation of robust and reproducible multiplexed sensor arrays.

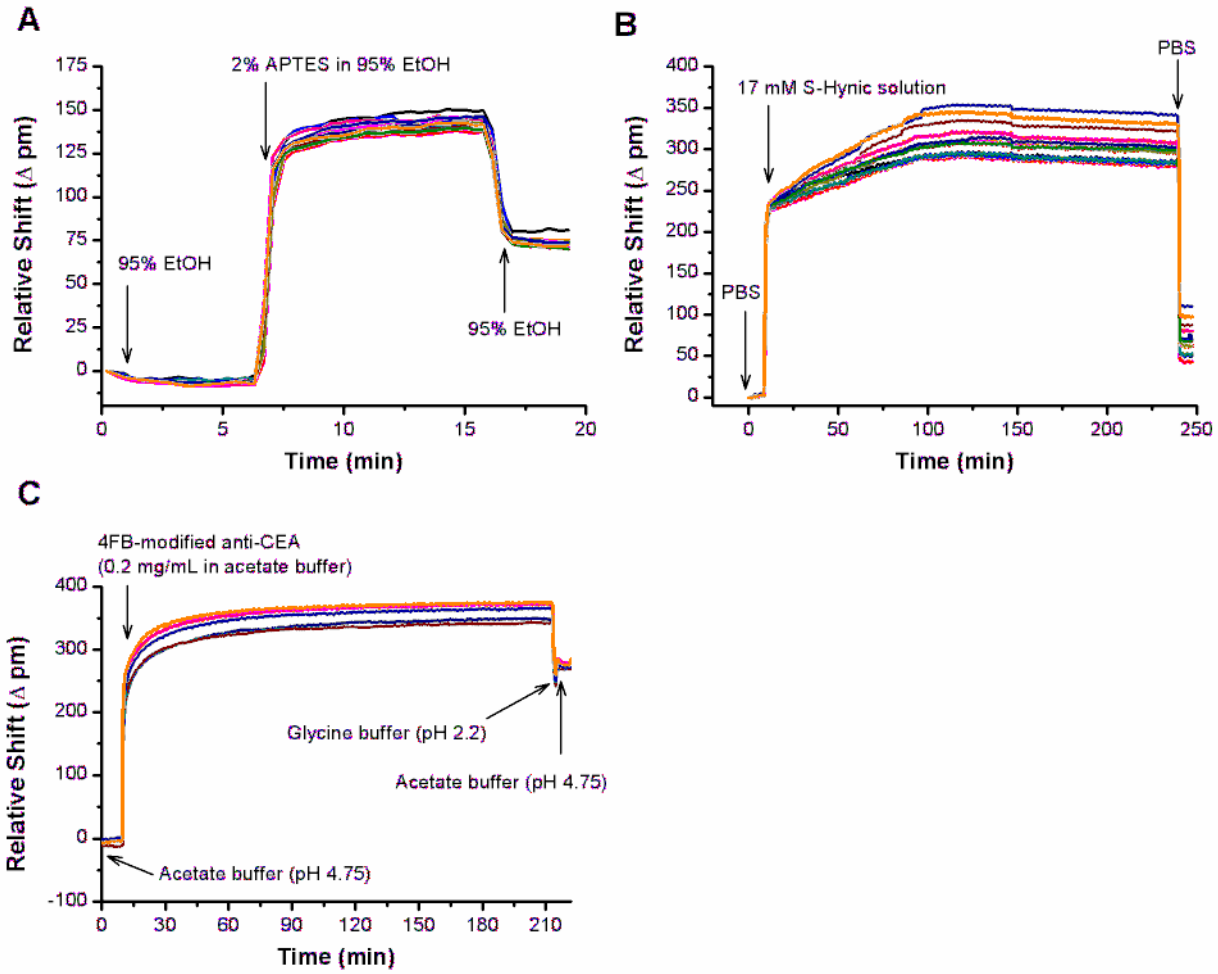

Figure 3.4 (A) Real-time monitoring of the shift in resonance frequency for twelve microrings within the same sample flow chamber during organic modification via reaction with APTES. The microrings were initially submerged in 95% ethanol solution and a 2% solution of APTES injected at t = 6.5 min. The silane was flushed from the chamber and microrings returned to 95% ethanol after 10 min. (B) Real-time observation of the reaction between S-HyNic (introduced at t = 10 min) and the surface amine groups as followed by monitoring the shift in resonance frequency. (C) Real-time shift in resonance frequency from five individual microrings during covalent immobilization of antibody onto the sensor surfaces. The 4FB-tagged anti-CEA antibody was added at t = 10 min and removed (sample chamber returned to acetate buffer) at t = 210 min.

Following the immobilization of anti-CEA antibodies, microring sensors were tested to verify that the immobilized antibody was still functional and that the sensors were responsive to antigen binding. Figure 3.5 shows the uncorrected (no control ring subtraction) response of anti-CEA functionalized microrings to a 1 μg/mL solution of CEA in BSA-PBS at t = 5 min, followed by regeneration with glycine buffer at t = 12 min with a return to BSA-PBS at t = 14 min. The exposure to CEA induces a specific response from five individual antibody-functionalized microrings, each displaying a net frequency shift of ~100 pm after 7 min of binding. Notably, the relative response of each of the rings is extremely similar, consistent with the observed antibody loading shown in Figure 3.4C. Also shown in Figure 3.5 are the responses of five individual control rings that are in the same channel as the five rings that showed a specific response. These microrings are identical except that they were not exposed to the 4FB-tagged antibody solution, and they showed no response during the same exposure to antigen. Thus, for all following biomolecular binding/detection experiments in this chapter, these unmodified rings are used as references. An important advantage of using an array of microring sensors is that unmodified rings can be used as reference rings in order to subtract out any systematic instrumental or thermal drift, as well as to remove sensor response caused by a change in the bulk refractive index or from small amounts of nonspecific binding.

3.3.2 Quantitative Detection of a Cancer Biomarker

To make quantitative measurements of CEA, microring resonators were covalently functionalized with anti-CEA antibodies as described. To demonstrate the dynamic range for this sensing technique, aliquots of CEA were sequentially flowed over the sensor array at concentrations of 45, 114, 228, 575, and 1183 ng/mL in BSA-PBS, and the shift in resonance frequencies of several microrings were monitored in real-time. At each concentration, the CEA solution was flowed for 25 minutes of binding followed by a quick (1–2 minute) rinse with glycine to regenerate the original antibody-presenting sensor surface and a 5-10 minute rinse with BSA-PBS to reestablish the baseline. Figure 3.6 shows a representative response from a single microring during the entire concentration exposure series. This dose and regeneration protocol was repeated three times in order to obtain all association curves in triplicate for post-acquisition data analysis.

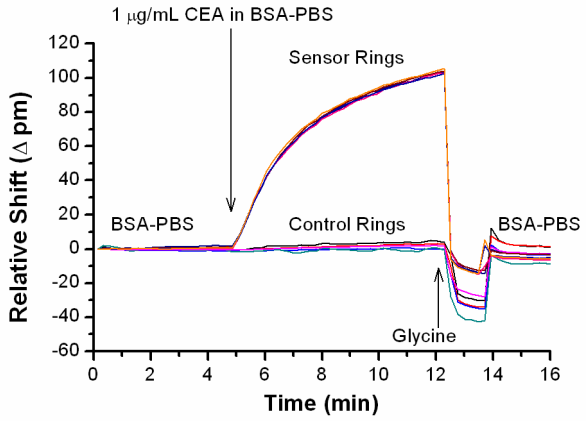

Figure 3.5 Time-resolved detection of CEA using five anti-CEA-functionalized microrings alongside five control microrings that were not functionalized with antibody. Following exposure to CEA, the antibody surface was regenerated by exposure to glycine buffer for two minutes before returning to BSA-PBS.

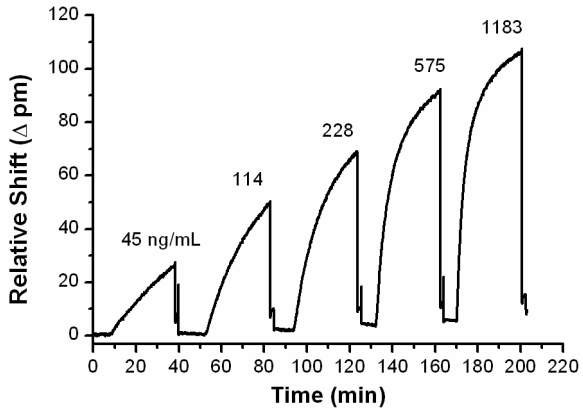

Figure 3.6 Real-time monitoring of resonance frequency shifts of an anti-CEA antibody-functionalized microring upon exposure to increasing concentrations of CEA in BSA-PBS. After exposure to antigen, the antigen-antibody interaction was disrupted with glycine buffer, regenerating the original sensor surface, and the sample chamber was returned to BSA-PBS to reestablish the sensor baseline.

To demonstrate the consistency of the observed CEA detection response, the data from a single microring during each of the three concentration series runs was overlaid, as shown in Figure 3.7A. The good agreement in both the magnitude and shape of the association curves allows CEA concentration determination with high precision. From the data in Figure 3.7A, a calibration curve was generated based upon the initial slopes of the association curves. As described by Fick's first law, under the mass-transport limiting conditions usually present in trace biomolecular analysis, the initial slope is linearly proportional to the concentration of the analyte in solution.[38] The resulting concentration-response calibration curve is generally linear over a wide dynamic range, and thus the method is advantageous for real-time detection assays.[30, 39-41] In addition, we have found that using an initial slope-based method provides increased precision as compared to fixed-time-point measurements for the 10-minute assays described in this paper. This increased precision is largely because the initial slope is determined from multiple data points over a given time range, whereas equilibrium-based measurements typically measure the response at a single time point, or over a discrete time range, during which the response is growing. For our system, multiple measurements based on initial slope typically have standard deviations about 3–6 times smaller than the standard deviations based on multiple measurements using a fixed time point.

In order to accomplish this analysis, the initial portion of the association curve is fit to an exponential functional form and then the exponential function is differentiated and the derivative function is evaluated at $t = t_0$, where t is time, and t_0 is the time at which solution is introduced to the microring. The equation utilized is a modified form of the integrated rate equation for a 1:1 Langmuir binding system and is given by:

$$S(t) = A\left(1 - e^{-B(t-t_0)}\right)$$

where $S(t)$ is the relative shift as a function of time, and A and B are fitting parameters. The variables A, B, and t_0 were fit to each binding curve independently and all parameters were allowed to vary. Curve fitting was done using the nonlinear curve fit routine in OriginPro 8. To determine initial slopes, the exponential equation can be differentiated to give the expression:

$$\frac{dS}{dt} = ABe^{-B(t-t_o)}$$

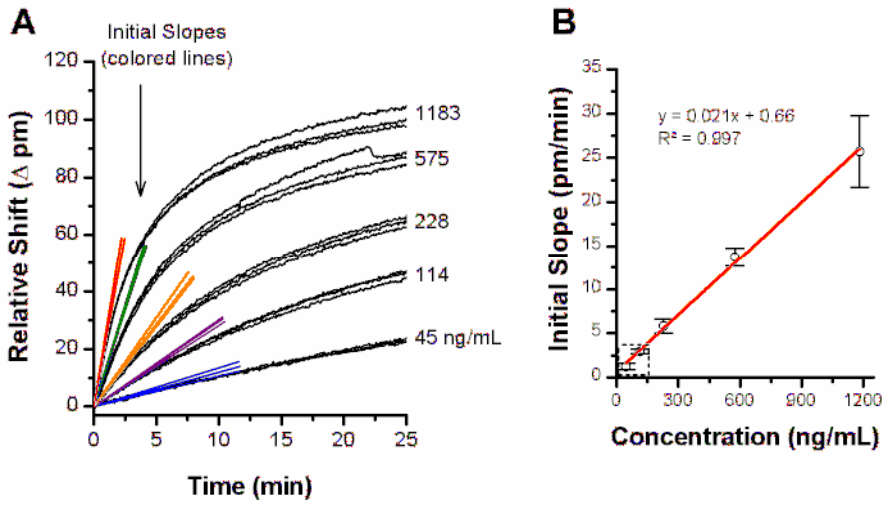

Figure 3.7 Real-time, label-free detection of CEA using microring resonators. (A) Overlay of three time-resolved association curves for the same ring at each concentration of CEA. The colored traces are tangent lines to the association curve at $t = 0$ and are used to determine the initial slope of sensor response. (B) Concentration-response calibration plot of the initial slope of sensor response versus CEA concentration upon introduction of antigen standard solutions. The dashed box in the corner of the graph represents the range shown in Figure 3.9C for measurement of CEA concentrations of unknown samples.

which evaluated at $t = t_0$ simplifies to:

$$\frac{dS}{dt} = AB$$

Figure 3.8A shows the regions of each curve from Figure 3.7 used for fitting, and Figure 3.8B shows the best fits overlaid on each curve. The colored lines in Figure 3.7A represent fitted tangent lines that give the initial slope for each association curve at each concentration. The initial slope values determined from the data in Figure 3.7A are plotted as a function of concentration in Figure 3.7B (error bars 95% confidence interval (C.I.), number of measurements (n) = 3). Table 3.1 gives the fitting parameters (*A*, *B*, t_0, *AB*, and χ^2 ,the chi-squared distribution) for each curve fitting in Figure 3.8B.

Notably, the resulting slope-based calibration plot is linear (coefficient of determination (R^2) for the linear fit is 0.997), which enables simple sensor calibration and extended linear dynamic range, particularly at higher antigen concentrations. While data from only a single microring is shown for clarity, the response of multiple sensors were simultaneously recorded and found to also yield linear calibration plots with extended dynamic ranges. While each microring behaved in a similar fashion, it is apparent that small differences in antibody loading require each microring sensor to be independently calibrated. Methods of *a priori* sensor normalization have the potential to enable independent calibration and fully automated applications in the future.

To demonstrate the ability of microring sensors to quantify samples containing lower concentrations of CEA, a second calibration curve was constructed based on the initial slope approach using standard concentrations from 0 to 121 ng/mL—encompassing the clinically-relevant range of 5–100 ng/mL. Figure 3.9A shows the overlaid time-response curves used to generate the initial slopes for the standard concentrations. Each concentration was run in triplicate with best-fit lines shown in color. Given that the rate of association is very slow at these concentrations, we directly fit the data from to a linear function, bypassing the exponential fit and derivative determination required at higher concentrations.

The initial slope-based concentration response curve is shown in Figure 3.9C (error bars 95% C.I., n = 3). Again a linear calibration plot is observed ($R^2 = 0.997$). The real-time association data shown in Figures 3.7B and 3.9C were obtained with the same microring, but on

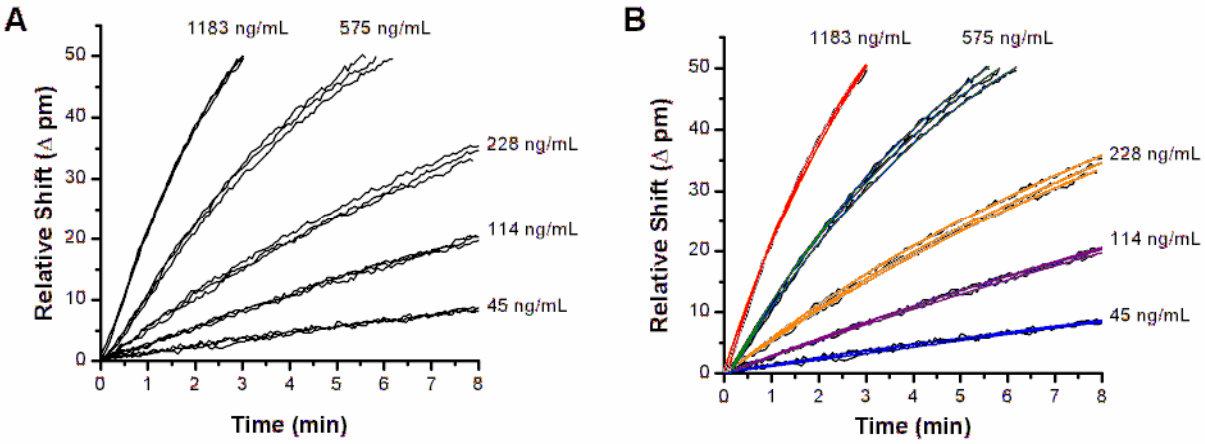

Figure 3.8 (A) Selected initial regions for each binding curve from Figure 6A (B) Best fits of exponential function overlaid on each curve

Table 3.1 Fitting parameters for exponential fits shown in Figure 3.8.

Concentration (ng/mL)	A (pm)	B (min^{-1})	t_0 (min)	AB (pm/min)	χ^2
45	600.5	0.00176	-0.0692	1.057	0.0669
45	41.5	0.02858	-0.1982	1.187	0.0683
45	19.3	0.06947	-0.0745	1.343	0.0494
114	87.2	0.03224	0.0340	2.813	0.0607
114	86.7	0.03405	0.0336	2.951	0.0623
114	67.3	0.04482	0.0191	3.018	0.0643
228	76.0	0.07345	0.0188	5.580	0.1373
228	78.9	0.07224	-0.0042	5.699	0.0758
228	73.0	0.08461	0.0333	6.180	0.0654
575	77.4	0.17261	0.1328	13.355	0.2019
575	80.0	0.16998	0.0739	13.605	0.3361
575	81.9	0.17305	0.1175	14.179	0.1465
1183	92.7	0.25708	-0.0189	23.831	0.4325
1183	82.6	0.32173	0.0604	26.591	0.2257
1183	80.3	0.33292	0.0466	26.722	0.0545

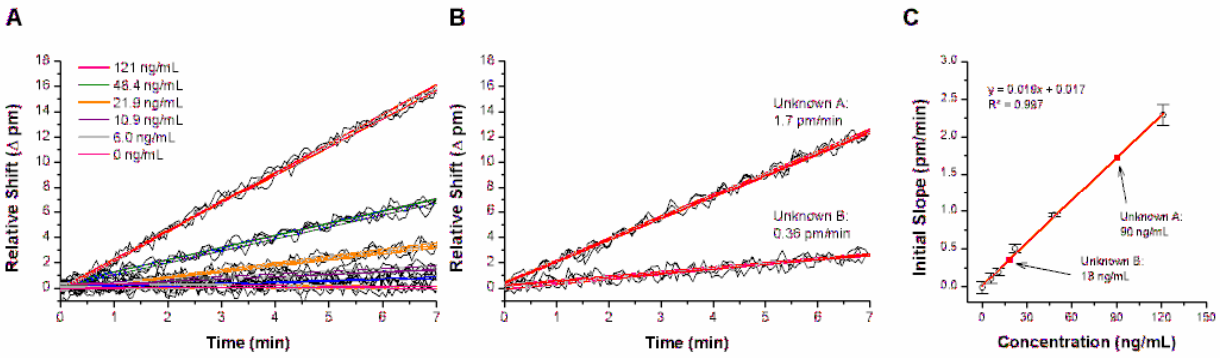

Figure 3.9 Real-time, label-free detection of low concentrations of CEA using microring resonator sensors. (A) Overlay of three time-resolved association curves at each concentration of CEA, as listed on the plot. The colored lines are linear fits to association data used to determine the initial slope of sensor response. (B) Overlay of three time-resolved association curves for unknown A and unknown B with linear fits shown in red. (C) Concentration-response calibration plot for CEA as determined by the initial slope method based on the initial slopes determined from (A) and (B).

Table 3.2 Fitting parameters for linear fits shown in Figure 3.9.

Concentration (ng/mL)	Slope (pm/min)	Slope Error (pm/min)	Intercept (pm)	Intercept Error (pm)	R^2
0	-0.03562	0.01713	0.372	0.0697	0.03654
0	-0.01616	0.01617	0.085	0.06581	0.00869
0	0.02516	0.01646	-0.044	0.067	0.02009
6.0	0.07964	0.02004	0.177	0.08169	0.12163
6.0	0.12607	0.01924	0.018	0.07875	0.27352
6.0	0.12799	0.01998	-0.122	0.08128	0.26475
10.9	0.17368	0.01679	0.192	0.06819	0.48414
10.9	0.20138	0.01470	0.094	0.06076	0.61812
10.9	0.20924	0.01817	0.291	0.07412	0.53777
21.9	0.48175	0.01490	-0.197	0.06094	0.90169
21.9	0.50773	0.01791	-0.178	0.07283	0.87575
21.9	0.52727	0.01267	-0.118	0.05159	0.93827
48.4	0.94338	0.01830	0.096	0.07452	0.95888
48.4	0.95315	0.01542	0.314	0.06305	0.97104
48.4	0.96077	0.01392	0.336	0.05685	0.97662
121	2.23048	0.01504	0.046	0.06142	0.99484
121	2.30533	0.01525	-0.044	0.06223	0.99503
121	2.33983	0.02154	-0.240	0.0879	0.99043
Unknown A	1.70922	0.01657	0.334	0.07494	0.9882
Unknown A	1.72481	0.01438	0.358	0.06667	0.99104
Unknown A	1.7344	0.01372	0.468	0.06291	0.99206
Unknown B	0.34016	0.01730	0.160	0.07278	0.76611
Unknown B	0.35153	0.01313	0.264	0.05705	0.85552
Unknown B	0.39018	0.01586	-0.085	0.06907	0.83216

different days. While the slopes of the calibration traces are similar, they are not identical, and there is a noticeable difference in the y-intercept—largely due to the variation in the dynamic range of each calibration plot. This observation reinforces the notion that at this stage each sensor must be independently calibrated on the same day and, ideally, calibrated directly in series with unknown samples. As with any calibration curve, the greatest accuracy for evaluating an unknown will be obtained by using calibration concentrations within a relevant range for the unknowns.

3.3.3 Measurement of unknown CEA concentrations

While the generation of calibration curves from standards is important, the obvious objective is the quantitation of unknown samples of CEA. Two blinded unknown samples A and B were measured to determine the concentrations of CEA using both a microring sensor and a commercial CEA ELISA kit. Both unknown solutions were flowed over the microring in triplicate, interspersed between the three concentration series shown in Figure 3.9A. The data for the unknown binding curves and subsequent linear fits are shown in Figure 3.9B. The initial slopes were determined for the lower concentration CEA standards and for the unknowns and the fitting parameters for each of these measurements is shown in Table 3.2. The unknown samples had slopes of 1.7 pm/min and 0.36 pm/min for unknowns A and B, respectively. Figure 3.9C shows the mapping of these initial slope values onto the calibration curve and quantitation of the unknowns as 90 ± 2 and 18 ± 1 ng/mL, respectively (uncertainties are based on the 95% C.I. for a calibration curve with n = 18, with three replicate unknown evaluations). The concentration values were then compared with those obtained using a commercial ELISA kit. The same unknown solutions (A and B) were assayed in a 96-well plate along with the provided standards according to manufacturer instructions. Concentration determination via ELISA gave concentrations of 112 ± 11 and 17 ± 9 ng/mL for unknowns A and B, respectively (uncertainties are based on the 95% C.I. for the ELISA calibration curve with n = 18, with three replicate unknown evaluations). The calibration curve for the ELISA is shown in Figure 3.10.

Following quantitation of CEA via both microring sensors and the commercial ELISA kit, the concentrations of the prepared blinded unknowns A and B were revealed to be 91 and 17 ng/mL, respectively. Interestingly, both microrings and ELISA were able to determine the lower

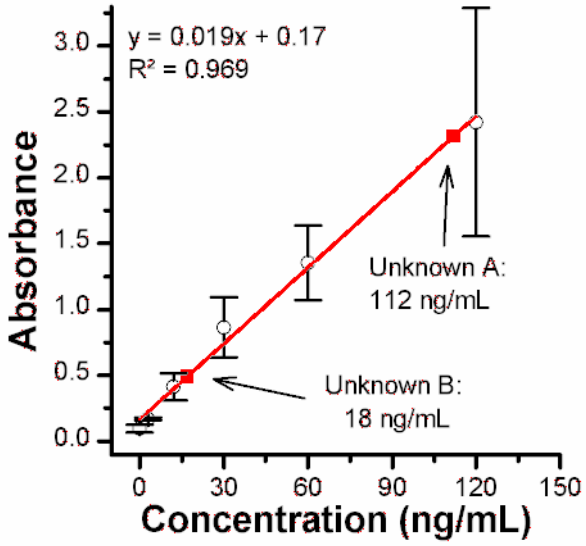

Figure 3.10 Overlay of the unknown solutions on the concentration-response calibration plot for CEA in BSA-PBS using a commercial ELISA kit; the concentration of the unknown solutions were determined to be 112 ± 11 and 17 ± 9 ng/mL.

concentration with a high degree of accuracy. Unknown A, which is higher in concentration, was also correctly determined via the microring resonators. However, the "correct" value falls outside the 95% confidence interval for the ELISA assay. Notably, the 95% confidence intervals are considerably larger for the ELISA assay. At higher concentrations this is likely due to the larger absorbance values that test the linearity of the spectrometer. The error in high concentration determination might be reduced by shortening the time of the development step, but this would compromise the ability to accurately quantitate at lower concentrations. This trade-off in the quantitative ability of ELISA across a one order of magnitude dynamic range is clearly less of a concern using the label-free microring resonator sensor.

To determine a detection limit for the microring resonator sensor, a minimum resolvable change in initial slope must be established in comparison to the normal baseline "slope noise." To achieve this, the standard deviation of the linear slope (slope noise, σ) of representative 7 min baseline sections (the same period of time over which the initial slope was fit for determination of low antigen concentrations) was measured to be 0.02 pm/min. Extrapolating to the 3σ threshold, the limit of detection for CEA in BSA-PBS was determined to be ~2 ng/mL. Notably, this value is below the basal levels (3-5 ng/mL) of CEA present in the serum of "healthy" adults. The microring detection limit is also comparable to the stated manufacturer value for the commercial ELISA kit of 1 ng/mL. Notably, the initial slope-based concentration determination can be accomplished in less than 30 minutes using microring resonators—a total of four 7 min runs (three standards and one unknown sample)—which is significantly faster than the 3+ hour ELISA procedure. Given the favorable precision, similar limit of detection, and assay speed in comparison to an ELISA assay, the potential of microring resonators for rigorous quantitation of unknown protein concentrations is high.

By way of comparison, multiple microring sensors on a given chip are observed to vary in the slope of the calibration curve slope by about 10-20%. However, the precision of each calibration curve remains fairly consistent, allowing unknowns to be evaluated among multiple sensors with a standard deviation of around 1-2 ng/mL, on the same magnitude as the observed uncertainty for a single calibration curve.

3.3.4 Cancer Biomarker Detection in Serum

We have also evaluated the ability of microring sensors to detect CEA in 100% fetal bovine serum. By adding human CEA to FBS, the detection platform was challenged with a complex sample matrix similar to that encountered when analyzing human serum or other biological fluids. CEA standards were created in FBS at concentrations of 0, 19, 49, 98, and 199 ng/mL, and the analysis was performed on a sensor chip functionalized with an anti-CEA antibody. As with CEA detection in buffer, the concentration of CEA in FBS was directly related to the initial slope following addition of the samples. However, because FBS contains a high concentration of proteins that nonspecifically adsorb to the sensor surface, addition of FBS resulted in a drifting baseline signal that could only be partially corrected using the on-chip control rings, as can be seen from an example trace in Figure 3.11A. Therefore, to accurately determine the sensor response to CEA, the slope of the baseline was measured 5 min before injection of the CEA sample and the slope of the drifting baseline was subtracted from the measured slope after the injection time. Table 3.3 gives the fitting parameters for the linear fits used in the serum analysis to create the calibration plot shown in Figure 3.11B. To test the validity of the calibration curve, a blinded unknown was evaluated and determined to have a concentration of 61 ± 23 ng/mL by comparison with the standard calibration curve shown in Figure 3.11B (uncertainties for unknowns are based on the 95% C.I. for a calibration curve with n = 15, unknown run one time). The microring resonator results were again correlated with those of a commercially-available ELISA, which gave a value of 67 ± 9 ng/mL. The calibration plot for this ELISA is shown in Figure 3.12. Both values were in good agreement with the prepared unknown concentration of 70 ng/mL, as revealed by analyses using microring and ELISA methods.

By comparing the slopes of the calibration curves for microring resonator detection of CEA in both buffer and serum, it is apparent that sensitivity is greatly reduced in serum. Whereas detection in buffer gives a slope of 0.019 (pm/min)/(ng/mL), see Figure 3.9C, detection in serum shows a ~6 fold decrease to 0.0036 (pm/min)/(ng/mL), as shown in Figure 3.11. This is not unexpected, however, since the specific binding of CEA is in competition for available antibody recognition sites with nonspecific interactions from serum proteins, some of which are present at 10^8-fold higher concentration.[42] In addition, the baseline “slope noise” in serum (determined in

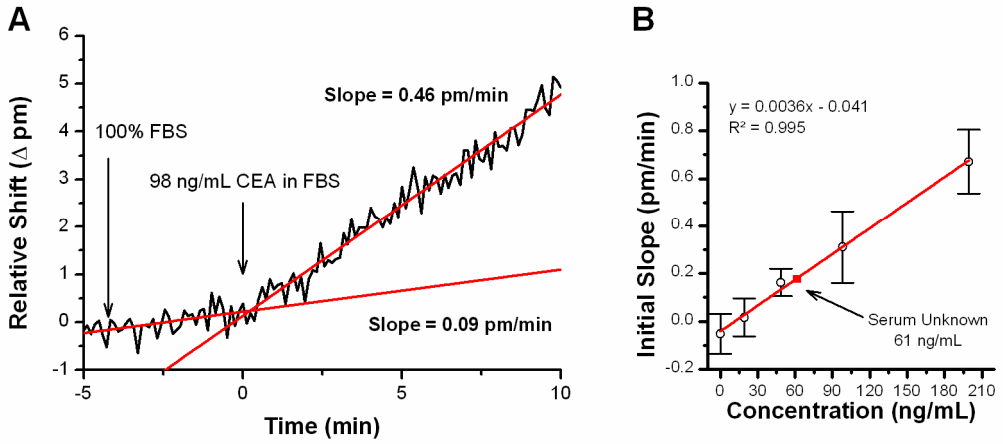

Figure 3.11 (A) Example sensor response following addition of CEA in 100% FBS. Initial slope is determined by using a linear fit of the baseline to subtract the drifting baseline from the change in signal caused by addition of CEA in FBS. (B) Overlay of the unknown solution on the concentration-response calibration plot for CEA in 100% FBS. The concentration was determined to be 61 ± 23 ng/mL, which is in good agreement with a commercial ELISA assay.

Table 3.3 Fitting parameters used to create the trace shown in Figure 6B in the manuscript.

Concentration (ng/mL)	Fit Region	Slope (pm/min)	Error (pm/min)	Intercept (pm)	Intercept Error (pm)	R^2
0	baseline	0.121	0.029	0.311	0.085	0.310
	response	0.072	0.013	0.430	0.076	0.302
0	baseline	0.142	0.030	0.357	0.088	0.359
	response	0.122	0.012	0.390	0.076	0.566
0	baseline	0.158	0.026	0.403	0.077	0.476
	response	0.070	0.012	0.459	0.072	0.328
19	baseline	0.263	0.027	0.672	0.079	0.707
	response	0.249	0.012	0.733	0.073	0.853
19	baseline	0.187	0.024	-1.668	0.069	0.611
	response	0.201	0.010	-1.827	0.058	0.857
19	baseline	0.146	0.026	0.374	0.075	0.451
	response	0.196	0.011	0.351	0.065	0.819
49	baseline	0.158	0.028	0.505	0.081	0.444
	response	0.335	0.013	0.433	0.076	0.907
49	baseline	0.133	0.019	0.342	0.057	0.538
	response	0.308	0.010	0.532	0.060	0.928
49	baseline	0.106	0.026	0.271	0.079	0.280
	response	0.242	0.012	0.403	0.071	0.855
98	baseline	0.298	0.035	0.627	0.106	0.638
	response	0.601	0.014	0.913	0.086	0.962
98	baseline	0.093	0.023	0.233	0.066	0.293
	response	0.469	0.011	0.099	0.070	0.958
98	baseline	0.105	0.025	0.268	0.074	0.302
	response	0.361	0.010	0.254	0.057	0.951
199	baseline	0.249	0.039	0.716	0.117	0.505
	response	0.940	0.013	0.409	0.079	0.986
199	baseline	0.156	0.030	0.398	0.089	0.398
	response	0.868	0.011	0.640	0.068	0.988
199	baseline	0.105	0.025	0.268	0.074	0.302
	response	0.361	0.010	0.254	0.057	0.951
Unknown	baseline	0.180	0.025	0.463	0.075	0.555
	response	0.360	0.013	0.292	0.076	0.918

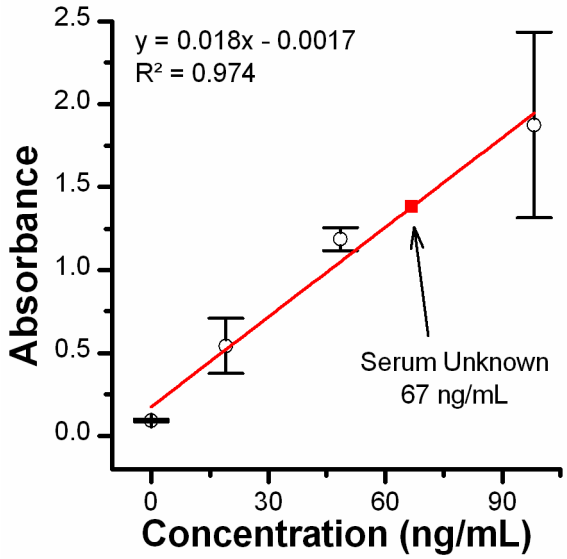

Figure 3.12 Overlay of the unknown solutions on the concentration-response calibration plot for CEA in 100% FBS using the same commercial ELISA kit; the concentration was determined to be 67 ± 9 ng/mL.

the same manner as for detection in buffer) was found to be 0.03 pm/min, which is slightly larger than the 0.02 pm/min for detection in buffer. This increased slope noise is largely the result of nonspecific serum adsorption that causes the drifting baseline, which, although largely linear, does have a slowly decreasing slope over time. While this nonlinear behavior limits the precision of slope determination it does not preclude quantitation of CEA levels in an unknown sample. Taken together, the decreased sensitivity to CEA in serum (as compared to buffer) and the slightly increased baseline noise result in a limit of detection of 25 ng/mL. Although still within the range monitored clinically (5–100 ng/mL), future work to lower the detection limit and improve measurement precision in serum will be necessary. One area of particular focus is minimizing nonspecific serum protein adsorption through improved surface treatment.

3.4 Conclusion

The work of this chapter establishes that arrays of silicon photonic optical microring resonators are a robust emerging tool for bioanalysis of clinically relevant samples. We show the ability to directly visualize the chemical and biochemical functionalization of the sensor surface to ensure consistent loading of antibody capture agents. We then demonstrate the applicability of the microring resonator platform for the sensitive and robust detection of a relevant marker of disease at clinically relevant levels in both buffer and fetal bovine serum. By utilizing a quantitation scheme based upon measuring the time-resolved initial slope of the sensor response, the concentration of unknown CEA solutions in buffer are determined in a label-free format with comparable sensitivity and improved precision over commercial ELISA assays. The established limits of detection are among the lowest ever reported for microring resonators applied to protein detection at the time of publication of this data. We also demonstrate the first-ever operation of such a device in undiluted serum. While still at an early stage of development, the inherent multiplexing capability of this optical semiconductor-based analysis technology, coupled with the detection limits and precision demonstrated herein, establishes silicon-on-insulator microring resonators as a promising platform for highly multiplexed, label-free biomolecular analysis.

3.5 References

(1) Royer, C. A.; Scarlata, S. F. In *Methods Enzymol.*; Ludwig, B., Michael, L. J., Eds.; Academic Press: Burlington, MA, 2008; Vol. Volume 450, pp 79-106.

(2) Seydack, M. *Biosens. Bioelectron.* **2005**, *20*, 2454-2469.

(3) Hempen, C.; Karst, U. *Anal. Bioanal. Chem.* **2006**, *384*, 572-583.

(4) Kodadek, T. *Chem. Biol.* **2001**, *8*, 105-115.

(5) Sun, Y. S.; Landry, J. P.; Fei, Y. Y.; Zhu, X. D.; Luo, J. T.; Wang, X. B.; Lam, K. S. *Langmuir* **2008**, *24*, 13399–13405.

(6) Qavi, A. J.; Washburn, A. L.; Byeon, J.-Y.; Bailey, R. C. *Anal. Bioanal. Chem.* **2009**, *394*, 121-135.

(7) Fan, X.; White, I. M.; Shopoua, S. I.; Zhu, H.; Suter, J. D.; Sun, Y. *Anal. Chim. Acta* **2008**, *620*, 8-26.

(8) Homola, J. *Chem. Rev.* **2008**, *108*, 462-493.

(9) Cunningham, B. T.; Laing, L. *Exp. Rev. Prot.* **2006**, *3*, 271-281.

(10) Gauglitz, G.; Proll, G. In *Biosensing for the 21st Century*; Springer-Verlag Berlin: Berlin, 2008; Vol. 109, pp 395-432.

(11) Vollmer, F.; Arnold, S. *Nat. Methods* **2008**, *5*, 591-596.

(12) Jokerst, N.; Royal, M.; Palit, S.; Luan, L.; Dhar, S.; Tyler, T. *J. Biophotonics* **2009**, *2*, 212-226.

(13) Ren, H. C.; Vollmer, F.; Arnold, S.; Libchaber, A. *Opt. Express* **2007**, *15*, 17410-17423.

(14) Vollmer, F.; Braun, D.; Libchaber, A.; Khoshsima, M.; Teraoka, I.; Arnold, S. *Appl. Phys. Lett.* **2002**, *80*, 4057-4059.

(15) Vollmer, F.; Arnold, S.; Braun, D.; Teraoka, I.; Libchaber, A. *Biophys. J.* **2003**, *85*, 1974-1979.

(16) Armani, A. M.; Kulkarni, R. P.; Fraser, S. E.; Flagan, R. C.; Vahala, K. J. *Science* **2007**, *317*, 783-787.

(17) Suter, J. D.; White, I. M.; Zhu, H.; Shi, H.; Caldwell, C. W.; Fan, X. *Biosens. Bioelectron.* **2008**, *23*, 1003-1009.

(18) White, I. M.; Oveys, H.; Fan, X.; Smith, T. L.; Zhang, J. *Appl. Phys. Lett.* **2006**, *89*, 191106.

(19) Zhu, H.; White, I. M.; Suter, J. D.; Dale, P. S.; Fan, X. *Opt. Express* **2007**, *15*, 9139-9146.

(20) Zhu, H.; White, I. M.; Suter, J. D.; Zourob, M.; Fan, X. *Analyst* **2008**, *133*, 356-360.

(21) Zhu, H. Y.; White, I. M.; Suter, J. D.; Fan, X. D. *Biosens. Bioelectron.* **2008**, *24*, 461-466.

(22) Boyd, R. W.; Heebner, J. E. *Appl. Opt.* **2001**, *40*, 5742-5747.

(23) Krioukov, E.; Klunder, D. J. W.; Driessen, A.; Greve, J.; Otto, C. *Opt. Lett.* **2002**, *27*, 512-514.

(24) Chao, C. Y.; Fung, W.; Guo, L. J. *IEEE J. Sel. Top. Quantum Electron.* **2006**, *12*, 134-142.

(25) Chao, C. Y.; Guo, L. J. *Appl. Phys. Lett.* **2003**, *83*, 1527-1529.

(26) Xu, D.-X.; Densmore, A.; Delâge, A.; Waldron, P.; McKinnon, R.; Janz, S.; Lapointe, J.; Lopinski, G.; Mischki, T.; Post, E.; Cheben, P.; Schmid, J. H. *Opt. Express* **2008**, *16*, 15137-15148.

(27) De Vos, K.; Girones, J.; Popelka, S.; Schacht, E.; Baets, R.; Bienstman, P. *Biosens. Bioelectron.* **2009**, *24*, 2528-2533.

(28) De Vos, K. M.; Bartolozzi, I.; Bienstman, P.; Baets, R.; Schacht, E. *Proc. SPIE* **2007**, *6447*, 64470K.

(29) Yalçin, A.; Popat, K. C.; Aldridge, J. C.; Desai, T. A.; Hryniewicz, J.; Chbouki, N.; Little, B. E.; King, O.; Van, V.; Chu, S.; Gill, D.; Anthes-Washburn, M.; Ünlü, M. S. *IEEE J. Sel. Top. Quantum Electron.* **2006**, *12*, 148-155.

(30) Ramachandran, A.; Wang, S.; Clarke, J.; Ja, S. J.; Goad, D.; Wald, L.; Flood, E. M.; Knobbe, E.; Hryniewicz, J. V.; Chu, S. T.; Gill, D.; Chen, W.; King, O.; Little, B. E. *Biosens. Bioelectron.* **2008**, *23*, 939-944.

(31) Wang, J. Y.; Tang, R. P.; Chiang, J. M. *Dis. Colon Rectum* **1994**, *37*, 272-277.

(32) Borras, G.; Molina, R.; Xercavins, J.; Ballesta, A.; Iglesias, J. *Gynecol. Oncol.* **1995**, *57*, 205-211.

(33) Sung, H.-J.; Cho, J.-Y. *BMB Reports* **2008**, *41*, 615-625.

(34) Sölétormos, G.; Nielsen, D.; Schiøler, V.; Mouridsen, H.; Dombernowsky, P. *Eur. J. Cancer* **2004**, *40*, 481-486.

(35) Schiemann, U.; Günther, S.; Gross, M.; Henke, G.; Müller-Koch, Y.; König, A.; Muders, M.; Folwaczny, C.; Mussack, T.; Holinski-Feder, E. *Cancer Detect. Prev.* **2005**, *29*, 356-360.

(36) Iqbal, M.; Gleeson, M. A.; Spaugh, B.; Tybor, F.; Gunn, W. G.; Hochberg, M.; Baehr-Jones, T.; Bailey, R. C.; Gunn, L. C. *IEEE J. Sel. Top. Quantum Electron.* **2010**, *16*, 654-661.

(37) Dillon, M. C.; Opris, D. C.; Kopanczyk, R.; Lickliter, J.; Cornwell, H. N.; Bridges, E. G.; Nazar, A. M.; Bridges, K. G. *Biomarker Insights* **2010**, *5*, 57-61.

(38) Eddowes, M. J. *Biosensors* **1987**, *3*, 1-15.

(39) Tunnemann, R.; Mehlmann, M.; Sussmuth, R. D.; Buhler, B.; Pelzer, S.; Wohlleben, W.; Fiedler, H.-P.; Wiesmuller, K.-H.; Gauglitz, G.; Jung, G. *Anal. Chem.* **2001**, *73*, 4313-4318.

(40) Adamczyk, M.; Mattingly, P. G.; Shreder, K.; Yu, Z. *Bioconj. Chem.* **1999**, *10*, 1032-1037.

(41) Cheng, T.-J.; Lin, T.-M.; Chang, H.-C. *Anal. Chim. Acta* **2002**, *462*, 261-273.

(42) Anderson, N. L.; Anderson, N. G. *Mol. Cell. Proteomics* **2002**, *1*, 845-867.

Chapter 4

Quantitative, Label-Free Detection of Five Protein Biomarkers Using Multiplexed Arrays of Silicon Photonic Microring Resonators

Notes and Acknowledgements

This chapter has been reproduced from the original paper "Quantitative, Label-Free Detection of Five Protein Biomarkers Using Multiplexed Arrays of Silicon Photonic Microring Resonators" (Washburn, A. L.; Luchansky, M. S.; Bowman, A. L.; Bailey, R. C. Anal. Chem. **2010**, *82*, 69–72). It has been reproduced here with permission from the American Chemical Society © 2010.

Adrienne Bowman and Matthew Luchansky are acknowledged for their assistance in the initial experiments that led to final results presented here.

This work was funded by the NIH Director's New Innovator Award Program, part of the NIH Roadmap for Medical Research, through grant number 1-DP2-OD002190-01 and the Camille and Henry Dreyfus Foundation. ALW was supported via a National Science Foundation Graduate Research Fellowship. MSL was supported by a National Science Foundation Graduate Research Fellowship and a Robert C. and Carolyn J. Springborn Fellowship from the Department of Chemistry at the University of Illinois at Urbana-Champaign. We acknowledge Abraham Qavi for his assistance in creating the unknown solutions.

This article can be accessed online at: http://dx.doi.org/10.1021/ac902451b

4.1 Introduction

Label-free bioanalytical technologies have recently garnered increased interest for their ability to generate highly sensitive and quantitative measurements without the cost, complexity, or labeling heterogeneity introduced by techniques requiring fluorescent or enzymatic tags.[1, 2] In particular, optical biosensors based on refractive index (RI) changes associated with analyte binding hold particular promise for conducting multiparameter biological analyses without labels.[3-5] Within the realm of label-free RI-based optical biosensors, microcavity resonators have demonstrated the ability to sensitively detect a diverse array of biological analytes including proteins,[6-9] nucleic acids,[10, 11] cells,[12] and viruses.[13, 14] Arrays of silicon photonic microring resonators, which can be routinely fabricated using well-established semiconductor processing techniques, have been previously demonstrated for biomolecular detection.[8, 15-18] However, despite their promise for highly multiplexed detection, previous reports have yet to demonstrate the ability to simultaneously detect and rigorously quantitate multiple clinically relevant analytes from a single sample volume using a single sensor array.

Chapter 3 demonstrated the use of silicon photonic microring resonators for quantitation of the cancer biomarker carcinoembryonic antigen (CEA) with a clinically relevant limit of detection comparable to a CEA enzyme-linked immunosorbent assay (ELISA). Extending beyond single parameter quantitation, this chapter demonstrates multiplexed detection using arrays of silicon-on-insulator microring resonators. Multiparameter bioanalytical technologies that provide multiple clinically relevant measurements from a single sample are of great value to applications ranging from individualized diagnosis to fundamental studies in systems biology.[19, 20] Though a previous report has indicated the ability to perform multiplex measurements on nucleic acids using a microsphere-based sensing strategy,[11] we significantly extend the multiplexing capabilities of microcavity resonators by demonstrating the ability to simultaneously perform 20 unique label-free immunoassays in parallel. Using these twenty independent sensors, we report an assay, run in quadruplicate, for five clinically relevant protein biomarkers [CEA, prostate specific antigen (PSA), alpha-fetoprotein (AFP), interleukin-8 (IL-8), and tumor necrosis factor-alpha (TNF-α)] on a single silicon photonic microring resonator array. Cross-reactivity profiles and individual calibration curves are generated for each antigen, and the

platform is validated by accurate quantitation of three separate unknown protein cocktails in a blind analysis.

4.2 Materials and Methods

4.2.1 Materials

Succinimidyl 4-formylbenzoate (S-4FB), and the silane 3-N-((6-(N'-Isopropylidene-hydrazino))nicotinamide)propyltriethyoxysilane (HyNic Silane), were purchased from SoluLink (San Diego, CA). Aniline was obtained from Acros Organics (Geel, Belgium). Monoclonal mouse anti-human CEA (Cat# M37401M), human CEA (Cat# A32030H), monoclonal mouse anti-human PSA (Cat #M86506M), human PSA (Cat# H6M07-323), monoclonal mouse anti-human AFP (Cat #H45610M), and human AFP (Cat# A81510H) were purchased from Meridian Life Science, Inc. (Saco, ME). Recombinant human IL-8 (Cat# 208-IL/CF) and monoclonal mouse anti-human IL-8 (Cat# MAB208) were obtained from R&D Systems (Minneapolis, MN). Monoclonal anti-human TNF-α (Cat# 16-7348), recombinant human TNF-α (Cat # 34-8329), and mouse IgG isotype control (Cat # 16-4714-85) were obtained from eBioscience (San Diego, CA). Zeba spin filter columns were purchased from Pierce (Rockford, IL). Silicone elastomer kit (RTV 615 2-Part Addition Cure Clear Silicone) was obtained from Momentive Performance Materials (Albany, NY). PBS was reconstituted from Dulbecco's phosphate buffered saline packets purchased from Sigma-Aldrich (St. Louis, MO). All other chemicals were obtained from Sigma-Aldrich and used as received.

All buffers were made with purified water (ELGA PURELAB filtration system; Lane End, UK), and the pH was adjusted as necessary with 1 M HCl or 1 M NaOH. Acetate buffer consisted of 50 mM sodium acetate and 150 mM sodium chloride adjusted to pH 6.0. Glycine buffer was 10 mM glycine and 160 mM NaCl adjusted to pH 2.2. BSA-PBS buffer was made by dissolving solid bovine serum albumin (BSA) in PBS (pH 7.4) to a final concentration of 0.1 mg/mL. For blocking, 2% BSA (w/v) in PBS was used. All solutions were degassed under vacuum before being flowed across the sensor surface.

4.2.2 Microrings and Instrumentation

Microring resonator array substrates and the instrumentation for analyzing the microring resonance frequencies were acquired from Genalyte, Inc. (San Diego, CA) and have been previously described.[6, 21] Briefly, 6 × 6 mm substrates hold sixty-four 30-µm diameter microrings with adjacent linear access waveguides that have input and output diffractive grating couplers at each end to independently measure the optical cavity spectrum of each microring. The entire wafer was spin-coated with a commercially-available perfluoro (alkenyl vinyl ether) copolymer (Asahi Glass Company) and annular openings were created over the active sensing rings via photolithography and reactive ion etching. Up to thirty-two microring sensors can be monitored simultaneously, with eight of the sensors not exposed to solution (covered by the fluoropolymer cladding) and used exclusively to compensate for thermal drift. The instrumentation uses a tunable, external cavity diode laser (center frequency 1560 nm) to rapidly scan the chip surface and couple light into the waveguides via grating couplers. Resonance wavelengths are determined as the wavelength at which the out-coupled light that has passed by the microring is at a minimum.

4.2.3 Microfludic Setup

For all steps except antibody functionalization, sensor chips were loaded into a custom cell with microfluidic flow channels defined by a Mylar gasket described in Chapter 3. Flow rates were maintained at 30 µL/min throughout the sensing experiments. For antibody functionalization, a 6-channel PDMS device was molded over a SU-8 template fabricated on a silicon wafer using standard photolithographic techniques. The PDMS device was created by mixing the base and curing agent in a 10:1 ratio and allowing the mixture to completely cure at 80 °C. Figure 4.1 contains an illustration of how both the microfluidic device and the one-channel Mylar gasket overlay the microring sensor array.

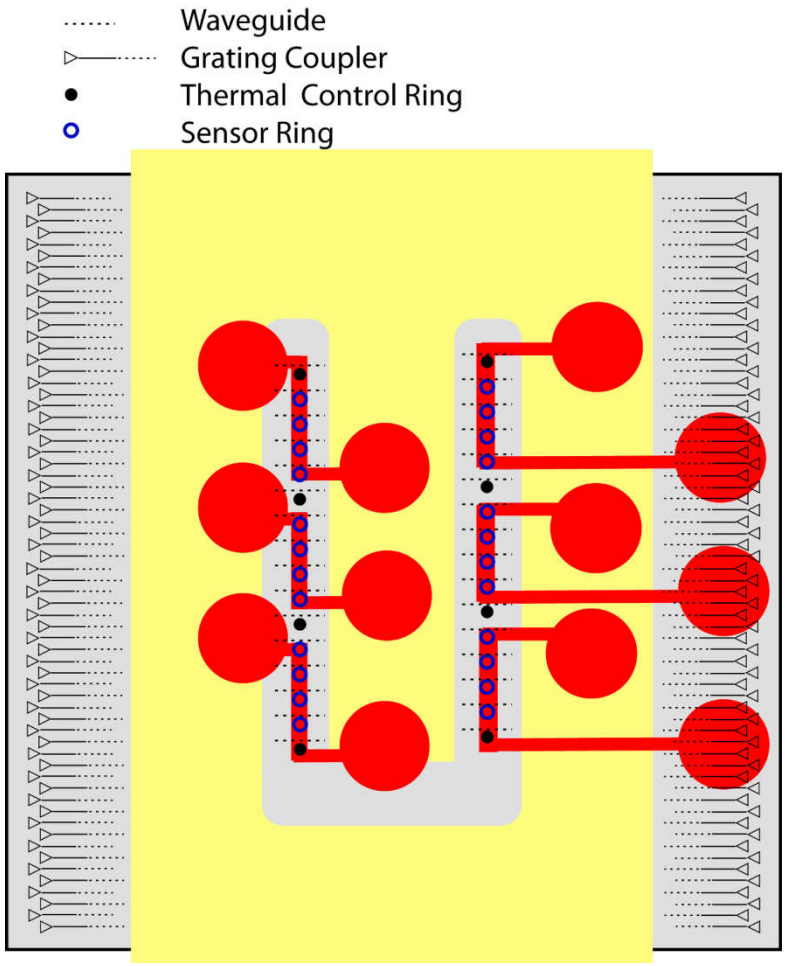

Figure 4.1 Schematic showing the layout of microrings and grating couplers on the microchip surface. Projections of the 6 PDMS microchannels used to differentially functionalize microrings with antibodies are shown in red. The PDMS microfluidic device was used exclusively for the directed antibody functionalization step. The placement of the single-channel Mylar gasket for subsequent detection experiments is shown in yellow.

4.2.4 Microring Surface Functionalization

Before functionalizing the microring surfaces, sensor chips are first cleaned by a 30-second immersion in piranha solution[22] (3:1 H_2SO_4:30% H_2O_2) followed by copious rinsing with water and drying with nitrogen gas. To add a HyNic moiety to the surface, the sensor chip is exposed to a solution of 0.5 mg/mL HyNic Silane in 98% EtOH and 2% DMF for 10 minutes and then rinsed with 100% EtOH. Covalent attachment of antibodies is achieved by reacting the antibody (1 mg/mL) with a 5-fold molar excess of S-4FB (dissolved first in DMF and diluted in PBS to less than 5% DMF) for 2 h at room temperature. Excess S-4FB was removed by spin filtration with Zeba spin filter columns, which also allowed buffer exchange into acetate buffer. The antibodies are then covalently attached in a spatially-controlled fashion via microfluidic channels. Each 4FB-modified antibody was flowed through a different channel to functionalize five sets of four rings, each with a different antibody: anti-PSA, anti-AFP, anti-CEA, anti-IL-8, anti-TNF-α. The sixth channel was functionalized with a mouse IgG isotype control antibody to serve as an on-chip control for non-specific adsorption and bulk refractive index changes.

Aniline (100 mM) is added to each antibody solution to catalyze hydrazone bond formation[23] and enable the reaction to proceed in 20 minutes. A glycine buffer rinse is then used to remove any noncovalently bound antibody. A final blocking step is accomplished by overnight soaking in a 2% solution (w/v) of BSA in PBS.

4.2.5 Microring Calibration and Unknown Analysis

Antigen calibration standards were prepared by diluting stock solutions of the antigens (0.1 mg/mL or greater) in BSA-PBS to concentrations below 1 ug/mL. Unknowns for the blind analysis were prepared in a similar manner. The concentrations of antigens in each of the mixtures are given in Table 4.1. Air bubbles present while solution #8 was being analyzed resulted in several outliers, so the data from that run was discarded; however, because each of the concentrations was assayed in triplicate, quantitative analysis was still achieved. To generate an array of variable, but non-repeating concentrations, we consulted a website containing 5×5 Sudoku puzzles (http://www.sudoku-download.net) and assigned a different antigen concentration to each numerical value.

Table 4.1 Concentration of antigen in ng/mL according to calibration solution number

	1	**2**	**3**	**4**	**5**	**6**	**7**	**8**	**9**	**10**	**11**	**12**	**13**	**14**	**15**
PSA	150	20	10	50	100	50	150	20	10	100	100	20	10	50	150
IL-8	10	150	100	20	50	10	100	50	150	20	20	150	50	10	100
AFP	100	10	50	150	20	20	50	150	100	10	150	10	100	20	50
CEA	20	50	150	100	10	100	20	10	50	150	50	100	20	150	10
TNF-α	50	100	20	10	150	150	10	100	20	50	10	50	150	100	20

4.3 Results and Discussion

4.3.1 Cross Reactivity Testing

Following microring sensor functionalization, the specificity of the sensors for each antigen was tested to ensure that antibody cross-reactivity was minimal. The six-channel PDMS microfluidic was replaced by a single channel Mylar gasket (see Figure 4.1) to probe all of the sensors simultaneously. Five different solutions, each containing 1 μg/mL of a different purified protein cancer biomarker diluted in 0.1 mg/mL bovine serum albumin in PBS (BSA-PBS), were sequentially flowed for 10 minutes. As expected, the rings functionalized with the mouse IgG isotype control did not interact with any of the biomarkers; thus, these rings were utilized as controls to correct off baseline drift due to thermal fluctuations or bulk refractive index changes.

Figure 4.2 displays the control-subtracted response of the microrings (four microrings per antibody) plotted with the relative shift in the resonance wavelength (given as the change of wavelength in picometers, or Δ pm) as a function of time. Each set of microrings functionalized with a particular biomarker-specific antibody responded only to the appropriate antigen solution. The lack of response in the off-diagonal plots demonstrates that there was minimal sensor cross-reactivity for these antibody-antigen combinations and that the control rings effectively removed any sensor drift. The only minor exception occurs with the anti-CEA- and anti-AFP-functionalized sensors in response to IL-8. This response results from a bulk refractive index shift from a constituent in the IL-8 stock solution; upon dilution of IL-8 for experiments at more physiologically relevant concentrations, this bulk refractive shift becomes essentially negligible.

Differences in the antigen responses in Figure 4.2 (both within a set of sensors functionalized with the same antibody and between sets of sensors functionalized with different antibodies) are the result of several factors. First, variations in protein size result in different responses.[24] Binding of a large protein such as CEA (185 kDa) gives a proportionally larger change in refractive index near the surface than a smaller protein such as IL-8 (8 kDa). Second, any variation in antibody surface coverage will lead to differences in the number of available active binding sites on a given sensor. Finally, the fractional occupation of available binding sites on the sensor is strongly influenced by antibody-antigen binding affinity, which differs for each antibody used in this study. As seen in Figure 4.2, each set of rings functionalized within a particular flow channel demonstrates a consistent response upon antigen addition. The only

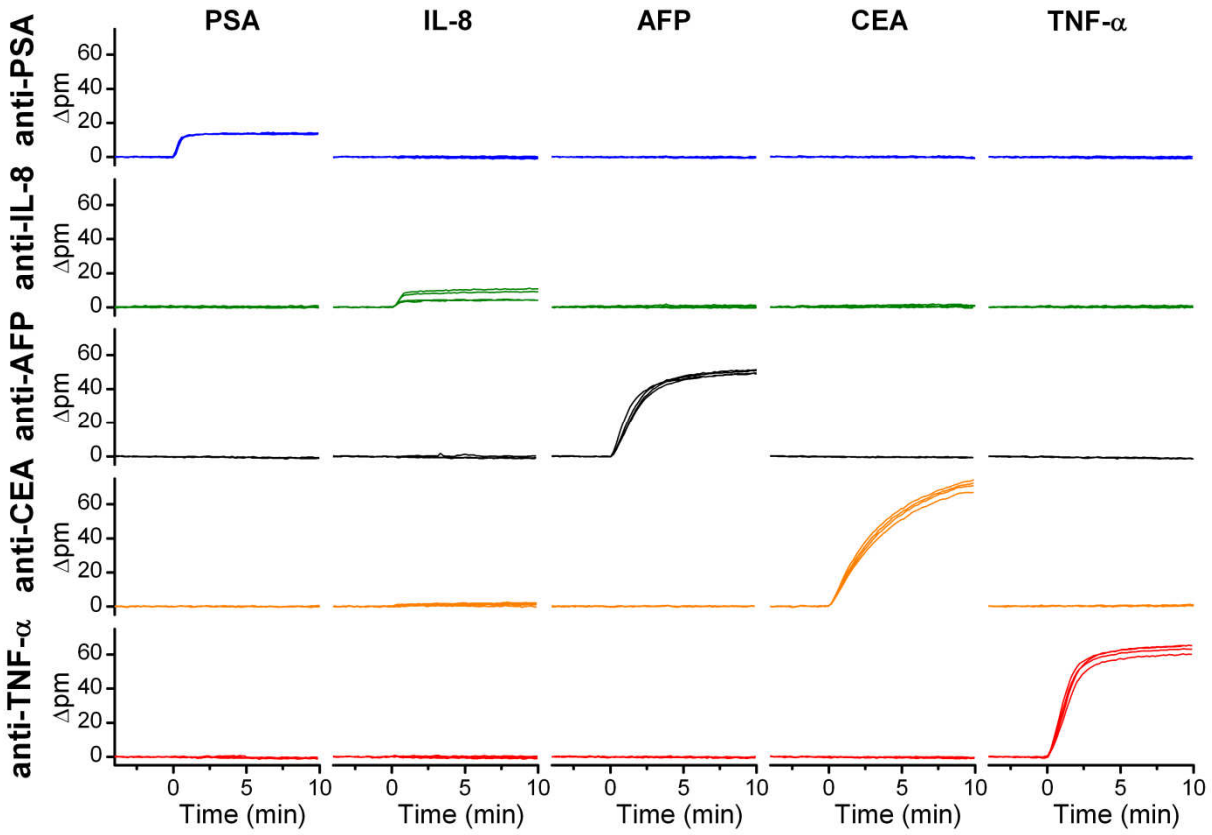

Figure 4.2 Cross-reactivity diagram. Each row represents the response of four rings functionalized with a particular antibody, as designated on the left hand axes (shift given as change in resonance peak wavelength in picometers); each column shows the sensor response upon addition of a 1µg/mL solution of a single antigen designated at the top of the respective column. The x- and y-scales are identical for all real-time association plots.

notable exception is for IL-8, where two of the rings have a noticeably smaller response than the other two rings.

4.3.2 Quantitative Multiplexed Sensing

To demonstrate quantitative multiplexed sensing, standard solutions were created that contain a mixture of each of the five antigens at different concentrations. We utilized the responses from these standards to independently calibrate each microring sensor using the previously described initial slope analysis method described in Chapter 3. Real-time response curves for CEA and TNF-α were fit to linear functions since these sensors were far from saturation at the particular concentrations and time intervals we used. Responses from PSA, IL-8, and AFP more closely approach binding equilibrium and therefore were more accurately fit to exponential functions as discussed in Chapter 3. As previously, initial slopes were determined by solving for the first derivative of the fitted exponential function at $t = 0$. From the initial slope data, calibration curves for each sensor ring were constructed.

Figure 4.3 displays overlays of the real-time response curves for all 20 sensor rings. Each column in Figure 4.3 represents a set of four microrings functionalized with a different antibody. Each color on the graph represents a different concentration of antigen between 0 and 150 ng/mL. Figure 4.4 shows the calibration curves generated from the real-time data in Figure 4.3 using the initial slopes of the response curves.

Since all antigens are mixed together and introduced simultaneously, it is possible to calibrate all of the sensors at once rather than individually with each antigen. The concentration of each of the antigens was varied within every calibration mixture so that any interferences between antigens could be minimized. In addition, simultaneous calibration with variable concentrations of each antigen helps avoid systematic errors that might be caused by long-term instrument drift or operator error while performing serial dilutions. To ensure reproducibility of the calibrations, each standard solution was analyzed in triplicate. Following analysis of a single solution, the sensor surface was regenerated with glycine buffer (pH 2.2) in preparation for subsequent standard and unknown solution analyses that were all performed sequentially on the same chip. Single-blind analyses of unknown samples containing variable concentrations of all five antigens were interspersed among the calibration standard analyses.

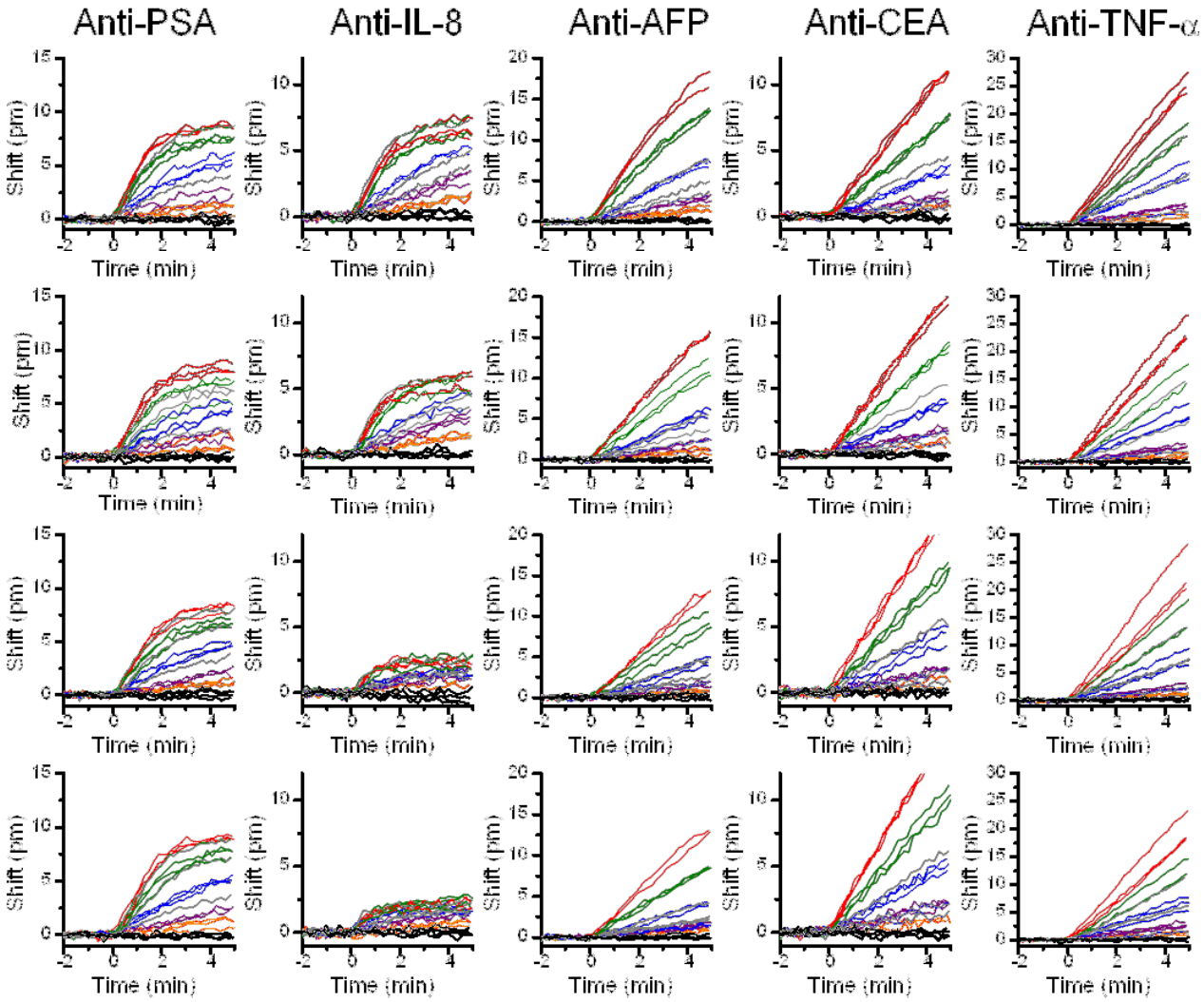

Figure 4.3 Real-time response curves for all sensors used in the experiment. The graphs within each column represent data taken from separate microrings functionalized with the same antibody. For the response curves, the colored lines represent the following concentrations of antigen: red, 150 ng/mL; green, 100 ng/mL; blue, 50 ng/mL; purple, 20 ng/mL; orange, 10 ng/mL; black, 0 ng/mL; gray, unknown solutions.

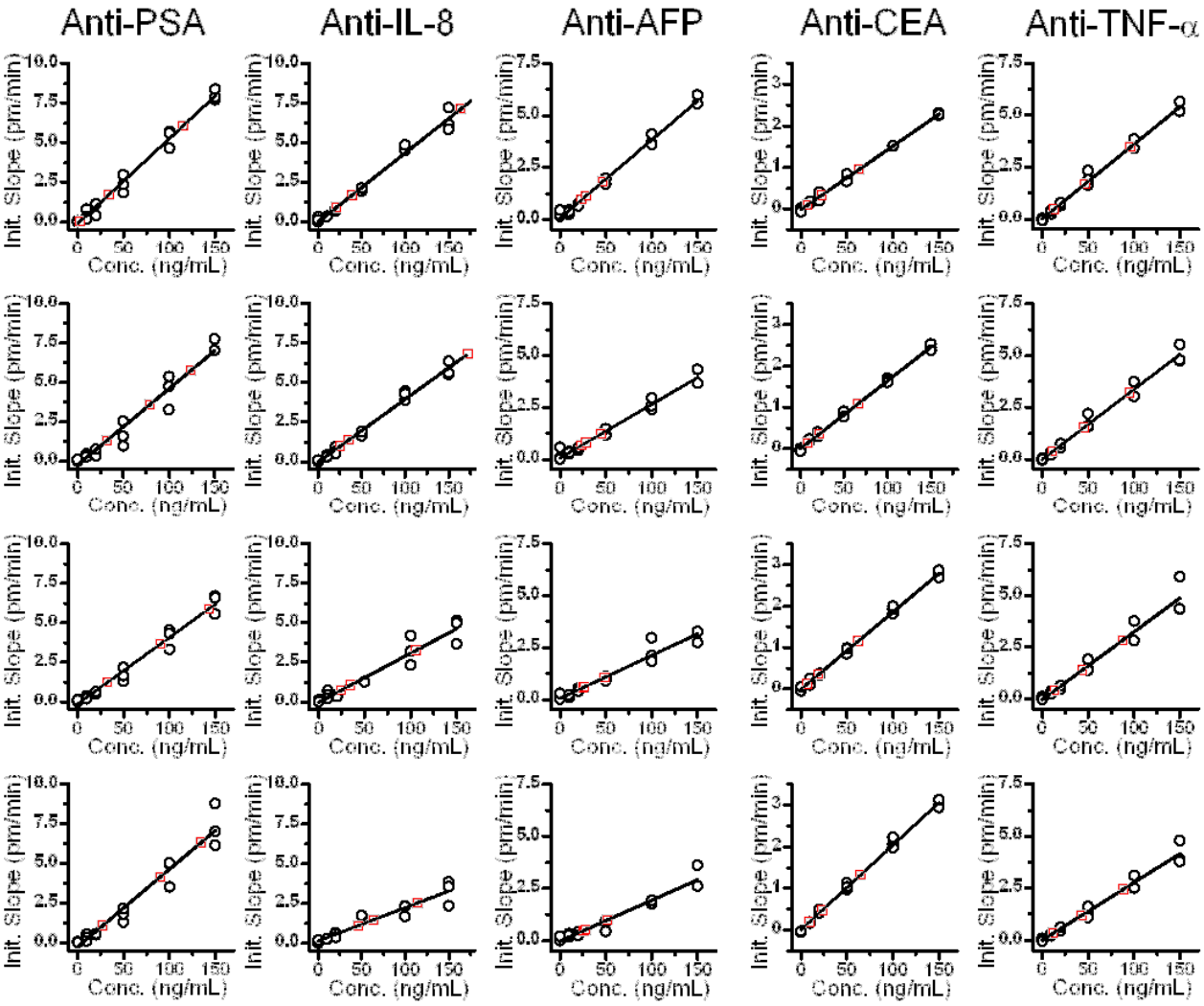

Figure 4.4 Calibration curves generated from the real-time response curves in Figure 4.3. The relative position of a calibration curve in the figure corresponds to the graph in the identical position in Figure 4.3. For these graphs, black circles are calibration points and red squares are unknowns.

Using the calibration curves for each ring, antigen concentrations for the three unknown mixture were determined. Figure 4.5 displays the concentrations of the unknowns as determined using the microring resonator sensors. Table 4.2 shows the actual values for the evaluation of unknowns as given in Figure 4.5. The first column gives the concentration as prepared by the researcher who created the unknowns. The second column lists the concentrations as determined from the calibration curves in Figure 4.4. The uncertainty is then given as the 95% confidence interval based on four independent measurements, and the percent error is the ratio of the prepared concentration and the difference between the prepared and measured concentrations.

Comparing the determined concentrations with the as-prepared values in Figure 4.5, it is apparent that all of the as-prepared concentrations fall within the error bounds of the measurement techniques (95% confidence interval, 4 independent measurements). The average measurement error was approximately 8 ng/mL. Measurements for IL-8 display relatively higher uncertainty compared to the other sensors. However, as shown in Figure 4.5, averaging the results from each of the four microring sensors still enables a reasonably accurate measurement of the concentrations (within 10% of exact concentration), even though the IL-8 precision could be improved. Overall, Figure 4.5 demonstrates that the system can simultaneously quantitate multiple protein biomarkers in solution via a method that would only require a 5-minute analysis, given a pre-calibrated sensor array.

4.4 Conclusions

This chapter describes a critically important development for resonant optical microcavity-based biosensors in that it details the first platform capable of high-level multiplexing and demonstrates that there is no significant sacrifice of absolute sensitivity and measurement precision, compared to an analogous single-parameter analysis. The system described herein—consisting of five antigens in albumin-containing buffer—is admittedly less complex than that encountered in a clinical setting, and future work will focus on analyses in samples such as human serum or whole-cell lysate. Chapter 3 describes complications that can arise due to non-specific adsorption from complex solutions, and therefore efforts to improve the biofouling resistance of the sensor surfaces are being pursued in parallel. While this microfluidic

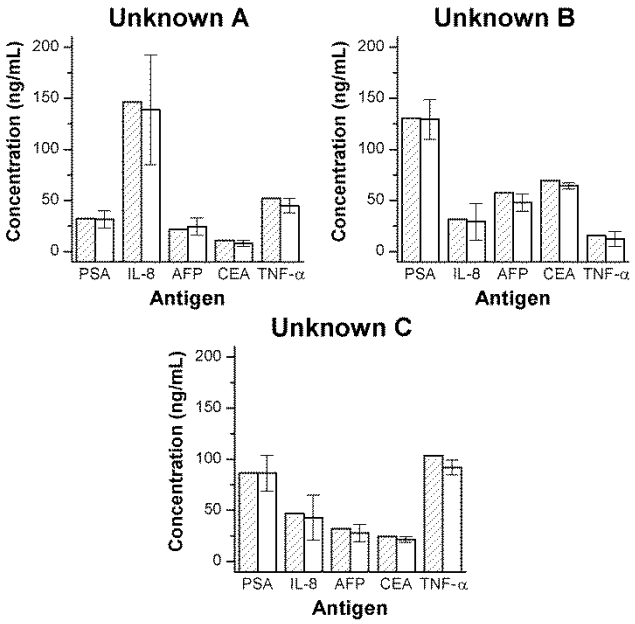

Figure 4.5 Evaluation of unknown protein cocktails A, B, and C comparing the measured values (unfilled bars) with the actual, as-prepared values (bars hatched with diagonal lines) for each of the five antigens. Error bars represent the 95% confidence interval, n = 4 trials.

Table 4.2 Values for unknown determinations: as-prepared concentration values, measured values, the associated uncertainty, and % error.

	Antigen	Prepared Concentration (ng/mL)	Measured Concentration (ng/mL)	Uncertainty (95% C.I.)	% error
Unknown A	PSA	32.4	31.5	8.3	2.7
	IL-8	146.4	138.9	53.7	5.1
	AFP	21.6	24.6	8.6	13.7
	CEA	10.8	8.0	3.0	25.8
	TNF-	52.1	44.8	7.1	13.9
Unknown B	PSA	130.7	129.2	19.3	1.2
	IL-8	31.5	29.3	18.0	7.1
	AFP	57.5	48.1	8.5	16.3
	CEA	69.5	64.2	2.9	7.7
	TNF- α	15.8	12.5	7.2	20.9
Unknown C	PSA	86.6	86.4	17.3	0.2
	IL-8	47.1	43.0	22.1	8.6
	AFP	32.0	27.9	8.5	12.9
	CEA	24.5	21.6	3.0	11.6
	TNF- α	103.6	91.9	7.2	11.3

approach allowed introduction of six different capture agents to the sensor chip surface, higher level multiplexing will require interfacing the microring resonator array with conventional microarray spotting instrumentation, which is facilitated by the current 200 µm ring-to-ring spacing.

4.5 References

(1) Kodadek, T. *Chem. Biol.* **2001**, *8*, 105-115.

(2) Sun, Y. S.; Landry, J. P.; Fei, Y. Y.; Zhu, X. D.; Luo, J. T.; Wang, X. B.; Lam, K. S. *Langmuir* **2008**, *24*, 13399–13405.

(3) Qavi, A. J.; Washburn, A. L.; Byeon, J. Y.; Bailey, R. C. *Anal. Bioanal. Chem.* **2009**, *394*, 121-135.

(4) Fan, X.; White, I. M.; Shopoua, S. I.; Zhu, H.; Suter, J. D.; Sun, Y. *Anal. Chim. Acta* **2008**, *620*, 8-26.

(5) Cunningham, B. T. In *Encycl. Sens.*, 2006; Vol. 5, pp 197-213.

(6) Washburn, A. L.; Gunn, L. C.; Bailey, R. C. *Anal. Chem.* **2009**, *81*, 9499-9506.

(7) Armani, A. M.; Kulkarni, R. P.; Fraser, S. E.; Flagan, R. C.; Vahala, K. J. *Science* **2007**, *317*, 783-787.

(8) Ramachandran, A.; Wang, S.; Clarke, J.; Ja, S. J.; Goad, D.; Wald, L.; Flood, E. M.; Knobbe, E.; Hryniewicz, J. V.; Chu, S. T.; Gill, D.; Chen, W.; King, O.; Little, B. E. *Biosens. Bioelectron.* **2008**, *23*, 939-944.

(9) Zhu, H.; White, I. M.; Suter, J. D.; Dale, P. S.; Fan, X. *Opt. Express* **2007**, *15*, 9139-9146.

(10) Suter, J. D.; White, I. M.; Zhu, H.; Shi, H.; Caldwell, C. W.; Fan, X. *Biosens. Bioelectron.* **2008**, *23*, 1003-1009.

(11) Vollmer, F.; Arnold, S.; Braun, D.; Teraoka, I.; Libchaber, A. *Biophys. J.* **2003**, *85*, 1974-1979.

(12) Ren, H. C.; Vollmer, F.; Arnold, S.; Libchaber, A. *Opt. Express* **2007**, *15*, 17410-17423.

(13) Zhu, H.; White, I. M.; Suter, J. D.; Zourob, M.; Fan, X. *Analyst* **2008**, *133*, 356-360.

(14) Vollmer, F.; Arnold, S.; Keng, D. *Proc. Natl. Acad. Sci.* **2008**, *105*, 20701-20704.

(15) De Vos, K. M.; Bartolozzi, I.; Bienstman, P.; Baets, R.; Schacht, E. *Proc. SPIE* **2007**, *6447*, 64470K.

(16) Wang, S.; Ramachandran, A.; Ja, S.-J. *Biosens. Bioelectron.* **2009**, *24*, 3061-3066.

(17) Xu, D. X.; Densmore, A.; Delâge, A.; Waldron, P.; McKinnon, R.; Janz, S.; Lapointe, J.; Lopinski, G.; Mischki, T.; Post, E.; Cheben, P.; Schmid, J. H. *Opt. Express* **2008**, *16*, 15137-15148.

(18) Yalcin, A.; Popat, K. C.; Aldridge, J. C.; Desai, T. A.; Hryniewicz, J.; Chbouki, N.; Little, B. E.; King, O.; Van, V.; Chu, S.; Gill, D.; Anthes-Washburn, M.; Unlu, M. S. *IEEE J. Sel. Top. Quantum Electron.* **2006**, *12*, 148-155.

(19) Ligler, F. S. *Anal. Chem.* **2009**, *81*, 519-526.

(20) Bailey, R. C. *Bioanalysis* **2009**, *1*, 1043-1047.

(21) Iqbal, M.; Gleeson, M. A.; Spaugh, B.; Tybor, F.; Gunn, W. G.; Hochberg, M.; Baehr-Jones, T.; Bailey, R. C.; Gunn, L. C. *IEEE J. Sel. Top. Quantum Electron.* **2010**, *16*, 654-661.

(22) ***Caution!*** *Piranha solutions are extraordinarily dangerous, reacting explosively with trace quantities of organics*.

(23) Dirksen, A.; Dawson, P. E. *Bioconjugate Chem.* **2008**, *19*, 2543-2548.

(24) Noto, M.; Khoshsima, M.; Keng, D.; Teraoka, I.; Kolchenko, V.; Arnold, S. *Appl. Phys. Lett.* **2005**, *87*, 223901-223901.

Chapter 5

DNA-encoding of Antibodies to Improve Performance and Allow Parallel Evaluation of the Binding Characteristics of Multiple Protein Capture Agents in a Surface-Bound Immunoassay Format

Notes and Acknowledgements

This chapter has been reproduced from the original paper "DNA-encoding of Antibodies to Improve Performance and Allow Parallel Evaluation of the Binding Characteristics of Multiple Protein Capture Agents in a Surface-Bound Immunoassay Format" (Washburn, A. L.; Gomez, J.; Bailey, R. C. Anal. Chem. **2011**, *83*, 3572–3580). It has been reproduced here with permission from the American Chemical Society © 2011.

Joseph Gomez is acknowledged for his assistance in the FPLC purification of the DNA-antibody conjugates.

This work was funded by the NIH Director's New Innovator Award Program, part of the NIH Roadmap for Medical Research, through grant number 1-DP2-OD002190-01, and by the Camille and Henry Dreyfus Foundation. A.L.W. was supported via a National Science Foundation Graduate Research Fellowship.

This article can be accessed online at: http://dx.doi.org/10.1021/ac200317z

5.1 Introduction

A major challenge in developing sensitive and robust protein immunoassays is identifying appropriate antibody capture agents for the intended target antigen. Although assay performance is profoundly affected by the ultimate sensitivity of the analytical methods, an oft-encountered limitation is imposed by poor antibody performance. Furthermore, many ultrasensitive detection techniques acquire their sensitivity from the use of extremely high affinity capture agents rather than fundamentally more sensitive measurement technologies—a complication when performing head-to-head evaluation of different methodologies in the absence of more general comparables. Nonetheless, high affinity protein capture agents are absolutely essential for robust immunoassays, and many hurdles are often encountered in their pursuit. For example, among a selection of commercially available antibodies against a certain target, the equilibrium and kinetic binding constants can vary significantly from vendor to vendor, clone to clone, and even lot to lot. Furthermore, these metrics are rarely available from vendors, making the direct evaluation of the performance of antibodies an important component of biosensor development.

Label-free, refractive index-sensitive sensor platforms,[1-8] have been widely used for evaluating protein-protein binding kinetics. Typically, these methods utilize microspotting or microfluidic technologies to directly create arrays of protein capture agents on the sensor surface in a process that is completely separate from the subsequent interaction screening. Although these screening formats work well for many applications, in this paper we demonstrate an expansion upon these capabilities by utilizing DNA-encoded antibodies for the screening of antibody kinetics using arrays of microring optical resonators. Microring resonators are refractive index-responsive optical devices that our group has recently demonstrated as a versatile tool for the sensitive detection of biomolecules.[9-11] Beyond these detection applications, the modular multiplexing capability of the semiconductor-based platform make it an attractive technology for multiplexed and label-free interaction monitoring.[8]

As described previously,[12-18] DNA microarrays can be converted into antibody arrays via a self-assembly process that involves conjugating antibodies with DNA strands which are complementary to DNA strands immobilized on the surface. Figure 5.1 shows an illustration of

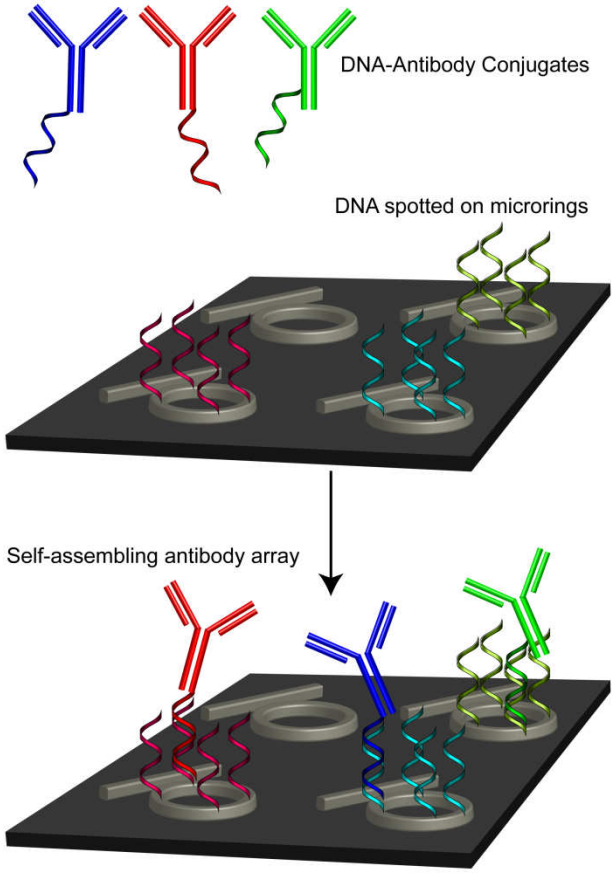

Figure 5.1 Covalent DNA-antibody conjugates (blue, red, and green) are created in parallel with a microring resonator chip (not to scale) that has been functionalized with unique complementary DNA strands via microspotting. After flowing the conjugates over the surface, the conjugates self-assemble onto the chip surface as dictated by the complementary DNA-DNA base pairing interactions. Non-functionalized rings serve as controls since they do not have any DNA-antibody conjugates directed towards them.

this concept whereby ssDNA-tagged antibodies are directed to specific cDNA-modified microrings via the Watson-Crick base pairing of the respective DNA sequences.

Advantages of this approach—both for biomolecule detection as well as capture agent screening—come from several factors. First, DNA microarrays, are generally more robust than protein microarrays on account of the high sensitivity of proteins to denaturation on hydrophobic surfaces,[19, 20] at air/water interfaces,[21] and under dehydrated storage conditions.[22] To avoid these deleterious effects on protein microarrays, microfluidic deposition techniques can be used to create patterned arrays of antibodies *in situ*, immediately before analysis. For example, Nahsol et al. used the ProteOn XPR36 with a 6 x 6 array of fluidics for screening applications.[4] However, microspotting has an advantage over microfluidic approaches in that it can allow larger and higher density arrays to be created. A second advantage of the DNA-encoded strategy comes from the nature of the surface immobilization interaction. Although the DNA-DNA interaction is sufficient to provide a robust linkage under assay conditions, the base-pairing interaction can be disrupted using chaotropic agents. This allows for the regeneration of sensor surfaces even when the desired antibody-antigen interactions are irreversible under standard antibody regeneration conditions (e.g. low pH, high pH, chaotropic, highly chelating, and high ionic strength conditions).[23] This capability can also be advantageously used to dynamically reprogram the specificity of sensor arrays by replacing one set of antibodies with others that have a different set of specificities but are encoded with the same DNA sequences.

In this paper we explored the combined utility of DNA-encoded antibodies and arrays of silicon photonic microring resonators as a versatile, multiplexed bioanalysis platform. We first confirmed the ability of the DNA-encoding strategy to direct antibodies to the appropriately cDNA-modified microring resonators and then validated the antigen-recognition capability of the immobilized capture agents. We next utilized DNA-encoded antibodies to evaluate the kinetics and secondary antibody recognition properties of 12 different commercial capture agents: six that recognized prostate specific antigen (PSA) and six specific for α-fetoprotein (AFP). For kinetic measurements we used the kinetic titration method described by Karlsson et al.,[24] which streamlines the evaluation process by avoiding the need to regenerate the surface between each addition of antigen. We first evaluated the six PSA antibodies in parallel; then after only a 15-minute rinse with 8 M urea, we reprogrammed the same microring resonator array substrate with the six AFP antibodies, which were subsequently interrogated in parallel. In addition to

screening binding kinetics, we also evaluated antibody pairs for secondary antibody recognition of antigen bound to each of the different primary antibodies immobilized on the chip. In this manner we were able to quickly determine which combinations of antibodies could function as a set for sandwich immunoassays. This also provided information about common binding epitopes among antibodies, since it is assumed that antibodies that form sandwich pairs are binding separate epitopes, whereas antibody pairs that bind in a mutually exclusive fashion are assumed to bind to proximal epitopes. Overall, the combination of DNA-encoded antibodies and microring resonator arrays is shown to be a promising combination for not only the evaluation of capture agent binding kinetics, but also other key characteristics that are important in the development of robust protein immunoassays.

5.2 Materials and Methods

5.2.1 Materials

Succinimidyl 4-formylbenzoate (S-4FB), succinimidyl 6-hydrazinonicotinamide acetone hydrazone (S-HyNic), 3-N-((6-(N'-Isopropylidene-hydrazino))nicotinamide)propyltriethyoxy-silane (HyNic Silane), and antibody-oligonucleotide conjugation kits were purchased from SoluLink (San Diego, CA). Custom DNA oligonucleotides were synthesized by Integrated DNA Technologies (Coralville, IA). Monoclonal mouse anti-human PSA antibodies clones B732M, B731M, 5A6, 5G6, 8A6, monoclonal mouse anti-human AFP antibodies clones B491M, 131-12210, 057-11301, 1301, 1305, and purified human AFP and PSA were purchased from Meridian Life Science, Inc. (Saco, ME). Monoclonal mouse anti-human PSA antibody clone 6915780 and monoclonal mouse anti-human AFP antibody clone 2127435 were obtained from Fitzgerald Industries International (Concord, MA). For convenience, all of the antibodies will be referred to by their specificity and clone number for future reference (e.g. anti-AFP-B491M). However, modifications to this convention include: anti-AFP-210 for clone 131-12210, anti-AFP-301 for clone 057-11301, anti-PSA-780 for clone 6915780, and anti-AFP-435 for clone 2127435.

Zeba spin filter columns and Starting Block were purchased from Pierce (Rockford, IL). Vivaspin molecular weight cutoff filters (50,000 and 5,000 Da MWCO), were obtained from GE Healthcare (Waukesha, WI). Phosphate buffered saline (PBS), with a standard 10 mM phosphate

ion concentration, was reconstituted from Dulbecco's phosphate buffered saline packets purchased from Sigma-Aldrich (St. Louis, MO). Aniline was obtained from Acros Organics (Geel, Belgium). All other chemicals were obtained from Sigma-Aldrich and used as received.

All buffers were made with purified water (ELGA PURELAB filtration system; Lane End, UK), and the pH was adjusted as necessary with 1 M HCl or 1 M NaOH. A different PBS buffer with 100 mM phosphate (100 mM PBS) was made with 150 mM NaCl, 22.5 mM monobasic sodium phosphate, and 77.7 mM dibasic sodium phosphate and then pH-adjusted to either pH 7.4 or pH 6.0. PBS with 0.05% Tween-20 (PBST) was made by adding Tween-20 to standard PBS buffer (Dulbecco's formulation). All solutions were degassed under vacuum sonication before being flowed across the sensor surface.

5.2.2 Instrumental Setup and Chip Fabrication

The sensor chips and microring resonator interrogation instrumentation was acquired from Genalyte, Inc. (San Diego, CA), and have been previously described.[25] Each 6 x 6 mm microchip contains thirty-two 30-µm diameter microrings that have adjacent linear waveguides with input and output diffractive grating couplers at each end to enable independent determination of the optical cavity spectrum of each microring using a tunable, external cavity diode laser (center frequency 1560 nm). Resonance wavelengths are measured as the wavelength at which the out-coupled light that propagates past the microring is negatively attenuated. A fluoropolymer cladding layer over the chip with etched annular openings enables exposure of active sensing rings while keeping thermal control rings buried under the cladding layer. In each experiment, twenty-four rings are responsive to surface chemistry and biological modification while eight are left under the cladding as thermal controls. All measurements for these experiments were made with the sensor chips loaded into a custom cell with microfluidic flow channels defined by a 0.007-inch thick Mylar gasket (both single and dual channel) with a previously described design.[9] Solutions were flowed through the chips using an integrated autosampler that draws from Parafilm-coated (Pechiney Plastic Packaging Company; Chicago, IL) polystyrene 96-well plates (Costar brand, Fisher Scientific).

5.2.3 Silane Functionalization

Microring array substrates were first cleaned with piranha solution[26] (3:1 H_2SO_4:30% H_2O_2) for 30 seconds followed by rinsing with water and N_2 drying. To introduce reactive functional groups, the substrates are immersed in a 1 mg/mL solution of HyNic Silane (20 mg/mL HyNic Silane in DMF stock solution diluted to 1 mg/mL with ethanol) for 30 minutes, followed by rinsing with ethanol and then water.

5.2.4 Oligonucleotide Functionalization

Oligonucleotide sequences, which were designed to minimize cross-reactivity between DNA probes, were previously reported for their utility in spatially localizing DNA-antibody conjugates.[16] The exact sequences, named A, A′, B, B′, F, F′, K, K′, L, L′, and M, M′, (where a prime symbol indicates a complementary sequence), are listed in Table 5.1. All oligonucleotides were synthesized with a 5′ amino terminal group to facilitate attachment to either the substrate or antibody. Oligonucleotides were functionalized with S-4FB according to manufacturer (SoluLink) instructions. Briefly, oligonucleotides were buffer exchanged to 100 mM PBS pH 7.4 and then a 20-fold molar excess of S-4FB in DMF was added. Solutions were allowed to react overnight at room temperature and then were buffer exchanged into 100 mM PBS pH 6.0 using 5 kDa MWCO filters.

5.2.5 DNA Spotting

Multiplexed functionality was installed on the microring arrays by alternately spotting 4FB-functionalized DNA strands A, B, F, K, L, M onto a microchip that had been previously functionalized with HyNic Silane. For initial tests with F′-anti-PSA-5A6 and/or B′-anti-AFP-B491M, only strands B and F were added to the chips. In all cases, several rings on each chip were not functionalized with DNA and used as controls. Six-plex chip spotting was achieved using a Nano eNabler spotting system from BioForce Nanosciences (Ames, IA) using a concentration of at least 100 μM DNA in 100 mM PBS buffer pH 6.0 mixed in a 1:1 ratio with

Table 5.1 List of DNA oligonucleotide sequences used. All sequences have a 5′ terminal amino group attached via a 6-carbon chain (5AmMC6 from IDT)

Name	Sequence (5′ to 3′)
A	AAA AAA AAA AAT CCT GGA GCT AAG TCC GTA
A′	AAA AAA AAA ATA CGG ACT TAG CTC CAG GAT
B	AAA AAA AAA AGC CTC ATT GAA TCA TGC CTA
B′	AAA AAA AAA ATA GGC ATG ATT CAA TGA GGC
F	AAA AAA AAA AAT CAG GTA AGG TTC ACG GTA
F′	AAA AAA AAA ATA CCG TGA ACC TTA CCT GAT
K	AAA AAA AAA ATA ATC TAA TTC TGG TCG CGG
K′	AAA AAA AAA ACC GCG ACC AGA ATT AGA TTA
L	AAA AAA AAA AGT GAT TAA GTC TGC TTC GGC
L′	AAA AAA AAA AGC CGA AGC AGA CTT AAT CAC
M	AAA AAA AAA AGT CGA GGA TTC TGA ACC TGT
M′	AAA AAA AAA AAC AGG TTC AGA ATC CTC GAC

DMSO, to slow solvent evaporation. For chips with only one or two different DNA strands added, the DNA was spotted manually using a stereoscope to direct fluid placement. After spotting, the drops of solution were dried on a hot plate (~70 °C) and incubated in 80% relative humidity (or higher) for 1-2 hours to allow rehydration of the DNA on the surface. Chips were then immersed into S-4FB-modified Starting Block. The Starting Block was modified following the same procedure as oligonucleotide functionalization but 100 µL of 5 mg/mL S-4FB was added to 1.5 mL Starting Block. The blocking solution was removed by rinsing with water, and then additional S-4FB modified blocking solution was added to the chip before incubating overnight in a humidity chamber at 4°C. Sensor chips were then rinsed with water, immersed in 8M urea for 20 minutes to remove excess blocking protein, and then finally rinsed with water and dried under nitrogen.

5.2.6 DNA-Antibody Conjugate Synthesis

To create DNA-antibody conjugates, antibodies were first functionalized with S-HyNic following the manufacturer's guidelines.[27] Briefly, S-HyNic in DMF was added in 5-fold molar excess to ~1 mg/mL antibody that had previously been buffer exchanged into 100 mM PBS pH 7.4 with a Zeba spin filter and reacted for at least two hours at room temperature. The antibody was then exchanged into 100 mM PBS pH 6.0 and concentrated using a 50 kDa MWCO filter, which also served to remove residual S-HyNic. The 4FB-modified DNA was then added in 20-fold molar excess to the HyNic-modified antibody solution and allowed to react overnight at 4 °C. DNA-antibody conjugates were then purified away from the excess DNA using a Superdex 200 10/300 GL column on an AKTA FPLC, both from GE Healthcare (Waukesha, WI). The separation was performed at 4 °C with a PBS isocratic elution. The collected fractions were concentrated with 50 kDa MWCO filters to yield purified solutions of DNA-antibody conjugates. The final conjugate concentration measured between 100-400 µg/mL, as determined by measuring the differential absorption at 260 versus 280 nm, corresponding to the DNA and IgG, respectively, using a NanoDrop UV-Vis absorbance system (ThermoFisher Scientific, Wilmington, DE). Alternatively, an oligonucleotide-antibody conjugation kit from SoluLink was used to synthesize and purify the conjugates using a magnetic-bead-based separation, according to manufacturer's instructions. Although both purification methods provided conjugates of

identical analytical behavior, the conjugation kit is advantageous for the parallel preparation of multiple conjugates, as opposed to serial FPLC purification. The following conjugates were synthesized: A′-anti-PSA-8A6, B′-anti-PSA-B732M, F′-anti-PSA-5A6, K′-anti-PSA-780, L′-anti-PSA-B731M, M′-anti-PSA-5G6, A′-anti-AFP-1301, B′-anti-AFP-B491M, F′-anti-AFP-435, K′-anti-AFP-1305, L′-anti-AFP-210, M′-anti-AFP-301.

5.2.7 Validation of DNA-Encoded Antibody Binding to cDNA-Modified Microring Resonators and Subsequent Antigen Recognition Capability

To validate the ability to localize DNA-antibody conjugates onto microrings presenting specific cDNAs (strands F and B), we tested F′-anti-PSA-5A6 and B′-anti-AFP-B491M. A solution of 20 µg/mL of the B′-anti-AFP-B491M conjugate was first flowed across the surface followed by 5 µg/mL of the F′-anti-PSA-5A6 conjugate. Because the relative binding rates of the DNA-antibody conjugates varied, the concentrations were adjusted so that the so that binding would occur at a similar rate. Following addition of conjugates, 1 µg/mL of AFP and then 1 µg/mL of PSA were flowed across the chip surface.

To test the loading-response behavior of the anti-PSA-5A6 antibody, two methods were used. First, several chips functionalized with strand F had different surface densities of F′-anti-PSA-5A6 added to the surface by varying the concentration of the conjugate added to the chip as well as the incubation time of the conjugate. Following addition of the conjugate, 1 µg/mL of PSA was flowed across the surface and the equilibrium, saturation response was measured after 5 minutes of exposure. Following this test, each chip was regenerated by flowing 8M urea over the chip surface for 15 minutes with water rinses before and after the urea. This enabled antibody conjugates loading to be repeated multiple times.

To compare the capture performance of DNA-encoded antibodies with those directly immobilized on the sensor surface via a covalent linkage with HyNic silane (as we have described previously[28]), we flowed 4FB-modified anti-PSA-5A6 (using the same procedure as the S-HyNic modification, but substituting S-4FB for S-HyNic) over HyNic-silane-functionalized sensor chips. We utilized a previously-described 4-channel flow cartridge[8] to react rings with different concentrations of anti-PSA-5A6 from 0.7 µg/mL to 7 µg/mL. The variations in concentration enabled different amounts of capture antibody to be loaded on different rings on

the same chip, as directly measured by monitoring the real-time shifts in microring resonance wavelength during antibody immobilization. Since these surfaces could not be regenerated to reload antibody, two separate chips (8 channels total) were used to collect the covalent immobilization data. After functionalizing the chip with anti-PSA-5A6, the chip was blocked overnight with 4FB-modified Starting Block and then loaded into a flow cartridge with a single channel to direct the antigen solution over all the sensor rings. Then a solution containing1 µg/mL of PSA was flowed over the chip and the saturation response was measured after 5 minutes of exposure.

5.2.8 DNA-antibody Conjugate Kinetic Screening Experiments

To load a DNA-antibody conjugate onto a chip, ~5 µg/mL (or higher concentration if DNA-DNA binding kinetics for a particular pair of complementary strands were slow) of conjugate was flowed over the chip surface and terminated with a buffer rinse of PBST after loading enough antibody to create a 30-50 pm shift. Saturation experiments with PSA were made by flowing 1 µg/mL PSA in PBST over the chip for 5 minutes. A chip surface could be regenerated by flowing 8M urea over the chip surface for 15 minutes with water rinses before and after the urea. Before performing the multiplexed kinetic evaluation experiments, the DNA-antibody conjugates were tested individually to ensure that no cross-reactivity occurred and to determine the relative binding rate of each conjugate. Thereafter, conjugates could be added simultaneously by adjusting the concentrations so that the rate of addition to the surface was similar for all of the DNA-antibody conjugates, and thus, equivalent loadings were achieved for a single functionalization time period. Kinetic titration experiments were made by adding increasing concentrations of PSA or AFP for a 1.5-minute antigen association period followed by a 4.5-minute rinse with PBST during which desorption of the antigen was observed.

Screening for secondary antibodies was accomplished by loading all six of the DNA-antibody conjugates for a particular antigen over the chip surface and then adding 1 µg/mL of the appropriate antigen (PSA or AFP) for 5 minutes. Following this step, each antibody (not conjugated to DNA) was flowed sequentially over the chip at a concentration of 1 µg/mL. Each chip was loaded into a flow cartridge with two separate microfluidic channels so that each channel could have a different sequence of antibodies flowed over the chip. Following sequential

addition of all 6 antibodies for a particular antigen on both channels, the chip was then regenerated with 8M urea, and the experiment was repeated with different sequences of antibodies added to each channel.

5.2.9 Data Analysis

Raw microring resonance wavelength data, recorded as a function of time, was corrected for any thermal drift of bulk refractive index shifts using on-chip control rings (exposed to solution, but not functionalized with DNA). The signal from all of the control rings was averaged and then subtracted from each of the individual active sensor rings. Kinetic titration data was divided into association and dissociation traces and fit (OriginPro 8.1; OriginLab Corporation; Northampton, MA) using the integrated rate equation for one-to-one Langmuir binding, as described by Karlsson et al.[24]

5.3 Results and Discussion

5.3.1 Validation of DNA-Antibody Conjugate Functionality

Before measuring the kinetics of binding to DNA-antibody conjugates, we first wanted to validate the functionality of the conjugates both in terms of loading onto ssDNA-presenting microrings as well as their subsequent ability to recognize the targeted antigen. Initially, both F′-anti-PSA-5A6 and B′-anti-AFP-B491M were sequentially loaded onto a chip functionalized with DNA strands F and B. Next, a saturating concentration (1 µg/mL) of AFP and then PSA were flowed across the chip. As can be seen in Figure 5.2A, introduction of the antibody conjugates results in large, positive shifts in the resonance wavelength (Δ pm), consistent with biomolecular deposition. The subsequent addition allows us to confirm that there is no non-complementary binding on rings to which a conjugate has not been specifically encoded in accordance with Watson-Crick base pairing. In addition, introduction of a high (1 µg/mL) concentration of AFP and then PSA to all the rings only results in a response on the rings functionalized with the specific DNA-antibody conjugates. From these results we can conclude that the DNA-antibody conjugates self-assemble to the appropriate sensor location and retain their specificity towards a target analyte.

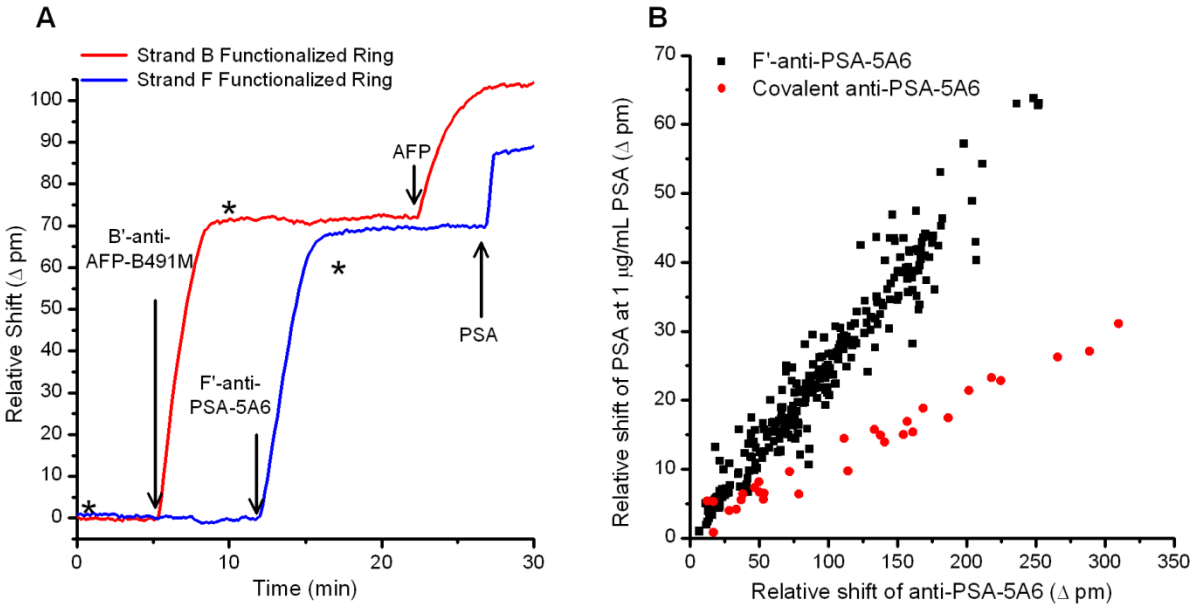

Figure 5.2 (A) Initial validation of DNA-antibody conjugates showing orthogonal antibody loading and orthogonal antigen response. First B′-anti-AFP-B491M was added followed by F′-anti-PSA-5A6. Then 1 µg/mL of AFP was added followed by 1 µg/mL PSA. The red trace shows the response of a microring functionalized with DNA strand B and the blue trace shows the response of a microring functionalized with DNA strand F. For reference, an arrow is positioned at the time points of injection and asterisks (*) indicate the switch to running buffer. (B) Shift in resonance wavelength for F3′-anti-PSA-5A6-presenting microring resonators to 1 µg/mL PSA versus the amount (in units of Δpm) of F3′-anti-PSA-5A6 originally loaded onto the sensors before antigen interaction. The slope of the DNA-encoded antibody loading versus antigen response is ~2.5-fold greater than that for covalently bound antibody, indicating an increased ability to bind to antigen.

We also sought to investigate batch-to-batch and chip-to-chip robustness of DNA-antibody conjugates, particularly in regards to the correlation between antigen binding response and the amount of antibody bound to the sensor. Using F′-anti-PSA-5A6, we performed multiple tests measuring the binding capacity of the antibody on the surface as a function of the amount of conjugate added to the DNA-functionalized surface. This was done by first adding F′-anti-PSA-5A6 to a chip functionalized with the complementary DNA strand F, a process that was measured in real-time to establish the relative amount of antibody bound to each microring. Following the addition of the conjugate, 1 μg/mL PSA was flowed over the surface and the saturating antigen response signal generated was recorded. Using 8M urea to disrupt the DNA duplex formed between conjugate and ring surface, a single sensor chip could easily be reloaded multiple times with different amounts of conjugate via regeneration after measurement of antigen binding responses. In this way, it was very easy to rapidly accumulate a large amount of data establishing a correlation between antibody loading and antigen binding response. We also measured the response from multiple sensor chips and several batches of F′-anti-PSA-5A6 conjugates, and the entirety of these data sets are compiled together as the black squares in Figure 5.2B. Impressively, the amount of antigen binding response is very well-correlated to antibody loading, a linear trend that holds across multiple sensor chips and independently synthesized batches of DNA-antibody conjugate.

For the sake of comparison, we performed a similar study using antibodies that were covalently tethered to the sensor surface, using a previously reported hydrazone linkage-based bioconjugate strategy.[28] The same anti-PSA-5A6 antibody used to make the DNA-antibody conjugates was directly attached to the sensor chips while recording the accompanying shift in resonance wavelength. The sensor chip was then exposed to 1 μg/mL PSA and the response was measured. This process was repeated for a second sensor chip, and all of the results are plotted as the circular red data points in Figure 5.2B. A linear relationship between antibody loading and antigen binding response is again observed, but the slope is 2.5 times greater in the case of the DNA-conjugate. Although the mechanism of this increase in antigen recognition capacity is still under investigation, we preliminarily attribute it to the fact that the underlying DNA functionalized microring surface is sufficiently hydrophilic to minimize the denaturation of attached antibodies through non-specific interactions. Furthermore, the flexibility afforded by the

DNA linker might allow the antibody to sample more optimal orientations for antigen capture, as opposed to the shorter and more rigid covalent linkage.

5.3.2 Validation of Multiplex DNA-Antibody Conjugate Chip

Having validated the performance and established the utility of DNA-antibody conjugates for antigen binding, we then created multiplexed substrates that presented different DNA strands (named A, B, F, K, L, M) on each sensor chip. Figure 5.3A demonstrates that complementary DNA strands bind specifically to the rings functionalized with the complementary surface-bound probes. As 1 μM complementary DNA strands A′, B′, F′, K′, L′, M′ are added sequentially, each set of rings with appropriate complementary strands shows a specific signal to the appropriate DNA strand with minimal cross reactivity. Similarly, Figures 5.3B and 5.3C show the specific binding of the anti-PSA and anti-AFP DNA-encoded antibody conjugates, respectively. Again, only the appropriate rings respond as each DNA-encoded antibody is added sequentially.

5.3.3 Kinetic Analysis of Six Anti-PSA and Six Anti-AFP Antibodies

Following the determination that all six conjugates could be loaded without any non-specific antibody localization, these 6-plex chips were then used to simultaneously evaluate the kinetic binding characteristics of multiple, commercially-available protein capture agents recognizing either PSA or AFP.

In order to expedite the data collection process for screening the binding characteristics of multiple antibodies, we followed the strategy of Karlsson and coworkers,[24] who previously reported a kinetic titration method. This method enables subsequent additions of antigen solutions without having to regenerate in between.

Starting with a sensor chip spotted with 6 different ssDNAs at unique spatial locations, six different DNA-antibody conjugates were simultaneously loaded onto the sensor chip by flowing a mixture of all the conjugates simultaneously over the entire chip surface. In an effort to avoid the deleterious effects of steric crowding on kinetic measurements,[29, 30] the amount of each bound antibody was maintained in the range of 450-750 pg/mm^2, (30-50 pm resonance wavelength shift, as established previously[31]). The six anti-PSA antibodies were evaluated

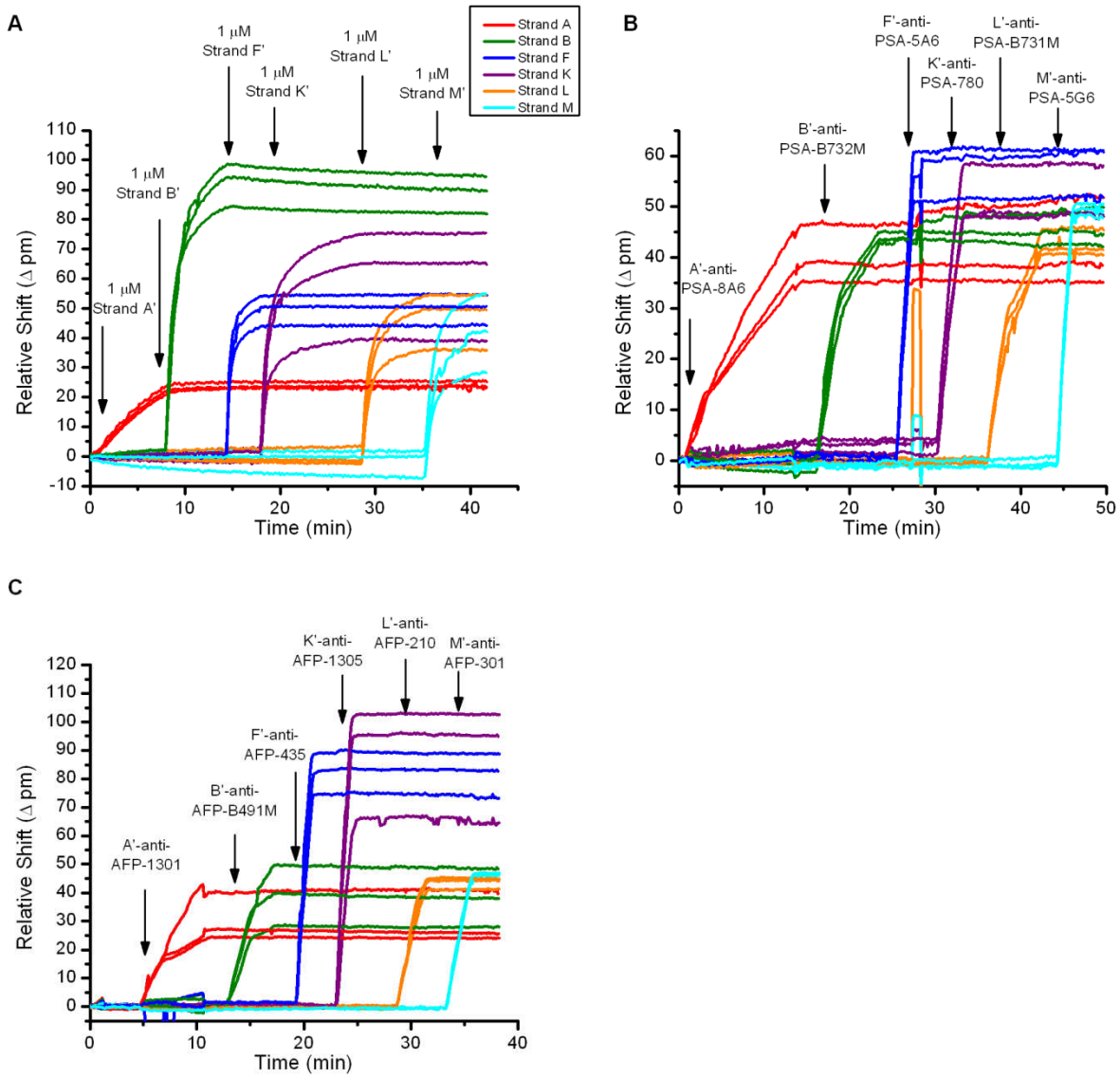

Figure 5.3 Real time data plots showing resonance wavelength shifts for arrays of microrings functionalized with 6 different DNA strand sequences (strands A, B, F, K, L, and M, each shown in a different color, as seen in the legend). (A) Sequential addition of 1 μM complementary DNA strands A′, B′, F′, K′, L′, M′ with no apparent cross-reactivity since only the appropriate rings respond at the time point at which the complementary strand is added. (B) Sequential addition of 6 different DNA-anti-PSA conjugates with appropriate complementary DNA. Again, only the appropriate rings respond at the time point during which the conjugate with the complementary DNA is added, so there is no apparent cross reactivity. The jump at ~27 minutes comes from an air bubble. (C) A similar experiment as in (D) but using anti-AFP conjugates. Again, no cross reactivity is observed.

initially, before the surface was regenerated with 8M urea and the six anti-AFP antibodies were added to the chip. Each titration consisted of 1.5-minute association phases of solutions containing 10, 20, 50, 100, 300, 1000, 5000 ng/mL concentrations of antigen (either PSA or AFP) with 4.5-minute dissociation rinses with buffer.

Figures 5.4A and 5.4B show the real-time shifts in resonance wavelength during the aforementioned kinetic titrations for both anti-PSA and anti-AFP antibodies, respectively. Each set of traces was normalized according to the amount of each antibody loaded onto the sensor array. Measurements were made in triplicate for each antibody, with six control rings comprising the rest of the 24-element sensor array. However, for clarity, data from only a single representative microring per antibody is shown.

As shown in Figure 5.4A, A′-anti-PSA-8A6 and K′-anti-PSA-780 conjugates show very low binding activity. To verify that the poor antigen recognition was not due to the covalently-attached DNA, we tested all of the antibodies without pendant DNA by flowing them over a surface with immobilized rabbit-anti mouse IgG-Fc (RAM-Fc) (data not shown). Because the RAM-Fc binds mouse IgG in the Fc region, away from the antigen recognition sites, this method does not require antibody modification and has been used to orient antibodies on biosensor surfaces.[32] Comparing the RAM-Fc immobilization approach to the DNA-assembled approach, the antigen binding behavior remained consistent between methods, with anti-PSA-8A6 and anti-PSA-780 displaying poor antigen binding performance in either case.

Figure 5.4B shows the real-time shifts in resonance wavelength for the six anti-AFP antibodies in a manner identical to the anti-PSA antibodies (Figure 5.4A). In this case, all the antibodies responded well and most of the antibodies had similar association and dissociation rates. Only K′-anti-AFP-1305 displayed markedly different behavior, in contrast to the collection of anti-PSA antibodies, which showed greater variation in binding kinetics.

In order to quantitatively evaluate the binding kinetics of the arrayed antibodies, the real-time shifts in resonance wavelength from the kinetic titration were fit using the integrated rate equation for the one-to-one Langmuir binding model. Figures 5.5 and 5.6 show the results of this fitting to the anti-PSA and anti-AFP antibodies, respectively. As noted above, the A′-anti-PSA-8A6 and K′-anti-PSA -780 antibodies showed poor binding activity, which presented complications in fitting these data sets. For A′-anti-PSA-8A6, the poor binding translated to a

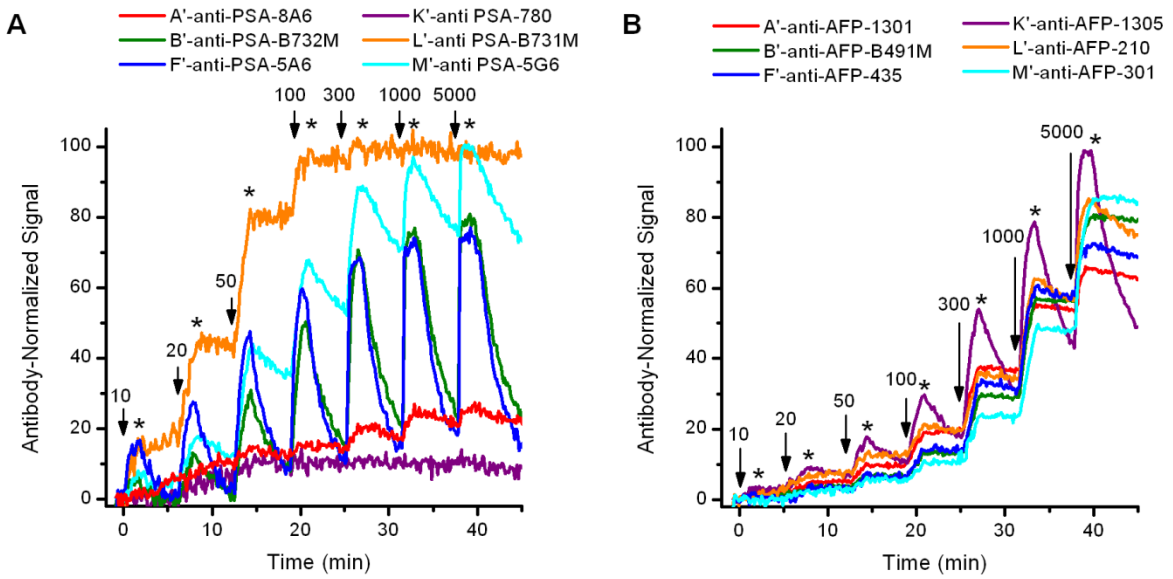

Figure 5.4 Real-time shifts in resonance wavelength from representative microring resonators functionalized with unique antibodies upon exposure to A) PSA, and B) AFP in a kinetic titration assay format. In both panels, solutions containing the targeted antigen at the listed concentrations (in units of ng/mL) are introduced for 1.5 minutes at time points indicated by black arrow. After this association phase, the solution was switched to buffer (as indicated with asterisks) and a 4.5 minute dissociation phase was recorded.

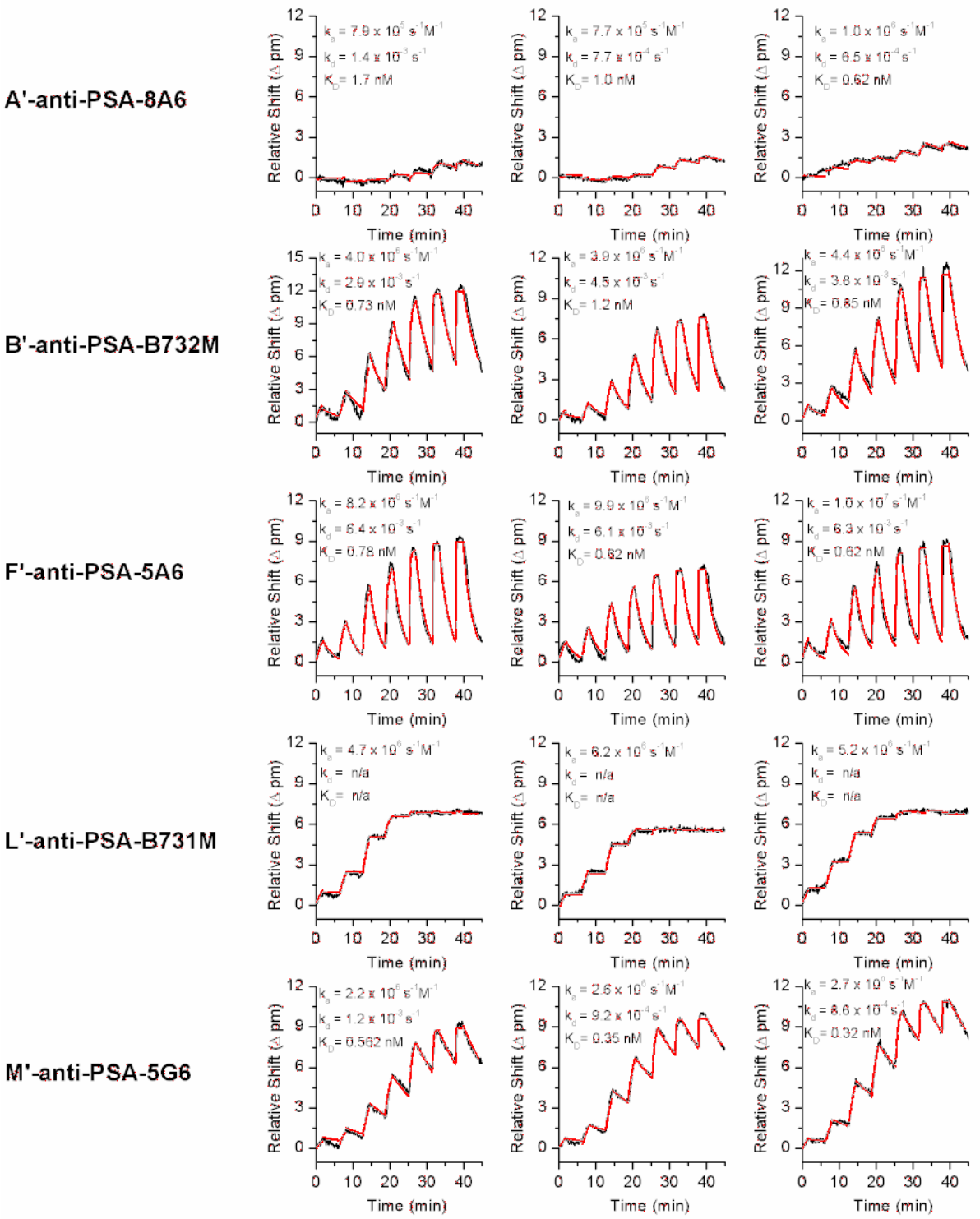

Figure 5.5 Real time data plots showing the kinetic titrations for 15 microring sensors (three sensors per antibody conjugate) for the anti-PSA conjugates. The black traces indicate the real time data, and the red traces indicate the global fit via a one-to-one Langmuir binding model. In each graph, the calculated k_a, k_d, and K_D from the fit are listed, except for L′-anti-PSA (B731M), which had too slow of a dissociation rate to accurately measure, thus "n/a" is given for those values. Also, anti-PSA-780 performed too poorly to generate a reliable fit, so the data for K′-anti-PSA-780 is not shown.

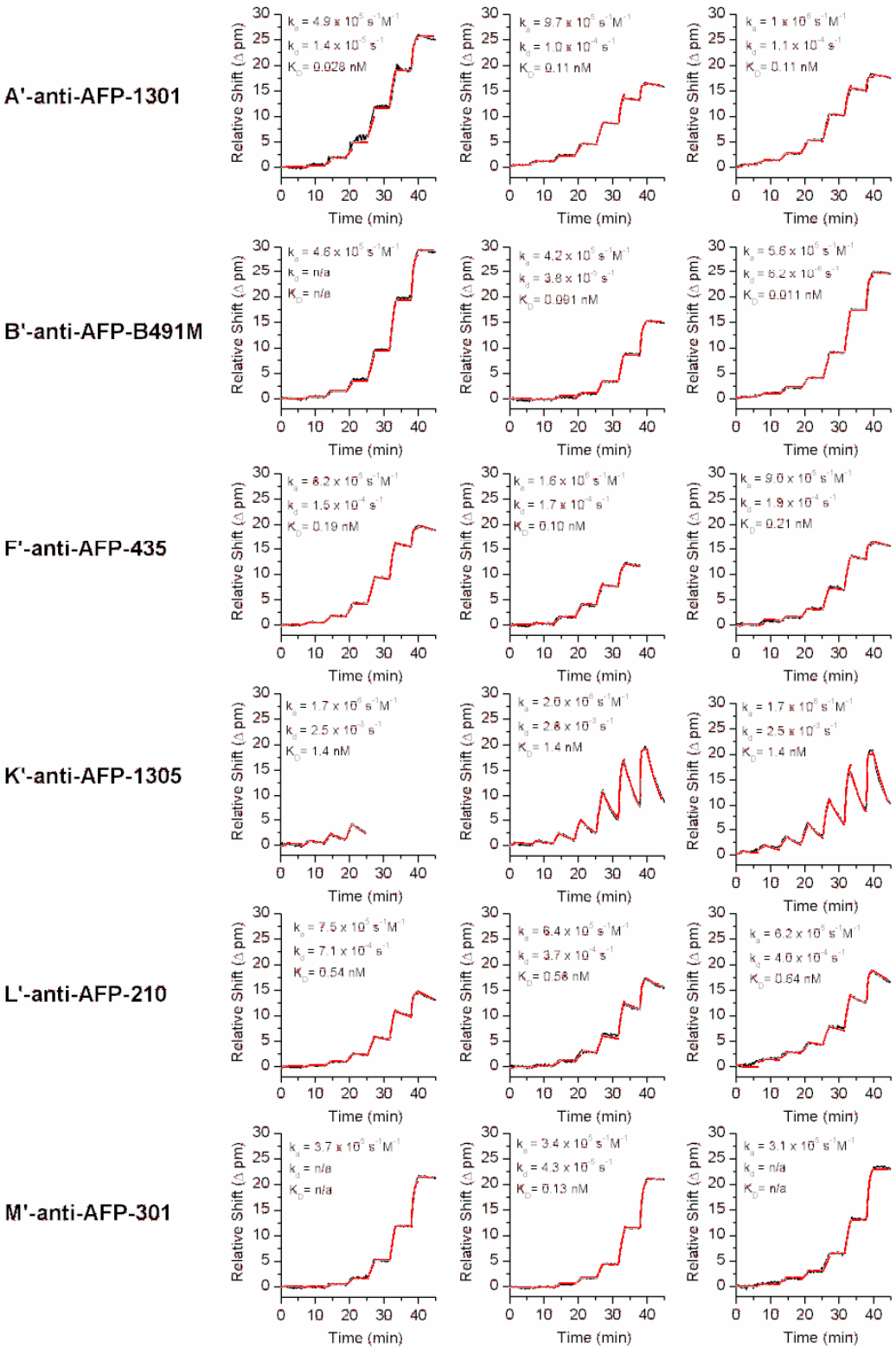

Figure 5.6 Real time data plots showing the kinetic titrations for 18 microring sensors (three sensors per antibody conjugate) for the anti-AFP conjugates. The black traces indicate the real time data, and the red traces indicate the global fit via a one-to-one Langmuir binding model. In each graph, the calculated k_a, k_d, and K_D from the fit are listed, except for a few of the plots, which had too slow of a dissociation rate to accurately measure, thus "n/a" is given for those values.

poor fit, whereas we were unable to fit binding parameters for K′-anti-PSA -780, thus its omission from the figure.

Table 5.2 summarizes the average values for the kinetic association (k_{on}) and dissociation rates (k_{off}) and equilibrium dissociation constant ($K_D = \frac{k_{off}}{k_{on}}$) determined from the fitting the resonance wavelength shifts for the microring array during the kinetic titration assays. As described above, the poor performance of the K′-anti-PSA -780 antibody prohibited accurate fitting to the model, and thus did not allow for determination of kinetic or equilibrium binding constants. Furthermore, L′-anti-PSA-B731M possessed an incredibly slow dissociation rate that was difficult to measure (even over longer dissociation times than described herein), and thus an accurate k_d (and K_D) could not be attained, although the affinity appears to be very high.

Due to subtle variations in experimental conditions and measurement methodology, as well as uncertainties in fitting, experimentally derived kinetic and equilibrium binding values often have variances from group-to-group or technology-to-technology, making absolute, cross-platform comparisons of protein-protein interactions difficult. However, by comparing six antibodies side by side in identical assay conditions within same microfluidic volume, we demonstrate a direct, head-to-head comparison of antibodies which can enable accurate selection of an antibody for a particular assay. For example, a fast association rate may desirable for certain applications where kinetics are of utmost importance. However, a slow dissociation rate may be preferred when the tightest possible binding (smallest K_D) is needed, or if antigen needs to stay bound for additional rinse or recognition steps, such as with a sandwich-type assay. The parallel screening method presented herein provides a straightforward approach to rationally selecting antibodies with optimal characteristics for the desired assay.

5.3.4 Antibody Sandwich Pair Screening

In addition to characterizing the binding kinetics of each individual antibody, the easily programmable and readily regenerable DNA-encoded microring sensor array also provides a mechanism to rapidly screen for antibody sandwich pairs. The six DNA-antibody conjugates recognizing either PSA or AFP were loaded onto the chip surface, and then a high concentration of antigen was flowed over the sensor array, giving a saturated binding response. Each individual antibody (non-DNA conjugated) was sequentially flowed over the chip and sandwich pairs were

Table 5.2 List of kinetic and equilibrium binding parameters for DNA-antibody conjugates interacting with their target antigen.

		k_a ($s^{-1}M^{-1} \times 10^{-5}$)	k_d ($s^{-1} \times 10^{4}$)	K_D (nM)
PSA antibody conjugates	A′-anti-PSA-8A6	8.7	9.2	1.1
	B′-anti-PSA-B732M	41	38	0.91
	F′-anti-PSA-5A6	94	63	0.67
	L′-anti-PSA-B731M	54	-	-
	K′-anti-PSA-780	-	-	-
	M′-anti-PSA-5G6	25	10	0.40
AFP antibody conjugates	A′-anti-AFP-1301	8.3	0.75	0.0091
	B′-anti-AFP-B491M	4.8	0.22	0.0046
	F′-anti-AFP-435	11	1.7	0.015
	K′-anti-AFP-1305	18	26	1.4
	L′-anti-AFP-210	6.7	3.9	0.58
	M′-anti-AFP-301	3.4	0.43	0.12

identified when shifts in resonance wavelength indicated the binding of the second antibody to the pre-bound antigen. After flowing all six antibodies in sequence, a urea regeneration step was used to strip the surface, which could then be reloaded with primary antibody conjugates and the process repeated with a different secondary introduction sequence. This reordering ensured that if the binding of one sandwich pair interfered with the binding of a second antibody, there would be an opportunity for the second antibody to be tested without the first antibody having been flowed over the surface already. By using a fluidic system that featured two identically-encoded channels, all sandwich pairs were unambiguously assessed using only a single regeneration (4 tests overall). The results of these screening efforts are summarized in Table 5.3 (PSA) and Table 5.4 (AFP). As expected for monoclonal antibodies, capture agents did not show secondary recognition of antigens already bound to themselves, as the epitope was blocked during primary binding. Furthermore, in all cases successful sandwich pairs work in both configurations where either antibody is surface-immobilized and the other acting as the solution-phase secondary recognition agent. Interestingly, both the anti-PSA and anti-AFP libraries show a large number of valid sandwich pairs. Anti-AFP antibodies exhibit a somewhat larger selection of sandwich pairs than the anti-PSA antibodies; this is not totally unexpected given that AFP is a larger protein than PSA, and would therefore possess more potential epitopes. Similarly, non-compatible sandwich pairs suggest that the antibodies bind to identical or proximal recognition domains and these types of analysis represent a form of epitope mapping. For example, anti-AFP-1301, anti-AFP-780, and anti-AFP-210 all seem to bind to a similar location on the antigen since their binding is mutually exclusive. Overall, the results show how readily secondary binding agent compatibility can be determined using a multiplexed sensor array of DNA-encoded antibodies, and suggest a straight-forward and efficient method for identifying pairs of capture agents that might be useful in sandwich-type immunoassays.

5.4 Conclusions

In this study we demonstrated the robust nature and utility of DNA-encoded antibodies for the multiplexed screening of capture agent binding properties, in terms of screening both their kinetic and equilibrium binding metrics, as well as their compatibility for forming sandwich pairs around a single antigen. Furthermore, this antibody attachment scheme appears

Table 5.3 Anti-PSA sandwich pair screening results showing sandwich-pair interactions ("X") between surface-immobilized primary antibodies (row headings) and solution-phase secondary antibodies (column headings).

	anti-PSA-8A6	**anti-PSA-B732M**	**anti-PSA-5A6**	**anti-PSA-780**	**anti-PSA-B731M**	**anti-PSA-5G6**
A′-anti-PSA-8A6	-	-	X	-	X	X
B′-anti-PSA-B732M	-	-	-	X	-	-
F′-anti-PSA-5A6	X	-	-	X	X	X
K′-anti-PSA-780	-	X	X	-	X	X
L′-anti-PSA-B731M	X	-	X	X	-	-
M′-anti-PSA-5G6	X	-	X	X	-	-

Table 5.4 Anti-AFP sandwich pair screening results showing sandwich-pair interactions ("X") between surface-immobilized primary antibodies (row headings) and solution-phase secondary antibodies (column headings).

	anti-AFP-1301	**anti-AFP-B491M**	**anti-AFP-435**	**anti-AFP-1305**	**anti-AFP-210**	**anti-AFP-301**
A′-anti-AFP-1301	-	X	-	X	-	X
B′-anti-AFP-B491M	X	-	X	X	X	X
F′-anti-AFP-435	-	X	-	X	-	X
K′-anti-AFP-1305	X	X	X	-	X	X
L′-anti-AFP-210	-	X	-	X	-	X
M′-anti-AFP-301	X	X	X	X	X	-

to offer multiple advantages over covalent immobilization in terms of antibody binding capacity, and array regeneration and reprogramming capabilities, thus reducing the need for complex microfluidic designs. Coupled with the inherent long term solution-phase storage stability of the DNA-antibody conjugates and ssDNA-functionalized sensor array, we envision that DNA-encoded antibodies will continue to be a valuable tool for both protein detection and the multiplexed evaluation of capture agent binding characteristics on a variety of transduction methodologies.

5.5 References

(1) Krishnamoorthy, G.; Beusink, J. B.; Schasfoort, R. B. M. *Anal. Methods* **2010**, *2*, 1020-1025.

(2) Krishnamoorthy, G.; Carlen, E. T.; Bomer, J. G.; Wijnperle, D.; deBoer, H. L.; Berg, A. v. d.; Schasfoort, R. B. M. *Lab Chip* **2010**, *10*, 986-990.

(3) Bravman, T.; Bronner, V.; Lavie, K.; Notcovich, A.; Papalia, G. A.; Myszka, D. G. *Anal. Biochem.* **2006**, *358*, 281-288.

(4) Nahshol, O.; Bronner, V.; Notcovich, A.; Rubrecht, L.; Laune, D.; Bravman, T. *Anal. Biochem.* **2008**, *383*, 52-60.

(5) Hosse, R. J.; Tay, L.; Hattarki, M. K.; Pontes-Braz, L.; Pearce, L. A.; Nuttall, S. D.; Dolezal, O. *Anal. Biochem.* **2009**, *385*, 346-357.

(6) Özkumur, E.; Needham, J. W.; Bergstein, D. A.; Gonzalez, R.; Cabodi, M.; Gershoni, J. M.; Goldberg, B. B.; Ünlü, M. S. *Proc. Natl. Acad. Sci. U. S. A.* **2008**, *105*, 7988-7992.

(7) Olkhov, R. V.; Shaw, A. M. *Anal. Biochem.* **2010**, *396*, 30-35.

(8) Byeon, J.-Y.; Bailey, R. C. *Analyst* **2011**, DOI: 10.1039/c1030an00853b.

(9) Washburn, A. L.; Gunn, L. C.; Bailey, R. C. *Anal. Chem.* **2009**, *81*, 9499-9506.

(10) Washburn, A. L.; Luchansky, M. S.; Bowman, A. L.; Bailey, R. C. *Anal. Chem.* **2010**, *82*, 69-72.

(11) Luchansky, M. S.; Bailey, R. C. *Anal. Chem.* **2010**, *82*, 1975-1981.

(12) Boozer, C.; Ladd, J.; Chen, S.; Yu, Q.; Homola, J.; Jiang, S. *Anal. Chem.* **2004**, *76*, 6967-6972.

(13) Boozer, C.; Ladd, J.; Chen, S. F.; Jiang, S. T. *Anal. Chem.* **2006**, *78*, 1515-1519.

(14) Ladd, J.; Boozer, C.; Yu, Q.; Chen, S.; Homola, J.; Jiang, S. *Langmuir* **2004**, *20*, 8090-8095.

(15) Bailey, R. C.; Kwong, G. A.; Radu, C. G.; Witte, O. N.; Heath, J. R. *J. Am. Chem. Soc.* **2007**, *129*, 1959-1967.

(16) Fan, R.; Vermesh, O.; Srivastava, A.; Yen, B. K. H.; Qin, L.; Ahmad, H.; Kwong, G. A.; Liu, C.-C.; Gould, J.; Hood, L.; Heath, J. R. *Nat. Biotechnol.* **2008**, *26*, 1373-1378.

(17) Schroeder, H.; Adler, M.; Gerigk, K.; Müller-Chorus, B.; Götz, F.; Niemeyer, C. M. *Anal. Chem.* **2009**, *81*, 1275-1279.

(18) Wacker, R.; Schröder, H.; Niemeyer, C. M. *Anal. Biochem.* **2004**, *330*, 281-287.

(19) Maruyama, T.; Katoh, S.; Nakajima, M.; Nabetani, H.; Abbott, T. P.; Shono, A.; Satoh, K. *J. Membr. Sci.* **2001**, *192*, 201-207.

(20) Vermeer, A. W. P.; Giacomelli, C. E.; Norde, W. *Biochim. Biophys. Acta, Gen. Subj.* **2001**, *1526*, 61-69.

(21) Sen, P.; Yamaguchi, S.; Tahara, T. *J. Phys. Chem. B* **2008**, *112*, 13473-13475.

(22) MacBeath, G.; Schreiber, S. L. *Science (Wash.)* **2000**, *289*, 1760-1763.

(23) Andersson, K.; Hamalainen, M.; Malmqvist, M. *Anal. Chem.* **1999**, *71*, 2475-2481.

(24) Karlsson, R.; Katsamba, P. S.; Nordin, H.; Pol, E.; Myszka, D. G. *Anal. Biochem.* **2006**, *349*, 136-147.

(25) Iqbal, M.; Gleeson, M. A.; Spaugh, B.; Tybor, F.; Gunn, W. G.; Hochberg, M.; Baehr-Jones, T.; Bailey, R. C.; Gunn, L. C. *IEEE J. Sel. Top. Quantum Electron.* **2010**, *16*, 654-661.

(26) ***Caution!*** *Piranha solutions are extraordinarily dangerous, reacting explosively with trace quantities of organics.*

(27) Solulink protocols. http://www.solulink.com/support/protocols (accessed December 28, 2010).

(28) Byeon, J.-Y.; Limpoco, F. T.; Bailey, R. C. *Langmuir* **2010**, *26*, 15430-15435.

(29) Myszka, D. G. *J. Mol. Recognit.* **1999**, *12*, 279-284.

(30) Karlsson, R.; Michaelsson, A.; Mattsson, L. *J. Immunol. Methods* **1991**, *145*, 229-240.

(31) Luchansky, M. S.; Washburn, A. L.; Martin, T. A.; Iqbal, M.; Gunn, L. C.; Bailey, R. C. *Biosens. Bioelectron.* **2010**, *26*, 1283-1291.

(32) Nice, E.; Layton, J.; Fabri, L.; Hellman, U.; Engstrom, A.; Persson, B.; Burgess, A. W. *J. Chromatogr.* **1993**, *646*, 159-168.

Chapter 6

Sensitive On-chip Detection of a Protein Biomarker in Human Serum and Plasma Over an Extended Dynamic Range Using Silicon Photonic Microring Resonators and Sub-micron Beads

Notes and Acknowledgements

This chapter has been reproduced from the original paper "Sensitive On-chip Detection of a Protein Biomarker in Human Serum and Plasma Over an Extended Dynamic Range Using Silicon Photonic Microring Resonators and Sub-micron Beads" (Luchansky, M. S.; Washburn, A. L.; McClellan, M. S.; Bailey, R. C. *Lab Chip* **2011**, *11*, 2042–2044). It has been reproduced here with permission from the Royal Society of Chemistry © 2011.

The data collected for these experiments was done as collaborative effort with Matthew Luchansky and Melinda McClellan, and their work is acknowledged. Matthew Luchansky is especially acknowledged for his work in putting together the final versions of the figures in this paper.

We acknowledge support from the NIH Director's New Innovator Award Program, part of the NIH Roadmap for Medical Research, through grant number 1-DP2-OD002190-01, and from the Camille and Henry Dreyfus Foundation. M.S.L and A.L.W were supported via National Science Foundation Graduate Research Fellowship. M.S.L. and M.S.M. were supported via Robert C. and Carolyn J. Springborn Fellowships from UIUC.

This article can be accessed online at: http://dx.doi.org/10.1039/C1LC20231F

6.1 Introduction

Many biosensor development efforts focus almost exclusively on improving detection sensitivity for a particular target analyte. While this is clearly a vital metric, assay dynamic range is also an important attribute that critically influences clinical utility. The dynamic range challenge is even more pronounced for multiplexed analyses, where both intra- and inter-analyte concentrations can vary widely. For example, the cardiovascular risk biomarker C-reactive protein (CRP) can increase by a factor of 10,000 in serum during an acute phase response.[1] Moreover, protein concentrations in human plasma are known to vary over 11 orders of magnitude.[2] Whereas single-analyte assays can incorporate repeated dilutions, multiplexed analyses of antigens that natively vary in magnitude represent a significant analytical challenge.

Recently, chip-integrated, silicon photonic microcavities have been developed for a number of biosensing applications.[3] Importantly, the scalability and multiplexing capability inherent to these semiconductor-based devices make them attractive for many high volume applications, including in vitro clinical diagnostics. Because they are responsive to binding-induced changes to the refractive index (RI) environment near the resonator surface, these sensors are intrinsically label-free. As illustrated in Chapters 3 and 4, microring resonators have been used for protein analysis and detection of analytes in both single[4] and multiplexed[5] formats using an initial slope-based quantitation technique. This approach features a superior linear dynamic range of ~3 orders of magnitude, while maintaining a limit of detection (LOD) comparable to that of a commercial enzyme-linked immunosorbent assay (ELISA). Other work in our group has shown that the incorporation of a secondary antibody recognition event can further lower the limit of detection while also increasing assay specificity in complex sample matrices.[6] However, because of surface-saturation effects, quantitation at higher concentrations is restricted, resulting in a more limited dynamic range similar to that of other sandwich immunoassays.[7]

In this paper, we report the analytical utility of a three-step assay format in which primary, secondary, and bead-enhanced tertiary binding events are observed in series in order to sensitively quantitate the presence of an antigen over a broad (~10^6) dynamic range. As shown in Figure 6.1, the primary and secondary measurements are conducted as described previously.[4, 6] The subsequent tertiary detection event involves the binding of streptavidin (SA)-coated, sub-

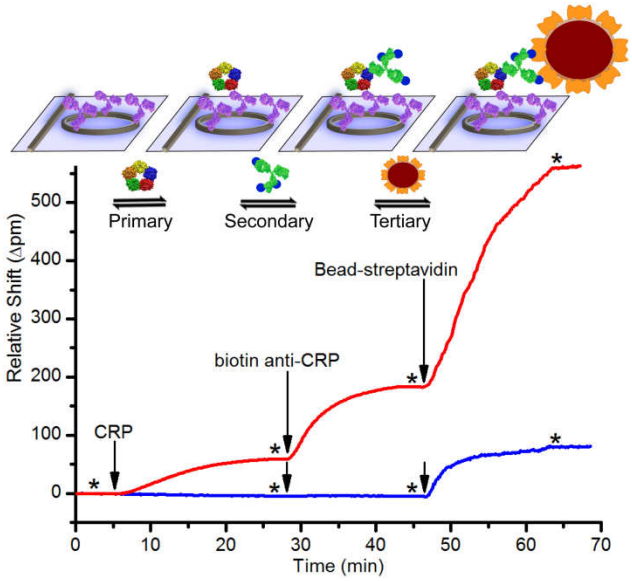

Figure 6.1 Schematic and real-time data plot showing sequential addition of CRP, biotinylated secondary antibody, and SA-functionalized beads. The red trace is 10^{-1} µg/mL CRP. The blue trace is 10^{-3} µg/mL CRP. * indicates buffer rinse, and arrows indicate solution injection.

micron (~100 nm diameter) beads to biotinylated secondary antibodies. Similar to previous reports using nanoparticles,[8-10] carbon nanotubes,[11] and enzymatic amplification[12] to enhance the signal of RI-based sensing devices, our tertiary binding assay lowers the LOD by enhancing the optical signal arising from a single bound antigen. However, more useful here is the integration of a consecutively run assay that includes the real-time observation of all three discrete binding regimes. This methodology broadens the dynamic range to over six orders of magnitude. As a representative analyte that is known to vary over a wide dynamic range in clinical samples,[1] CRP is quantitated via a three-step assay protocol in buffer, human serum, and human plasma.

6.2 Materials and Methods

6.2.1 Materials

3-N-((6-(N'-Isopropylidene-hydrazino))nicotinamide)propyltriethoxysilane (HyNic silane), succinimidyl 6-hydrazinonicotinate acetone hydrazone (S-HyNic), and succinimidyl 4-formyl benzoate (S-4FB) were purchased from Solulink (San Diego, CA). Capture and secondary antibodies to CRP (clones M701289 and clones M701288, respectively) were purchased from Fitzgerald Industries (Concord, MA). Capture (MAB206, clone 6708) and biotinylated secondary (BAF206) antibodies for interleukin-6 were purchased from R&D Systems, Inc (Minneapolis, MN). Recombinant human interleukin-6 and a human CRP ELISA kit (88-7502-28) were purchased from eBioscience (San Diego, CA). NHS-PEG_4-Biotin was purchased from Thermo Scientific and dissolved in DMF to make a 20 mM stock solution. Streptavidin-coated polystyrene/iron oxide beads with a mean diameter of 114 nm were purchased from Ademtech (Pessac, France). Human CRP (95% pure from human blood) was purchased from Meridian Life Science. CRP-depleted processed serum and CRP High Plasma (with a reported CRP content of 69.1 µg/mL based on a Roche Modular immunoassay) were purchased from SunnyLab (Sittingbourne, UK). Pooled normal human serum and single-donor human serum samples #1 and #2 (catalog number IPLA-SER-S, lot numbers K9207 BF 19 and 55-25114 WM 19, respectively) were purchased from Innovative Research (Novi, MI). Fresh single-donor human plasma was collected from a healthy donor under a plan approved by the University of Illinois Institutional Review Board. Zeba spin filter columns and StartingBlock

(PBS) were purchased from Pierce (Rockford, IL). Vivaspin molecular weight cutoff filters (5000 and 50000 kDa) were purchased from GE Healthcare (Waukesha, WI).

The capture anti-CRP antibody was immobilized onto the microring sensors using a DNA-encoding approach.[13, 14] 30-mer DNA strands for the DNA-encoded CRP capture antibody immobilization were synthesized with a C6 spacer and 5′ amination by Integrated DNA Technologies (Coralville, IA). The surface 30-mer sequence was:

5'-AAAAAAAAAAGCCTCATTGAATCATGCCTA-3',

and the complement sequence conjugated to anti-CRP capture antibodies was:

5'-AAAAAAAAAATAGGCATGATTCAATGAGGC-3'.

The 3′- biotinylated 30-mer for the simulated human papillomavirus (HPV) DNA target, simulated HPV DNA 46-mer target, and HPV surface capture strand were also synthesized by Integrated DNA Technologies. The sequences, respectively, were :

5'-CTCTGGATAATAGAGAATGTAAAAAAAAAA-3'
5'-TACATTCTCTATTATCCACACCTGCATTTGCTGCATAAGCACTAGC-3'
5'-AAAAAAAAAGCTAGTGCTTATGCAGCAAAT-3'.

PBS buffer was prepared from Dulbecco's phosphate buffered saline from Sigma Aldrich (St. Louis, MO). PBST buffer consisted of PBS buffer and 0.05% Tween-20. The pH of buffers was adjusted using 1M HCl or 1M NaOH. All other chemicals were obtained from Sigma-Aldrich and used as purchased.

6.2.2 Antibody and DNA Modification

An aldehyde moiety is added to the surface capture DNA strand and its complement by incubation with a 20-fold molar excess of 5 mg/mL S-4FB for 2-3 h at room temperature in 33% DMF in PBS pH 7.4. Excess S-4FB is removed by buffer exchange using a 5-kDa molecular

weight cutoff filter. Capture antibody-HyNic conjugates are prepared by incubating the antibody with a 10-fold excess of 1 mg/mL S-HyNic at room temperature for 2 h. Excess S-HyNic is removed by buffer exchange using Zeba spin filter columns. For biotinylation, 0.5 mg/mL secondary anti-CRP M701288 in PBS pH 7.4 is incubated with a 10-fold molar excess of 20 mM NHS-PEG_4-biotin for 3 h at room temperature. Excess NHS-PEG_4-biotin is removed by buffer exchange using Zeba spin filter columns. Capture antibody- DNA conjugates are prepared by incubating the capture antibody-HyNic conjugate and the 4FB-modified surface DNA strand at a 1:20 protein:DNA ratio overnight at 4°C. The mixture is purified using a Superdex 200 10/300 GL column on an AKTA FPLC, both from GE Healthcare, and fractions containing the antibody-DNA conjugate are concentrated and exchanged into PBS buffer using a 50-kDa molecular weight cutoff filter.

6.2.3 Bead Exchange and Surface Modification

Of critical importance, beads are exchanged into PBST buffer immediately before use to remove free streptavidin via the following procedure. Without doing so, excess free streptavidin rapidly diffuses to the surface and outcompetes the beads for biotin binding sites. To exchange the beads, 30 µL of 5 mg/mL streptavidin-coated beads are diluted to 150 µg/mL with PBST buffer and centrifuged at 10,000 *g* for 4 min. The bead pellet is held at the bottom of the tube using a magnet while the supernatant is removed, leaving about 30 µL of solution. The beads are then resuspended in 1 mL of PBST buffer by pipetting the solution up and down ~50 times with the tube bottom remaining in contact with the magnet. This procedure is repeated for a total of 4 exchanges. Directly before use in the assay, the final bead solution is adjusted to a concentration of 50 µg/mL using the absorbance value at 286 nm as determined by calibration based on direct dilution of non-exchanged beads. For DNA detection, beads are conjugated to a secondary complementary DNA strand. Streptavidin-coated beads are incubated with a large excess of biotinylated DNA for at least 2 h. The excess DNA is removed by buffer exchange according to the previously described method.

6.2.4 Chip Functionalization

Chips are batch-functionalized ex-situ by a spotting method. After a 20-min sonication in ethanol, chips are immersed for 20 s in hot Piranha solution (3:1 H_2SO_4: 30% H_2O_2) [*Caution: Pirahna solution must be handled with care as it can react violently with organic compounds.*], rinsed with water, and dried under a stream of nitrogen. Each chip is then spotted with a 30-µL drop of 1 mg/mL HyNic silane in 95% ethanol and 5% DMF and incubated at room temperature in an enclosed chamber for 30 min. The chip is then rinsed with ethanol and dried. A 0.5-µL drop of 4FB-modified capture DNA strand is then manually pulled across the surface with a 2.5-µL pipette tip. The 24-sensor chips were functionalized with DNA leaving four sensors on each chip unfunctionalized to serve as controls. The chip is then blocked by submersion in StartingBlock at 4ºC for at least 8 h.

6.2.5 CRP Detection Experimental Procedure

The fluidic cell and microfluidic system have been described previously.[4] In these experiments, a Mylar gasket is used to direct flow to two microfluidic channels, each addressing 12 of the 24 active rings, allowing two experiments to be carried out on one chip. A consistent amount of capture antibody is loaded by flowing 10 µg/mL DNA-encoded anti-CRP M701289 at 2 µL/min until the antibody signal reaches ~140 Δpm. To begin the procedure for the analysis of samples, PBST buffer is flowed over the surface to establish a baseline. A 30 µL/min-flow rate is maintained for all assay segments. The sample or standard is introduced and allowed to flow over the surface for 20 min, followed by a buffer rinse. In serum and plasma samples, this rinse is longer (~20 min) than the typical 3 min rinse to allow for desorption of non-specifically bound proteins. The biotinylated secondary antibody is then flowed over the surface for 15 min followed by another short buffer rinse (3-5 min). Finally, streptavidin-coated beads (exchanged immediately before use as described above) are flowed over the surface for 16 min followed by a final buffer rinse. For DNA detection, there is not a third binding step as the secondary detection strand is directly conjugated to the bead.

6.2.6 Instrumental Setup

The microring resonator instrumentation and chips were acquired from Genalyte (San Diego, CA), and have been described in detail in previous publications.[4, 15] Briefly, each chip is fabricated with 32 active microring sensors covered with a perfluoropolymer cladding layer. Eight rings on each chip remain occluded by the polymer layer and serve as thermal controls. Twenty-four active sensors rings have an annular opening etched over the ring to enable exposure to the solution in the microfluidic channel. Each ring resonance is monitored via frequency attenuation in an adjacent linear waveguide. Input and output diffractive grating couplers are located at each end of the waveguide to enable independent determination of the optical cavity spectrum for each microring using a tunable, external cavity diode laser (center frequency: 1560 nm).

6.2.7 Data analysis

Calibration curves for primary binding are generated by determining the initial slope as a function of analyte concentration, as described in Chapter 3. Secondary and tertiary binding calibration curves are generated by plotting the total net relative shift of the secondary and bead binding, respectively. Standard additions were prepared based on an initial estimate of the unspiked concentration in a diluted sample based on comparison to calibration plots generated in buffer. Small increments of a concentrated CRP solution are added to aliquots of diluted sample and then analyzed in the above described manner. Standard addition plots were generated based on primary, secondary, or tertiary response as a function of the concentration of spiked CRP added, and CRP concentrations are determined based on extrapolation of the linear regression fit to the x-intercept. Regression lines for calibration in buffer and standard additions were calculated using linear fitting functions in Origin Pro 8.5 software.

6.3 Results and Discussion

6.3.1 Demonstration of Three-Step Assay

As shown in the red trace in Figure 6.1, the addition of 10^{-1} µg/mL CRP (t = 5 min) resulted in a visible primary binding response. Subsequent addition of biotinylated anti-CRP (t = 28 min) gave a ~3-fold larger response. Finally, addition of 100-nm SA-functionalized beads (t = 46 min) provided an even larger signal enhancement. At this relatively high concentration, secondary and tertiary amplification gave large signals, but they were not required for CRP detection. However, at lower concentrations such as 10^{-3} µg/mL CRP (blue trace in Fig. 1), amplification was necessary. At or below this concentration, no primary binding was detected, and the secondary binding showed ~1 pm resonance wavelength shift. Notably, addition of the beads gave nearly a 100-fold signal enhancement at this low concentration. Negative control experiments, in which biotinylated antibody and SA-beads were flowed over an anti-CRP-functionalized chip without initial CRP incubation, yielded no appreciable signal, as shown in Figure 6.2.

6.3.2 Chip Reproducibility and CRP Calibration Curve

After determining the nature of the three-step signal enhancement process, CRP standards were measured across a 5-order-of-magnitude concentration range using the sequential primary-secondary-tertiary assay protocol. In order to use multiple chips to create a calibration curve, we first had to verify that chip-to-chip responses for a given sample were reproducible. Figure 6.3 shows the response plots from identical analyses on 4 chips (8 fluidic channels) with one ring shown for each channel. Figure 6.3A demonstrates the reproducibility of the measurements at a high concentration of 10^{-1} µg/mL and Figure 6.3B demonstrates reproducibility for a low concentration of 10^{-3} µg /mL.

Statistical results of these comparisons are tabulated in Table 6.1. Average shifts/initial slopes and standard deviations for 10^{-1} µg/mL and 10^{-3} µg /mL CRP are given in Table 6.1A and Table 6.1B, respectively. The ring-to-ring standard deviation is calculated from the standard deviation for all rings (n = 80) on all 4 chips tested, while the channel-to-channel standard deviation is calculated from the standard deviation of the average values for each of 8 channels

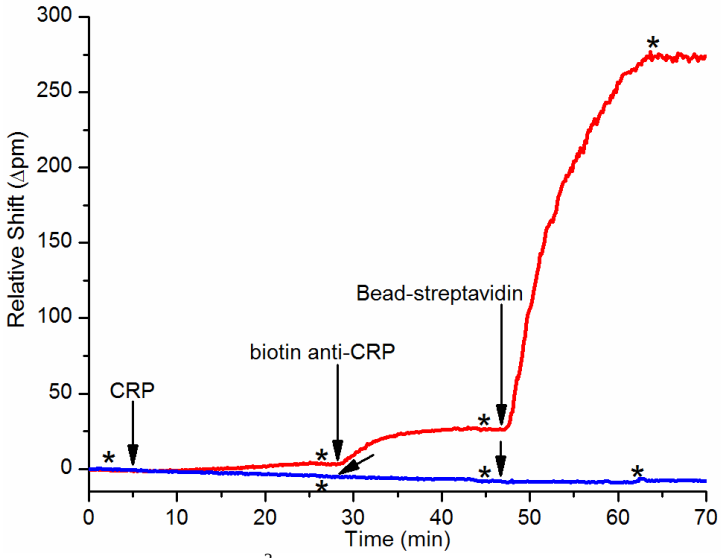

Figure 6.2 Negative control experiment for 10^{-2} µg/mL CRP sandwich assay with bead amplification. The red plot represents the response to 10^{-2} µg/mL CRP (*t* = 5 min) followed by the introduction of 1.6 µg/mL biotin-anti-CRP M701288 (*t* = 28 min) and subsequent signal amplification with 50 µg/mL streptavidin-conjugated beads (*t* = 46 min). The blue plot represents a ring that is first exposed to buffer without any CRP followed by the same secondary antibody and bead solutions. No primary, secondary, or bead signal is observed on rings not exposed to CRP, which demonstrates no appreciable non-specific binding of secondary antibodies or beads. * indicates buffer rinse and the arrows indicate the introduction of the identified solutions at the times noted.

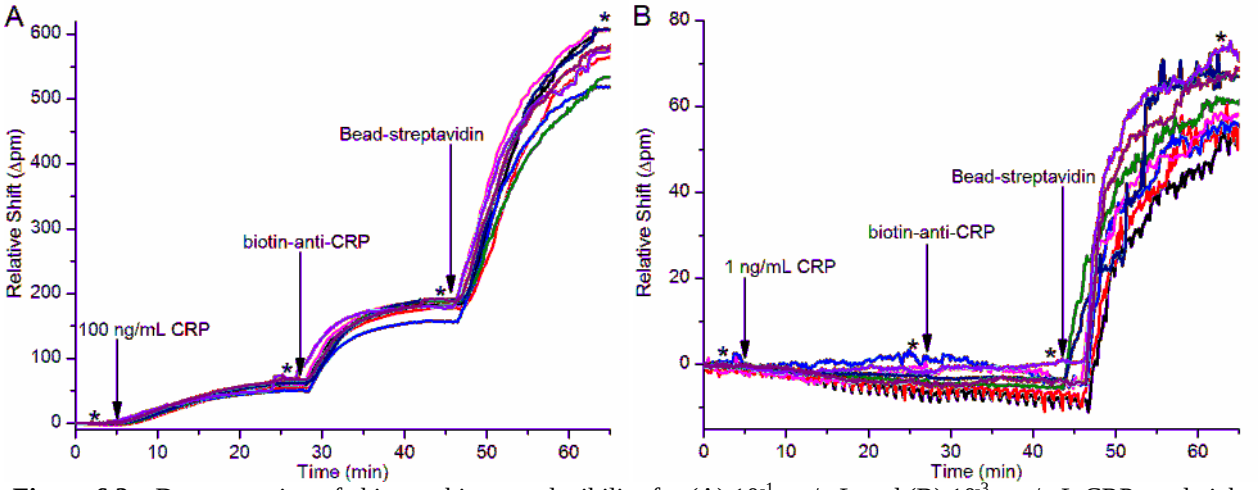

Figure 6.3 Demonstration of chip-to-chip reproducibility for (A) 10^{-1} µg/mL and (B) 10^{-3} µg /mL CRP sandwich assays with subsequent bead-based amplification. Both plots display 8 representative rings, with 1 ring selected from each of 2 channels on a total of 4 chips for each CRP concentration. * indicates buffer rinse and the arrows indicate the introduction of the identified solutions at the times noted. All assays were conducted in freshly degassed 10 mM PBS pH 7.4 + 0.05% Tween-20 with 1.6 µg/mL biotin-anti-CRP M701288 and 50 µg/mL streptavidin-conjugated beads. Statistics for the 10^{-1} µg/mL and 10^{-3} µg /mL reproducibility studies are summarized in Tables 1A and 1B respectively.

Table 6.1 Standard deviations of the variations between sensors and between groups of sensors in a microfluidic channel for CRP analysis at (**A**) 10^{-1} µg/mL and (**B**) 10^{-3} µg /mL.

A	*Initial Primary Slope*	*Secondary Shift*	*Bead Shift*
	Δpm/min	Δpm	Δpm
Average	3.7	117	369
St. Dev. (ring-to-ring)	0.7	14	47
St. Dev. (channel-to-channel)	0.3	8	33

B	*Initial Primary Slope*	*Secondary Shift*	*Bead Shift*
	Δpm/min	Δpm	Δpm
Average	-	0.9	73
St. Dev. (ring-to-ring)	-	1.5	15
St. Dev. (channel-to-channel)	-	1.0	8

(2 microfluidic channels/chip). In each case, the ring-to-ring variability exceeds the channel-to-channel variability, suggesting that the use of multiple chips for calibrations and quantitative analyses is satisfactory. It is also worth noting that the 0.9 ± 1.5 pm secondary shift for 10^{-3} µg /mL CRP represents a concentration on the lower boundary of what can be seen with a simple CRP sandwich assay. Although difficult to observe with secondary binding, tertiary binding creates an easily measurable response (73 ± 15 pm). Thus, in addition to enabling detection at previously impossible levels, beads also are important for amplifying small secondary signals.

After determining chip-to-chip reproducibility, we then detected CRP across a wide range of concentrations to create the calibration curve shown in Figure 6.4. In this figure, the response curves from the primary, secondary, and tertiary binding assays overlap, allowing continuous CRP calibration over a broad dynamic range (10^{-4} µg/mL to 10 µg/mL). The initial slope of primary binding (black squares) is important because, at high concentrations, the surface is nearly saturated. Thus, it is impossible to distinguish between high concentrations except by the rate at which they approach saturation.[4] Using initial slopes, it is possible to quantify concentrations from 10^{-2} to >10 µg/mL in buffer. The dynamic range is extended (10^{-3} to $>10^{-1}$ µg/mL) by measuring the relative shift in resonance wavelength following addition of secondary antibody (red circles) and further expanded down to $<10^{-4}$ µg/mL though the use of SA-bead enhancement (blue triangles). Using the bead-based enhancement, the overall assay LOD is ~3 × 10^{-5} µg/mL (~200 fM).

The dynamic range of each step of the three-part analysis method has a region of overlap with one of the other steps (Figure 6.4), providing the opportunity for confirmation of the measurement. For example, 10^{-3} µg/mL CRP is quantifiable by secondary detection, but tertiary amplification significantly increases the measurement precision. As suggested by the results in Table 6.1.

6.3.3 Detection of CRP in Plasma and Serum

Following assay calibration, the same three-step detection protocol was applied to the quantitation of CRP in human plasma and serum samples. Because the expected range of concentrations of CRP in human blood is from 10^{-1} µg/mL to 10^{3} µg/mL, each sample was subjected to the same 1:1000 dilution into buffer, bringing concentrations into the range that

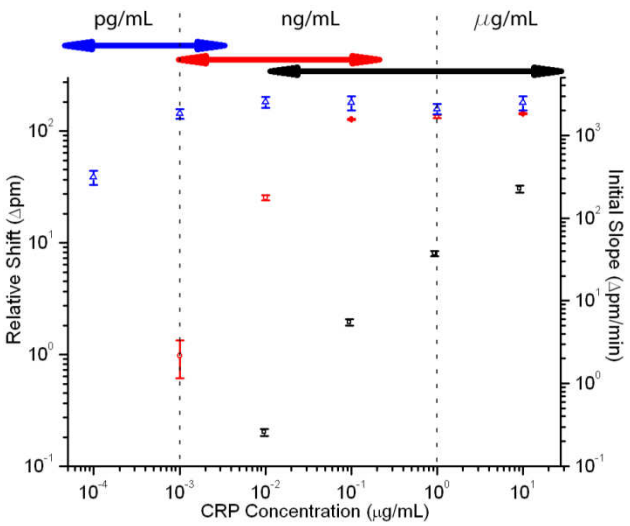

Figure 6.4 Log-log calibration plot showing the response of the microring resonators to varying concentrations of CRP using the three-step assay. Black squares indicate the initial slope of the primary binding (right axis), red circles indicate secondary antibody shift, and blue triangles indicate bead shift (left axis). Error bars represent 95% CI for n=17-47 rings for each concentration. Arrows at top represent overlap of dynamic ranges for each assay portion.

could most accurately be quantified. This uniform dilution, as opposed to repeated dilutions, also helped reduce non-specific adsorption of blood proteins and lowered the required sample volumes to less than ten microliters, making the assay amenable to fingerprick sampling.

For the purposes of quantitation we utilized a standard addition method as it is amenable to the complex and variable clinical sample matrices.[16] In this method, the diluted serum or plasma was first analysed via the three-step assay, and the response was compared to the calibration curve (Figure 6.4) to roughly estimate the CRP concentration range. Three appropriate samples with increasing standard additions were then successively analysed, and the precise CRP concentration was determined via extrapolation. The wide variation in native CRP levels required user input into the standard addition procedure, as opposed to simply adding uniform amounts of standard. However, the overall methodology is amenable to automation; for example, an analytical system pre-programmed with the calibration information could utilize integrated microfluidics to create the appropriate standard additions on demand.

Figure 6.5 shows the standard addition plots generated for each sample. Figure 6.6 shows the results of these serum/plasma analyses. The colours in the graph indicate the method used to quantify the CRP concentration. The black bar indicates that a commercially obtained pooled plasma sample with elevated CRP was quantified using the primary binding response and found to have a CRP concentration of 57.5 ± 3.3 µg/mL. This value obtained on the microring resonator platform agreed reasonably well with the supplier's provided value of 69.1 µg/mL. The red bars indicate secondary binding-based detection, which was used to quantitate the CRP values in the pooled-donor normal serum, single-donor serum #2, and single-donor plasma. The blue bars indicate quantitation using the tertiary bead binding, which was necessary to detect CRP within single-donor serum #1 as well as a commercially-available CRP-depleted serum sample (in which CRP had been removed by the vendor). Each of the samples analysed, with the exception of the CRP-elevated pooled plasma, had CRP levels less than 1 µg/mL, placing those donors in the low-risk range for cardiovascular disease.[1] Interestingly, for the CRP-depleted sample, analysis of a 1:100 dilution revealed CRP levels at 3×10^{-5} µg/mL. While this concentration is far below what would typically be found in human serum, it is noteworthy that this is similar to the lowest levels of CRP present in saliva.[17] This means that the three-step assay format on the silicon photonic-based platform is amenable to quantifying CRP in all clinically-relevant sample matrices.

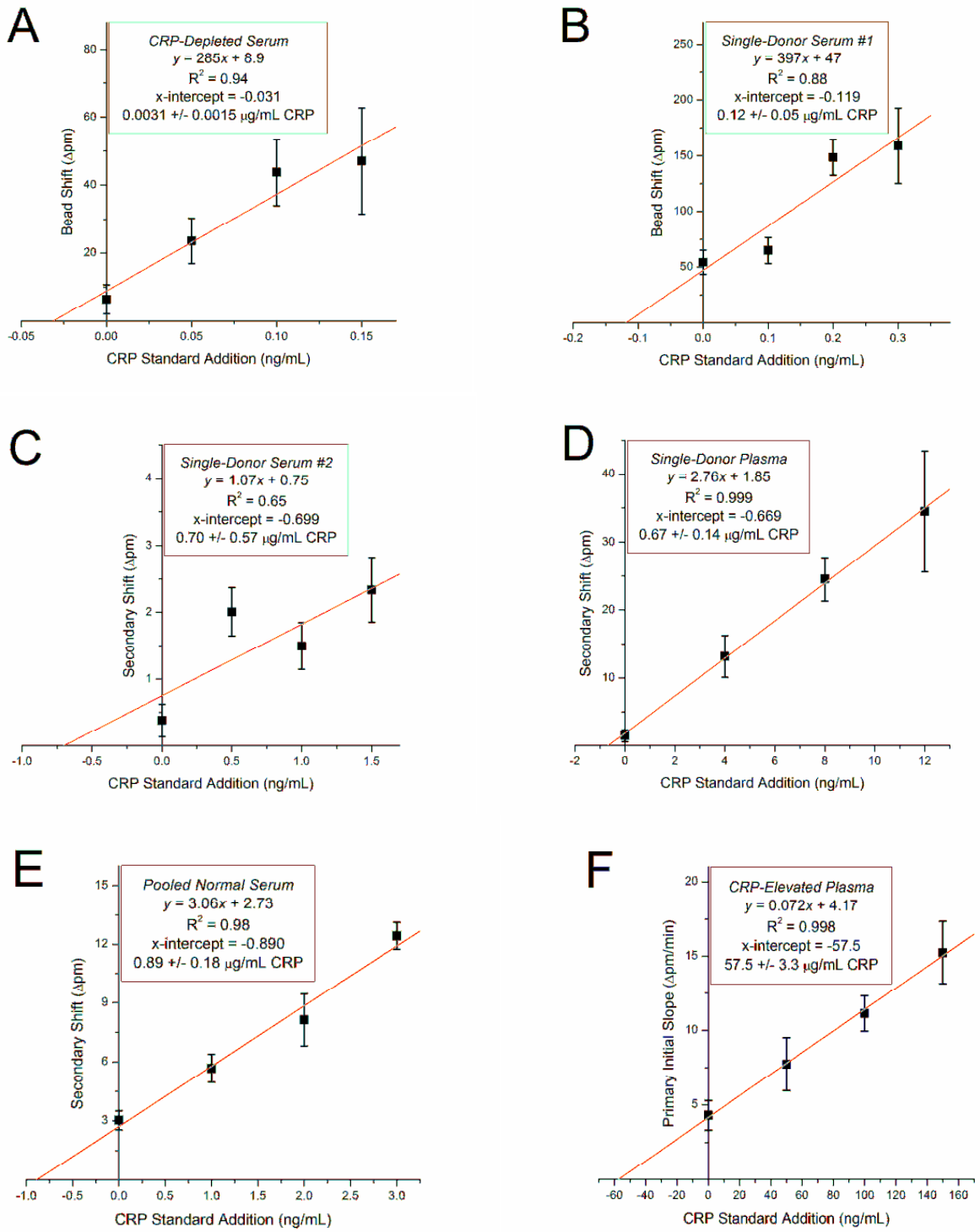

Figure 6.5 Standard addition plots used to determine CRP concentrations in 6 human serum and plasma samples quantified in Figure 6.6. Since CRP levels vary over a wide dynamic range, quantitation was performed based on bead shift (**A**, **B**), secondary shift (**C**, **D**, **E**), or primary initial slope (**F**). Each plot displays the shift or slope data for an unspiked sample dilution plus three standard additions of CRP determined by the magnitude of the unspiked sample response. The sample identity, fitting equation, quality of fit, x-intercept, and observed CRP concentration are presented for each standard addition experiment shown above.

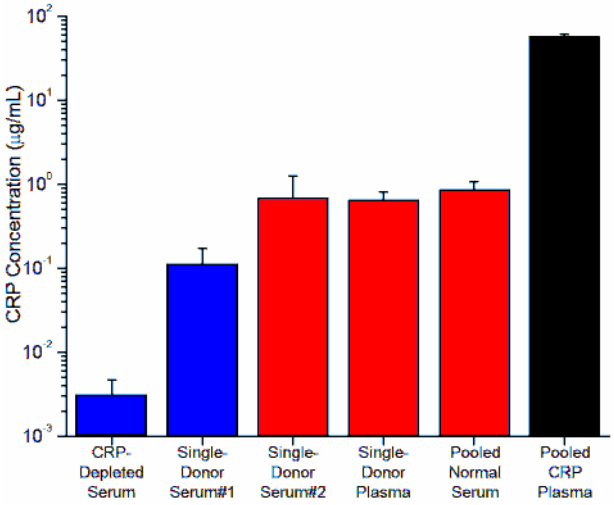

Figure 6.6 Detection of CRP in human serum and plasma samples. All samples are diluted 1:1000 in buffer except for the CRP-depleted serum, which was diluted 1:100. Error bars represent the error in the x-intercept determination used in the standard addition analysis.

Table 6.2 Comparison of CRP levels measured by ring resonators with those determined based on a commercial CRP ELISA.

	CRP Concentration (µg/mL)	
	Ring Resonator Array	*CRP ELISA*
CRP-Depleted Serum	0.0031 ± 0.0015	-
Single-Donor Serum #1	0.12 ± 0.05	0.19 ± 0.08
Single-Donor Serum #2	0.70 ± 0.57	0.39 ± 0.08
Single-Donor Plasma	0.67 ± 0.14	2.05 ± 0.22
Pooled Normal Serum	0.89 ± 0.18	1.45 ± 0.10
Pooled CRP-Elevated Plasma	58 ± 3	105 ± 11

In addition to microring resonator analysis, a commercial enzyme-linked immunosorbent assay (ELISA) was performed for comparison with the results for the six human serum and plasma samples depicted graphically in Figure 6.6. Results of this comparison are given in Table 6.2. In this table, errors for the ring resonator array data represent the error in the x-intercept determination used in the standard addition assays (as described above). ELISA errors are the standard deviation of triplicate assays run according to the manufacturer's protocol. All ELISA values were measured from samples that were diluted to be within the range of the assay, with a 1:1000 dilution proving optimal for all but the CRP-elevated plasma which required a 1:40000 dilution. ELISA failed to detect CRP in the CRP-depleted serum at any dilution tested (1:100, 1:1000, 1:4000). While ring resonator analysis was in strong agreement with ELISA for most of the samples tested, some varied by as much as a factor of 2-3. This variation is typical of what is observed when comparing a variety of immunoassays, especially considering different dilution factors. Prior analyses of CRP samples by Khuseyinova *et al.* and Clarke *et al.* that each compared separate immunoassay methodologies showed a similar degree of agreement between methods, with most values in strong agreement and some varying by as much as a factor of 3-4.[18, 19] These variations also tend to be more pronounced at higher concentrations, such as the pooled CRP-elevated plasma sample, where additional dilution or use of calibration curve extremes are necessary but introduce greater error due to pipetting, regression, or signal saturation.

In the course of our studies, we observed that several of the serum and plasma samples gave abnormally large signals for primary binding to microrings functionalized with the capture anti-CRP antibody, but a much smaller secondary binding response. These interactions, which we attribute to cross-reactivity between the primary antibody and some unknown component, highlight the fact that sample-to-sample heterogeneity can greatly complicate analysis in clinical samples. In the case of the pooled plasma with elevated CRP, the primary binding signal was much larger than any of the off-target responses, and thus it did not interfere with primary response-based quantitation. However, for the single-donor plasma and serum samples, as well as the pooled normal serum, the primary off-target signal indicated abnormally high CRP content. Fortunately, the proportionally smaller secondary binding response increased the specificity of the assay, giving more reliable levels of CRP. Although some of the complications associated with clinical samples might be reduced by employing alternative antibodies or improved surface treatments, cross-reactivity and non-specific interactions are particularly difficult to completely

avoid for multiplexed assays from within complex sample matrices, underscoring the utility of this three-step measurement format that allows analytes to be measured at multiple levels, increasing both the specificity of the assay and reducing false positive responses.

6.3.4 Detection of DNA and IL-6 with Bead Amplification

As a final demonstration of our signal amplification strategy, we not only measure CRP concentrations, but we also demonstrate that we can detect DNA strands as well as the cytokine interleukin-6 (IL-6) using the bead amplification protocol. Figure 6.7A shows the detection of a 46-mer DNA strand relevant to the detection of the human papillomavirus (HPV). This ssDNA target was measured at four concentrations: 10 nM, 2 nM, 0.4 nM, and 0.16 nM. Each concentration is undetectable via primary binding, but addition of beads conjugated to a 30-mer DNA probe that is complementary to a portion of the HPV target, a measurable signal is given.

IL-6 was detected in a similar manner as CRP using the sandwich assay detection format with a biotinylated secondary antibody. Samples at concentrations of 10 ng/mL and 0.1 ng/mL are measured using the bead-binding amplification. At the 0.1 ng/mL level, signal is only detected by the beads binding to the biotinylated secondary antibody. Overall, these two examples demonstrate the applicability of the signal amplification technique to a variety of analytes.

6.4 Conclusions

This chapter demonstrates a three-step immunoassay on a scalable silicon photonic biosensing platform that enables a protein antigen to be detected over six orders of magnitude of concentration in complex, clinically-relevant sample matrices. While primary binding allows detection at higher concentrations, subsequent secondary and tertiary binding events significantly lower the LOD. The secondary and tertiary binding also increases the specificity of the assay by requiring additional target-specific recognition, allowing discrimination against non-specific interferants. Using this approach in a standard addition format, we determined the concentration of CRP in both human serum and plasma across a broad dynamic range while avoiding the need

for multiple serial dilutions. This methodology, which is facilitated by a real-time and modularly multiplexable sensor technology, is applicable beyond the detection of CRP and can be applied to other analytes. The generality of this technique should make it useful in multiplexed analyses where analytes may differ in concentration by orders of magnitude.

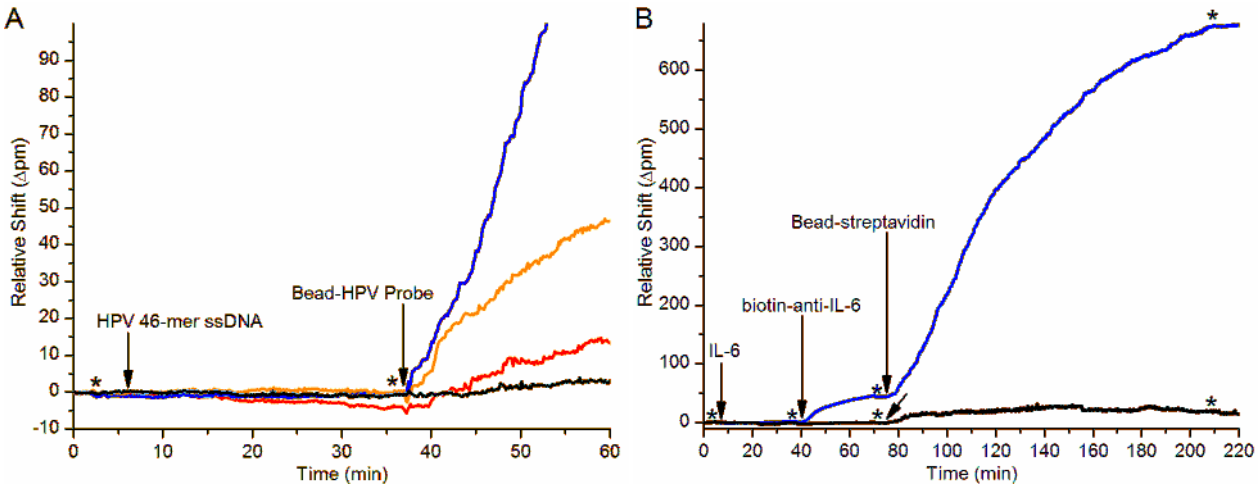

Figure 6.7 Bead-based signal amplification universally augments ring resonator signals in assays designed for the detection of (A) a 46-mer human papillomavirus (HPV) ssDNA target and (B) the cytokine interleukin-6 (IL-6). In (A), 4 concentrations of HPV DNA prepared by serial dilution [10 nM (blue), 2 nM (orange), 0.4 nM (red), 0.16 nM (black)] are each undetectable based on primary binding (t = 6-36 min) to rings functionalized with a 30-mer probe complementary to the HPV target. Upon the addition of beads conjugated with a separate 30-mer DNA probe complementary to the remaining portion of the HPV 46-mer at t = 37 min, all 4 concentrations can be detected in a concentration-dependent manner. HPV DNA assays were conducted in freshly degassed 10 mM PBS pH 7.4 + 0.05% Tween-20 with 20 µg/mL HPV probe-conjugated beads. In (B), 10 ng/mL (blue) and 0.1 ng/mL (black) IL-6 are detected using bead-based amplification of a sandwich immunoassay. The secondary shift for 10 ng/mL IL-6 is amplified ~12x through the use of beads. However, the lower concentration of 0.1 ng/mL IL-6 (5 pM) is only detectable through the use of bead-based amplification to amplify the secondary signal. IL-6 assays were conducted in 10 mM PBS pH 7.4 + 0.1 mg/mL BSA with 1 µg/mL biotin anti-IL-6 BAF206 and 50 µg/mL streptavidin-conjugated beads. * indicates buffer rinse and arrows indicate the introduction of the identified solutions at the times noted.

6.5 References

(1) McDonnell, B.; Hearty, S.; Leonard, P.; O'Kennedy, R. *Clin. Biochem.* **2009**, *42*, 549-561.

(2) Anderson, N. L.; Anderson, N. G. *Mol. Cell. Proteomics* **2002**, *1*, 845-867.

(3) Washburn, A. L.; Bailey, R. C. *Analyst* **2011**, *136*, 227-236.

(4) Washburn, A. L.; Gunn, L. C.; Bailey, R. C. *Anal. Chem.* **2009**, *81*, 9499-9506.

(5) Washburn, A. L.; Luchansky, M. S.; Bowman, A. L.; Bailey, R. C. *Anal. Chem.* **2010**, *82*, 69-72.

(6) Luchansky, M. S.; Bailey, R. C. *Anal. Chem.* **2010**, *82*, 1975-1981.

(7) Law, B., Ed. *Immunoassay: A Practical Guide*; Taylor & Francis: London, 1996.

(8) He, L.; Musick, M. D.; Nicewarner, S. R.; Salinas, F. G.; Benkovic, S. J.; Natan, M. J.; Keating, C. D. *J. Am. Chem. Soc.* **2000**, *122*, 9071-9077.

(9) Kim, S.; Lee, J.; Lee, S. J.; Lee, H. J. *Talanta* **2010**, *81*, 1755-1759.

(10) Sim, H. R.; Wark, A. W.; Lee, H. J. *Analyst* **2010**, *135*, 2528-2532.

(11) Lee, E. G.; Park, K. M.; Jeong, J. Y.; Lee, S. H.; Baek, J. E.; Lee, H. W.; Jung, J. K.; Chung, B. H. *Anal. Biochem.* **2011**, *408*, 206-211.

(12) Li, Y.; Lee, H. J.; Corn, R. M. *Anal. Chem.* **2007**, *79*, 1082-1088.

(13) Bailey, R. C.; Kwong, G. A.; Radu, C. G.; Witte, O. N.; Heath, J. R. *J. Am. Chem. Soc.* **2007**, *129*, 1959-1967.

(14) Washburn, A. L.; Gomez, J.; Bailey, R. C. *Anal. Chem.* **2011**, *83*, 3572-3580.

(15) Iqbal, M.; Gleeson, M. A.; Spaugh, B.; Tybor, F.; Gunn, W. G.; Hochberg, M.; Baehr-Jones, T.; Bailey, R. C.; Gunn, L. C. *IEEE J. Sel. Top. Quantum Electron* **2010**, *16*, 654-661.

(16) Harris, D. C. *Quantitative Chemical Analysis*, 5th ed.; W. H. Freeman and Company: New York, 1999.

(17) Dillon, M. C.; Opris, D. C.; Kopanczyk, R.; Lickliter, J.; Cornwell, H. N.; Bridges, E. G.; Nazar, A. M.; Bridges, K. G. *Biomarker Insights* **2010**, *5*, 57-61.

(18) Khuseyinova, N.; Imhof, A.; Trischler, G.; Rothenbacher, D.; Hutchinson, W. L.; Pepys, M. B.; Koenig, W. *Clin. Chem.* **2003**, *49*, 1691-1695.

(19) Clarke, J. L.; Anderson, J. L.; Carlquist, J. F.; Roberts, R. F.; Horne, B. D.; Bair, T. L.; Kolek, M. J.; Mower, C. P.; Crane, A. M.; Roberts, W. L.; Muhlestein, J. B. *Am. J. Cardiol.* **2005**, *95*, 155-158.

Chapter 7

Creation of a Multiplex Protein Biomarker Panel and Detection of Eight Protein Cancer Biomarkers in Cancer Patient Blood Serum Using Silicon Photonic Microring Resonators

Notes and Acknowledgements

This work was funded by the NIH Director's New Innovator Award Program, part of the NIH Roadmap for Medical Research, through grant number 1-DP2-OD002190-01, and by the Camille and Henry Dreyfus Foundation. A.L.W. was supported via a National Science Foundation Graduate Research Fellowship as well as a Division of Analytical Chemistry Summer Graduate Research Fellowship funded by the Society for Analytical Chemists of Pittsburgh. The assistance of Kim Lenkeit, Winnie Shia, Matthew Luchansky, and Kiarah Lee was crucial to the collection of data and the development of this work, and their help is gratefully acknowledged.

7.1 Introduction

In recent years, the development of biomarker panels and proteomic profiles for diagnostic purposes has been viewed as a promising means to diagnose and treat cancer patients earlier and more accurately.[1, 2] Unfortunately, developing validated biomarkers that can be incorporated into panels that meet the rigorous requirements for a clinical diagnostic have faced several challenges.[3, 4] Some of the challenges to developing validated biomarker diagnostics for clinical use include avoiding bias in sample collection and storage methods, avoiding bioinformatics artifacts, and, perhaps most importantly, developing methods in a laboratory that can be reproduced in a clinical setting—a key to success in clinical trials.

To develop robust, reproducible tools for clinical diagnostics, it is important to understand the strengths and shortcomings of current methods. At this time, multiplex diagnostics have generally fallen into two classes of analysis: mass spectrometry-related analysis and immunoassay-derived analysis.[5] Mass spectrometry has the advantage that proteomic analysis has the potential to reveal the presence of thousands of proteins in a single sample, especially when combined with preparatory steps such as chromatography or sample digestion. Unfortunately, the variability in preparation steps and instrumentation between laboratories adversely affects the reproducibility of mass spectrometric methods. Conversely, immunoassays utilize specific antibody capture agents and are typically designed to analyze one analyte per capture agent. Although this practically limits the number of analytes that can be measured in a given multiplexed assay, the well-behaved specificity of the capture agents helps immunoassays perform in a more robust manner as compared to mass spectrometric analyses. As a result, immunoassays typically require simpler procedures—dilution often being the only preparative step—and are typically more reproducible and quantitative, even between different laboratories. Thus, although mass spectrometry will continue to play a significant role in the discovery and analysis of protein biomarkers, immunoassays are a more likely candidate for the development of robust, widespread diagnostics that can accurately quantitate biomarkers in human samples in a multiplexed fashion. As a result, our research is focusing on the development of an antibody-based multiplex analysis chip that can measure biomarkers from human serum samples in a robust manner.

For multiplexed immunoassays, the current state of the art typically relies upon planar microarrays or multiplexed bead-based assays for measuring concentrations of biomarkers in human serum samples.[6] Although these techniques are well established and can deliver promising results, they typically rely on a signal that is generated at the end of multiple binding steps. For example, a standard bead-based detection format would involve immobilized antibodies binding to antigens of interest followed by binding of secondary antibodies that are attached to some sort of signal generating molecule (enzyme, fluorophore, etc.).[6, 7] In contrast, with refractive index-based sensors, such as microring resonators, it is possible to gain information from each step of the process—primary antigen binding, secondary antibody binding, and tertiary signal amplification.[8] This additional information can not only improve the dynamic range of an assay and provide additional information in a multiplexed analysis, but it also makes it possible to more rapidly develop and interpret reliable immunoassays. One of the challenges with a multiplexed immunoassay is obtaining appropriate capture agents for a given analyte and then avoiding interferences between different capture agents. By being able to observe primary binding of antigen in real time as well as secondary antibody binding, it is possible to gain the information necessary to rapidly develop an assay that will be limited in cross reactivity, or at least in which any cross reactivity will be well understood and characterized.

Our previous work developing microring resonators has shown that multiplexed microring resonator chips can be used to rapidly screen antibodies for binding affinities and for sandwich pairs.[9] Additionally, we have shown that microrings can be utilized for multiplex detection of cancer biomarkers[10] and that we can sensitively detect a single biomarker using a signal amplification scheme.[8] In this paper, we combine these capabilities to create a multiplexed cancer biomarker chip that can detect eight different cancer biomarkers in human serum using a signal amplification method to improve the limit of detection.

For our cancer biomarker panel we selected: α-fetoprotein (AFP), for liver and germ cell cancer;[11] carcinoembryonic antigen (CEA), for colorectal and pancreatic cancer;[12-15] cancer antigen-125 (CA-125), for ovarian cancer;[11, 16] osteopontin, for ovarian cancer;[16] cancer antigen 19-9 (CA19-9), for pancreatic, colorectal, or ovarian cancer; [11, 17] cancer antigen 15-3 (CA15-3), for breast cancer;[11] prostate specific antigen (PSA), for prostate cancer;[18] and activated leukocyte cell adhesion molecule (ALCAM), for breast cancer.[19] In selecting which biomarkers to use for our test panel, we included six very common biomarkers (CEA, CA-125, CA15-3, AFP, PSA,

and CA19-9), five of which are FDA-approved biomarkers[15] (CEA, CA-125, CA15-3, AFP, and PSA), and two less common biomarkers (osteopontin and ALCAM). Our choices were made to facilitate a panel that covers a wide variety of cancers as well as those that would be enabled by a good selection of commercially available antibodies. This selection is ideal for demonstrating the potential to create a robust diagnostic panel that can be utilized for analyzing clinical samples. Although future developments would probably narrow down the selection of biomarkers to several pertinent biomarkers for a particular cancer type, this work nonetheless demonstrates the utility of microring resonators in the creation and implementation of multiplexed biomarker panels.

At time of publishing, this chapter's work is only partially completed. In this chapter, we demonstrate the creation of an 8-plex biomarker panel, the characterization of the signal amplification method, and an initial trial with several human serum samples. In the near future, this work will continue to advance by developing a method to quantify serum patient samples, as well as looking at statistical methods for analyzing and categorizing patient samples.

7.2 Materials and Methods

7.2.1 Materials

Succinimidyl 4-formylbenzoate (S-4FB), succinimidyl 6-hydrazinonicotinamide acetone hydrazone (S-HyNic), and 3-N-((6-(N'-Isopropylidene-hydrazino))nicotinamide)propyltriethy-oxysilane (HyNic Silane) were purchased from SoluLink (San Diego, CA). Custom DNA oligonucleotides were synthesized by Integrated DNA Technologies (Coralville, IA). A list of capture and detection antibodies used in these experiments is given in Table 7.1. NHS-PEG_4-Biotin, Zeba spin filters, and Starting Block were purchased from Pierce (Rockford, IL). NHS-PEG_4-Biotin was dissolved in DMF to make a 20 mM stock solution. Human serum samples from cancer patients were purchased from Innovative Research, Inc. (Novi, MI) and Asterand, Inc. (Detroit, MI). Fresh single-donor human plasma was obtained from a healthy donor under a plan approved by the University of Illinois Institutional Review Board. Vivaspin molecular weight cutoff filters (50,000 and 5,000 Da MWCO), were obtained from GE Healthcare (Waukesha, WI). Alternately, molecular weight cut-off filters (30,000 and 3,000 Da MWCO) were obtained from VWR (Radnor, PA). Anti-biotin (phycoerythrin) and anti-phycoerythrin

Table 7.1 List of antigens and antibodies used for eight-plex experiments, company source, product number and antibody clone (for monoclonal antibodies)

Antibody / Antigen Type		Source*	Product Number	Antibody Clone
AFP	**Antigen**	Meridian	A81510H	
	Capture	Meridian	MAM01-301	057-11301
	Detection	Meridian	M01254M	B491M
ALCAM	**Antigen**	R&D Systems	656-AL	
	Capture	R&D Systems	MAB656	105901
	Detection	R&D Systems	BAF656	Polyclonal
CA 125	**Antigen**	Fitzgerald	30-AC21	
	Capture	Life Span	LS-C84288 / 28658	M002201
	Detection	Meridian	10-C02F	M002203
CA 15-3	**Antigen**	Meridian	A32000H	
	Capture	Fitzgerald	10-C03E	M002204
	Detection	Fitzgerald	10-C03F	M002208
CA 19-9	**Antigen**	Fitzgerald	30AC14	
	Capture	Fitzgerald	10C04C	M8073021
	Detection	Meridian	M37301M	241
CEA	**Antigen**	Fitzgerald	30-AC32	
	Capture	Meridian	MAM02-009	057-10009
	Detection	Meridian	MAM02-008	057-10008
Osteopontin	**Antigen**	Fitzgerald	30RA0008	
	Capture	Meridian	M66102M	2C5
	Detection	Meridian	H01278M	B697M
PSA	**Antigen**	Fitzgerald	30R-AP019	
	Capture	Meridian	M66279M	B731M
	Detection	Meridian	M86506M	5A6

*Sources full names and locations:

Meridian Life Science, Saco, ME

R&D Systems, Minneapolis, MN

Fitzgerald Industries International, Concord, MA

Life Span Biosciences, Seattle WA

(biotin) were obtained from eBioscience (San Diego, CA). All antigens and antibodies (capture and detection) purchased and used for eight-plex experiments are listed in Table 7.1. Streptavidin-coated polystyrene/iron oxide beads with a mean diameter of 114 nm were purchased from Ademtech (Pessac, France). Phosphate buffered saline (PBS), with a standard 10 mM phosphate ion concentration, was reconstituted from Dulbecco's phosphate buffered saline packets purchased from Sigma-Aldrich (St. Louis, MO). All other chemicals were obtained from Sigma-Aldrich and used as received.

All buffers were made with purified water (ELGA PURELAB filtration system; Lane End, UK), and the pH was adjusted as necessary with 1 M HCl or 1 M NaOH. For NHS-ester chemistry, PBS buffer with 100 mM phosphate (100 mM PBS) was used. This was made with 150 mM NaCl, 22.5 mM monobasic sodium phosphate, and 77.7 mM dibasic sodium phosphate and then pH-adjusted to either pH 7.4 or pH 6.0. PBS with 0.05% Tween-20 (PBST) was made by adding Tween-20 to standard PBS buffer (Dulbecco's formulation). PBST with Starting Block (PBST-SB) was made by adding 1% Starting Block to PBST buffer and then adding 0.01% sodium azide as a preservative. All solutions were degassed under vacuum sonication before being flowed across the sensor surface.

7.2.2 Instrumental Setup and Microchip Design

The sensor chips and microring resonator measurement system was acquired from Genalyte, Inc. (San Diego, CA). For initial results and testing, we utilized Generation 1 instrumentation and microring resonator chips as previously described.[20] These chips were 6 × 6 mm microchips with 32 microring sensors, 8 of which are thermal controls. All measurements for these experiments were made with the sensor chips loaded into a custom cell with microfluidic flow channels defined by a 0.007-inch thick Mylar gasket with a U-shaped channel 750 µm wide as previously described.[21] Solution was flowed through the chips via a Harvard Apparatus syringe pump (Holliston, MA).

7.2.3 Silane Functionalization

Microring array substrates were first cleaned with piranha solution[22] (3:1 H_2SO_4:30% H_2O_2) for 30 seconds followed by rinsing with water and N_2 drying. To introduce reactive functional groups, all substrates had 20 µL of a 1 mg/mL solution of HyNic Silane (20 mg/mL HyNic Silane in DMF stock solution diluted to 1 mg/mL with ethanol) added to the chip surface for ~30 minutes, followed by rinsing with ethanol and then sonicating in ethanol for ~30 minutes. Chips were then dried with N_2.

7.2.4 Oligonucleotide Functionalization

Oligonucleotide sequences, which were designed to minimize cross-reactivity between DNA probes, were previously used in creating DNA-antibody conjugates.[9, 23] The exact sequences, named B, B′, C, C′, D, D′, F, F′, J, J′, K, K′, L, L′, and M, M′, (where a prime symbol indicates a complementary sequence), are listed in Table 7.2. All oligonucleotides were synthesized with a 5′ amino terminal group to facilitate additional chemical reactivity. All oligonucleotides were functionalized with S-4FB according to manufacturer (SoluLink) instructions. Briefly, oligonucleotides were buffer exchanged to 100 mM PBS pH 7.4 using 5 kDa MWCO filters and then a 20-fold molar excess of S-4FB in DMF was added. Solutions were allowed to react overnight at room temperature and then were buffer exchanged into 100 mM PBS pH 6.0 using 5 kDa MWCO filters. Anomalously, Strand C had a tendancy to permeate the 5 kDa MWCO filters whereas the other strands showed no such permeation. Using a 3 kDa MWCO filter helped reduce loss of Strand C in the buffer exchanges.

7.2.5 DNA-Antibody Conjugate Synthesis

To create DNA-antibody conjugates, antibodies were functionalized with S-HyNic as previously demonstrated.[9] Briefly, S-HyNic in DMF was added in 20- to 30-fold molar excess to ~1 mg/mL antibody that had previously been buffer exchanged into 100 mM PBS pH 7.4 with a Zeba spin filter and reacted for at least two hours at room temperature. The antibody was then exchanged into 100 mM PBS pH 6.0 with a Zeba spin filter. The 4FB-modified DNA was then

Table 7.2 List of DNA oligonucleotide sequences used. All sequences have a 5′ terminal amino group attached via a 6-carbon chain (5AmMC6 from IDT)

Name	Sequence (5′ to 3′)
B	AAA AAA AAA AGC CTC ATT GAA TCA TGC CTA
B′	AAA AAA AAA ATA GGC ATG ATT CAA TGA GGC
C	AAA AAA AAA AGC ACT CGT CTA CTA TCG CTA
C′	AAA AAA AAA ATA GCG ATA GTA GAC GAG TGC
D	AAA AAA AAA AAT GGT CGA GAT GTC AGA GTA
D′	AAA AAA AAA ATA CTC TGA CAT CTC GAC CAT
F	AAA AAA AAA AAT CAG GTA AGG TTC ACG GTA
F′	AAA AAA AAA ATA CCG TGA ACC TTA CCT GAT
J	AAA AAA AAA ATC TTC TAG TTG TCG AGC AGG
J′	AAA AAA AAA ACC TGC TCG ACA ACT AGA AGA
K	AAA AAA AAA ATA ATC TAA TTC TGG TCG CGG
K′	AAA AAA AAA ACC GCG ACC AGA ATT AGA TTA
L	AAA AAA AAA AGT GAT TAA GTC TGC TTC GGC
L′	AAA AAA AAA AGC CGA AGC AGA CTT AAT CAC
M	AAA AAA AAA AGT CGA GGA TTC TGA ACC TGT
M′	AAA AAA AAA AAC AGG TTC AGA ATC CTC GAC

added in >10-fold molar excess to the HyNic-modified antibody solution and allowed to react overnight at 4 °C. DNA-antibody conjugates were then purified away from the excess DNA using a Superdex 200 10/300 GL column on an AKTA FPLC, both from GE Healthcare (Waukesha, WI). The separation was performed at 4 °C with a PBS isocratic elution. The collected fractions were concentrated with either 30 or 50 kDa MWCO filters (with equivalent results) to yield purified solutions of DNA-antibody conjugates. The final conjugate concentration was determined by measuring the differential absorption at 260 versus 280 nm, corresponding to the DNA and IgG, respectively, using a NanoDrop UV-Vis absorbance system (ThermoFisher Scientific, Wilmington, DE). The following conjugates were synthesized using the capture antibodies listed in Table 7.1: B′-anti-AFP, C′-anti-ALCAM, D′-anti-CA19-9, F′-anti-osteopontin, J′-anti-CA15-3, K′-anti-CEA, L′-anti-CA-125, M′-anti-PSA.

7.2.6 DNA Spotting and Multiplex Functionalization

Eight-plex chips were created by microspotting 4FB-functionalized DNA strands onto HyNic-functionalized microring resonator chips. Each chip had rings spotted with the eight DNA sequences in the sequential order B, C, D, F, J, K, L, and M which was then repeated three times. Spotting was accomplished with a Nano eNabler spotting system from BioForce Nanosciences (Ames, IA) using a concentration of ~100 µM 4FB-modified DNA in 100 mM PBS buffer pH 6.0 mixed in a 1:1 ratio with DMSO, to slow solvent evaporation. After spotting, the drops of solution were dried on a hot plate (~80 °C) for five minutes. The chips were then incubated in a saturated humidity chamber overnight to enable rehydration of DNA and subsequent surface reaction without the presence of DMSO. Overnight incubation proved to be important in obtaining reproducible results from chip to chip. Following the overnight incubation, chips were then immersed into Starting Block. The blocking solution was immediately removed by rinsing with water, and then the chips were again reimmersed into fresh Starting Block. Chips were left in Starting Block for >3 hours and then immersed in PBST for 1 hour. After PBST immersion, chips were removed and briefly rinsed with water and air dried.

To add multiple antibodies to the chip surface, all of the DNA-antibody conjugates were diluted in a single mixture to 5 µg/mL (except for L′-anti-CA-125, which was used at 1 µg/mL) with PBST as the diluting buffer. To each eight-plex, DNA-functionalized microchip, ~10-15 uL

of DNA-antibody conjugate mixture was added to the surface of each chip. The chips were enabled to incubate overnight to enable maximum binding of the DNA-antibody conjugates to the DNA capture probes on the surface. This overnight binding step also proved to be important to ensuring that each microring sensor had a uniform surface density of antibody, thus enabling more consistent ring-to-ring and chip-to-chip responses. Following overnight binding, the chips were immersed in Starting Block. They were loaded into a fluidic cartridge, with care taken to make sure the chips stay wet during the loading process to avoid denaturing the antibodies on the surface. Typically, we used a method whereby the chips could be loaded while immersed in water to prevent any drying of the surface.

7.2.7 Antibody Biotinylation

To biotinylate all eight secondary antibodies, each antibody was initially buffer exchanged to 100 mM PBS pH 7.4 via a Zeba spin column. Antibodies solutions had a 20-fold molar excess of 20 mM NHS-PEG_4-biotin added and were then allowed to incubate for 2 h at room temperature. For the anti-AFP secondary, it was determined that a 5-fold molar excess gave optimal antibody activity, and for the anti-osteopontin secondary, it was found that a 50-fold molar excess resulted in the best signal amplification for osteopontin. Excess NHS-PEG_4-biotin was removed by buffer exchange using Zeba spin filter columns. The ALCAM secondary antibody came as a pre-biotinylated polyclonal antibody sample, so it was not treated any further.

7.2.8 Bead Exchange

As discovered previously,[8] when using the streptavidin-coated 100 nm beads, it is of critical importance to buffer exchange the beads immediately before use. This exchange removes free streptavidin which would otherwise rapidly diffuse to the surface and outcompete the beads for biotin binding sites. To exchange the beads, 100 μL of 5 mg/mL streptavidin-coated beads were diluted to 1 mL PBST-SB buffer and centrifuged at 10,000 *g* for ~8 min. The bead pellet was held at the bottom of the tube off to the side using a rare-earth magnet while the supernatant was completely removed. The beads were then resuspended in 1 mL of PBST-SB buffer by pipetting the solution up and down ~50 times with the tube bottom remaining in contact with the magnet.

Pipetting has proven to be the most effective method of resuspension as compared to using a vortex mixer or sonication. After resuspending, the beads were aliquoted into 100 μL aliquots and then spun down at 10,000 *g* for ~4 min and stored for later use. Just prior to use in an experiment (~5 minutes prior), these stored beads were placed adjacent to the rare-earth magnet for several minutes to enable the concentration of any resuspended beads. Then the supernatant was completely removed as just described, and the beads were resuspended in 500 μL PBST-SB to make a nominally 100 μg/mL solution of magnetic beads. Where highly reproducible concentrations were needed between experiments, the absorbance at 275 nm (via NanoDrop) was used. Typically a 100 μg/mL solution will have a A_{275} absorbance of ~0.2 with the 1 mm pathlength on the NanoDrop.

7.2.9 Layer-by-layer Antibody Buffer Exchange

Prior to utilizing the anti-PE (biotin) and anti-biotin (PE) antibodies for the layer-by-layer antibody amplification step, it was necessary to buffer exchange these antibodies into PBST-SB. This was done using Zeba spin columns, and this step eliminated the bulk refractive index shift measured by the microring resonator sensors due to components in the original storage buffer.

7.2.10 Eight-plex Antigen Analysis

Human serum samples were analyzed after diluting to 50% in PBST-SB. This dilution was used to enable the cold non-degassed serum samples to be mixed with room temperature, degassed buffer preventing any bubble formation; it also diluted the serum solution to make its viscosity more amenable to flowing through a microfluidic channel. For antibody evaluation and amplification strategy testing, 10% FBS solutions spiked with antigens were used. Initial testing was done with antigens diluted in pure buffer.

To perform an analysis of a sample using an eight-plex chip, the microring resonator chip was loaded in the fluidic cartridge and registered. PBST-SB was used as the running buffer and was flowed over the surface for ~5 minutes. Then the sample was introduced and flowed over the chip for 30 minutes. Then buffer was flowed over the chip to rinse off any non-specifically bound proteins for 20 minutes. Then a mixture of each biotinylated secondary antibody at a

concentration of 1 µg/mL was flowed over the chip for 15 minutes. A 5 minute rinse with buffer occurred next and was followed by the signal amplification step. For bead amplification, a buffer-exchanged solution with 100 µg/mL beads was flowed over for 15 minutes. For the layer-by-layer antibody amplification, 1 µg/mL anti-biotin (PE) was first flowed over the surface followed by a brief buffer rinse, and then 2 µg/mL anti-PE (biotin) was next flowed over followed by a brief buffer rinse. This process was repeated up to 6 times to amplify the secondary antibody signal. Solution flow rate was 30 µL/min for all steps.

7.3 Results and Discussion

7.3.1 Antibody Screening

The initial step in creating an eight-plex assay was to first acquire antibodies that would bind selectively and specifically to the antigens of interest with sufficient sensitivity. As we demonstrated in previous results,[9] the microring resonator system is an effective way to screen for antibody binding kinetics as well as for antibody sandwich pairs. Thus, after screening for antibodies against the antigens AFP, ALCAM, CA125, CA15-3, CA19-9, CEA, osteopontin, and PSA, we could then create an eight-plex chip that contained all eight antibodies as DNA-antibody conjugates. Since each chip has 24 active sensors, each of the eight antibodies was deposited onto three microring sensors. The eight-plex chip was then tested to determine if any antibody cross-reactivity existed. We did this testing by sequentially flowing a high concentration of each antigen in buffer (1 µg/mL for AFP, ALCAM, CEA, osteopontin, PSA and 1 kU/mL for CA125, CA15-3, CA19-9) over the chip followed by sequential addition of each secondary antibody.

Figure 7.1 shows the sensor responses to each of the antigens as they are individually added. Each graph shows the responses for each of the 24 sensors with each sensor colored according to the antibody with which it was functionalized. The title above each graph indicates which antigen was added, and the line next to the title indicates the color associated with each antibody (anti-AFP = black, anti-ALCAM = red, anti-CA19-9 = cyan, anti-osteopontin = blue, anti-CA15-3 = purple, anti-CEA = orange, anti-CA125 = yellow, anti-PSA = green). As indicated in Figure 7.1, each sensor responds specifically according to the antibody it was functionalized with. The only instance of noticeable interference occurs with the anti-CA19-9

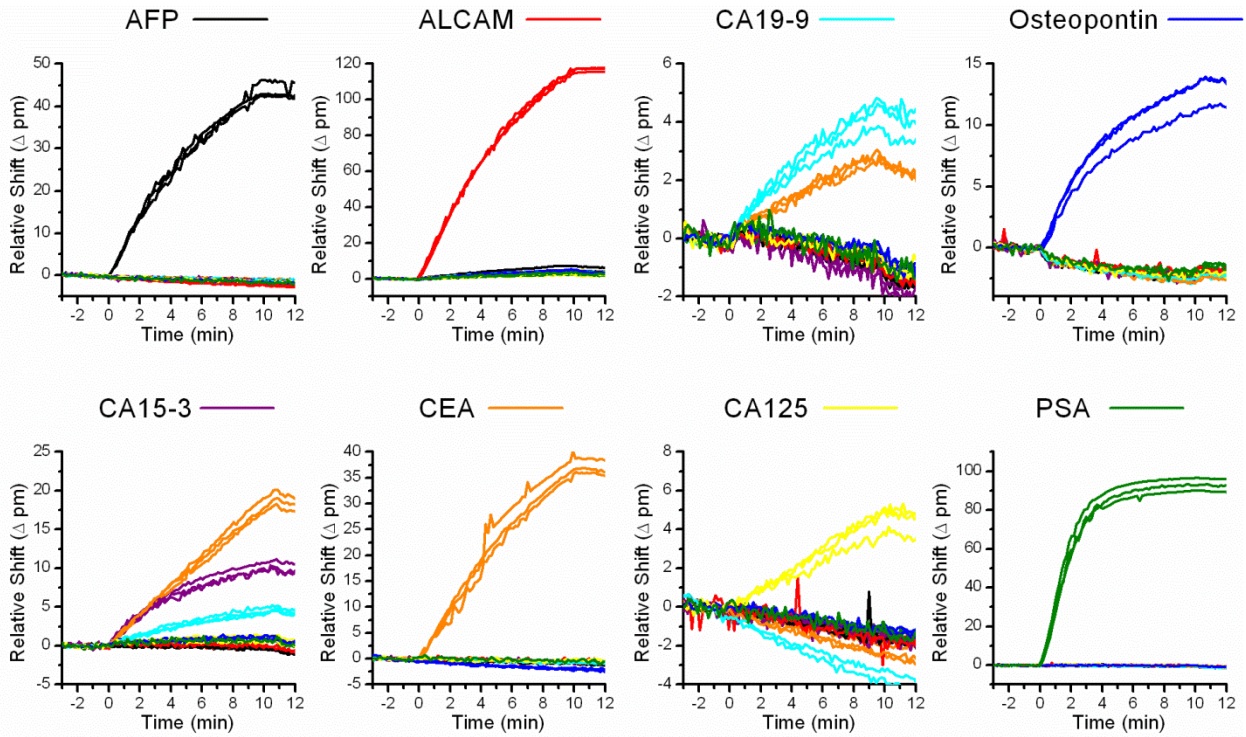

Figure 7.1 Responses for 8-plex chips following addition of 1 µg/mL antigen (or 1 kU/mL for CA19-9 CA125, CA15-3). Each graph shows the responses of all the microring sensors upon addition of the specified antigen as indicated by the title above each graph. The colored line next to the antigen name indicates the color used to represent the sensor trace corresponding to the sensors functionalized with antibodies against that particular antigen.

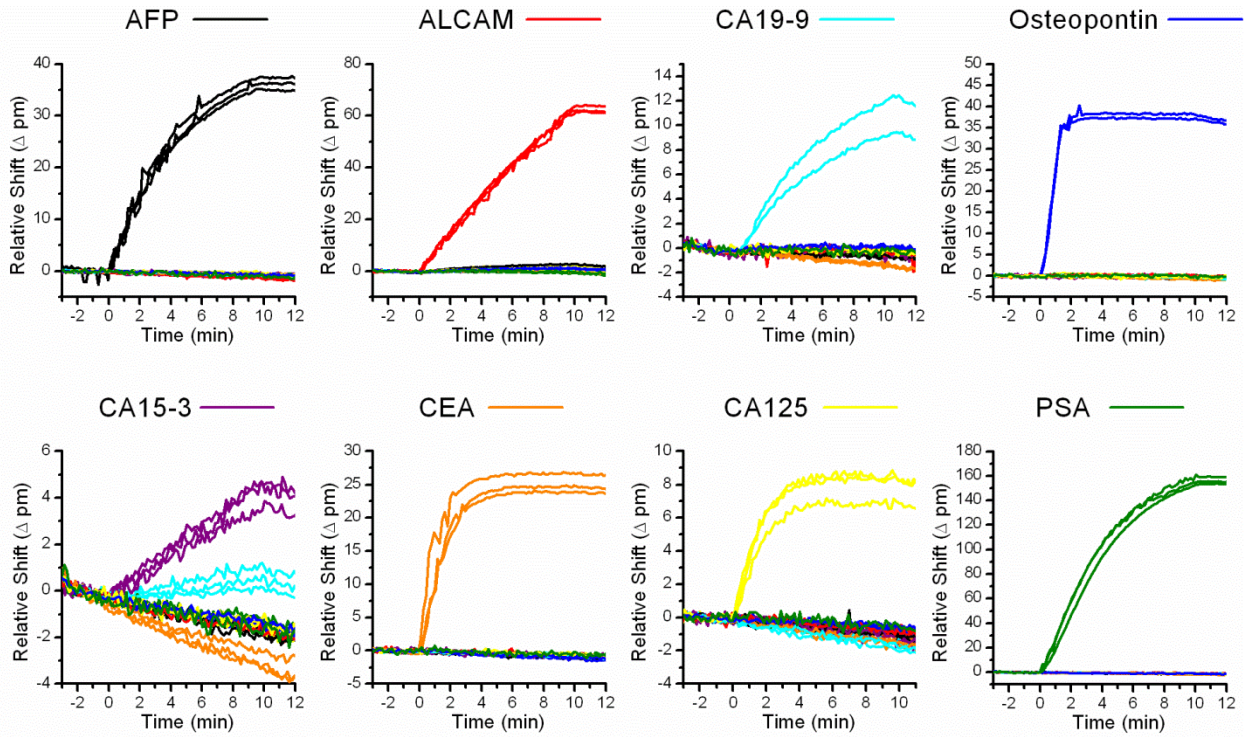

Figure 7.2 Responses for 8-plex chips following addition of 1 µg/mL secondary antibody. Each graph shows the responses of all the microring sensors upon addition of the specified antigen as indicated by the title above each graph. The colored line next to the antigen name indicates the color used to represent the sensor trace corresponding to the sensors functionalized with antibodies against that particular antigen.

sensors and the anti-CA15-3 sensors. Following addition of 1 kU/mL CA19-9, the appropriate anti-CA19-9-functionalized rings (cyan) respond, but so do the anti-CEA-functionalized rings (orange). Similarly, addition of 1 kU/mL of CA15-3 results in responses from not only the antiCA15-3-functionalized sensors (purple), but also from the anti-CEA- and anti-CA19-9-functionalized sensors. This inter-antigen interference has two potential sources. First, it could be due to contaminant antigens in the "pure" standards. Because the standards for CA19-9, and CA15-3 are derived from purified extracts from human cell lines, it is not unlikely that multiple cancer biomarkers could be present in a given standard. The CA15-3 antigen product information sheet even indicates that CA19-9 and CA125 are present, albeit at less than 1-2% of the CA15-3 concentration; however, the presence or absence of CEA is not indicated. The second potential source of cross-reactivity is from the off-target binding of the capture antibody (e.g. anti-CA19-9 binding to CA15-3). This is also not totally surprising given that CA19-9, CA125, and CA15-3 are all mucin-family glycoproteins derived from cancer cells.[24-27] Thus, the probability of binding epitope overlap between these antigens is non-negligible.

To further determine the specificity of the interactions, we examined the results from secondary antibody binding. As shown in Figure 7.2, addition of 1 ug/mL of each secondary antibody (in sequence, following addition of antigens) results in a specific response from the appropriate sensors. In the case of CA19-9, there is no further response from the anti-CEA functionalized rings following addition of anti-CA19-9. This suggests that the response of the anti-CEA rings following addition of CA19-9 was not the result of off-target CA19-9 binding. As an additional control (data not shown), we tested the addition of CA19-9 to sensors functionalized with anti-CEA followed directly by addition of the anti-CEA secondary. In this case, after addition of the anti-CEA secondary, a specific response occurred on the anti-CEA rings confirming that the response of the anti-CEA sensors to CA19-9 is very likely the result of CEA present in the CA19-9 "standard." The response of the anti-CEA rings to the addition of CA15-3 proved to have the same cause as the addition of CA19-9. In this case as well, the addition of the anti-CA15-3 secondary antibody generated no secondary response (as seen in Figure 7.2), but addition of anti-CEA (data not shown) did generate a specific response. Apparently, both the CA15-3 and CA19-9 antigen standards are contaminated with CEA at a fairly high level. Although CEA contamination in CA15-3 and CA19-9 could be problematic, it should be correctable once the levels of CEA present are well characterized. This indicates the

importance of having a label-free detection system to accurately determine the source of cross-reactivity and how it can be corrected.

On the other hand, the response of the anti-CA19-9-functionalized rings to the addition of CA15-3 displayed a different source of cross-reactivity. Unlike the anti-CEA rings, the anti-CA19-9 rings still respond upon addition of 1 μg/mL anti-CA15-3 secondary antibody. This suggests that CA15-3 is binding to the anti-CA19-9 antibodies. Even after changing the antibodies used as capture and detection antibodies for CA19-9, CA15-3 would still bind to the anti-CA19-9-functionalized rings, and the subsequent addition of anti-CA15-3 would generate a response. Furthermore, addition of anti-CA19-9 secondary following addition of anti CA15-3 did not generate a measureable response (data not shown) indicating that it was not CA19-9 contaminants that generated the response. Thus, it became apparent that all of our measurements with the anti-CA19-9-functionalized rings would measure both the CA15-3 and CA19-9 content in the sample. However, because the anti-CA15-3-functionalized sensors are still specific towards CA15-3, our sensor chip can be designed to measure CA15-3 levels and the combined levels of CA15-3 plus CA19-9. This is not too different than the tests for PSA which measure both free PSA and total PSA (free PSA + complexed PSA).[28] Again, this level of characterization and understanding of a multiplexed assay would not be easily achieved with an end-point only measurement. Instead, having the real-time, label-free data makes it possible to thoroughly evaluate and characterize the source of interference between antigens.

7.3.2 Background Signal Reduction with Beads

Following the determination of which antibodies to use for the eight-plex analysis as well as their characterization, we proceeded to determine the sensitivity of our measurement using signal amplification techniques. Our initial tests utilized the streptavidin-coated microspheres to bind to the biotinylated secondary antibodies. Unfortunately, initial results showed that there was a significant amount of non-specific signal. Figure 7.3A shows the addition of beads to a sensor chip where all eight antigens were added to the chip followed by all eight secondary antibodies. In this case, the anti-ALCAM secondary was the only biotinylated secondary flowed across the chip, and thus the anti-ALCAM sensors should be the only ones that respond upon addition of streptavidin-coated beads. As expected, the red traces show the relatively high response of the

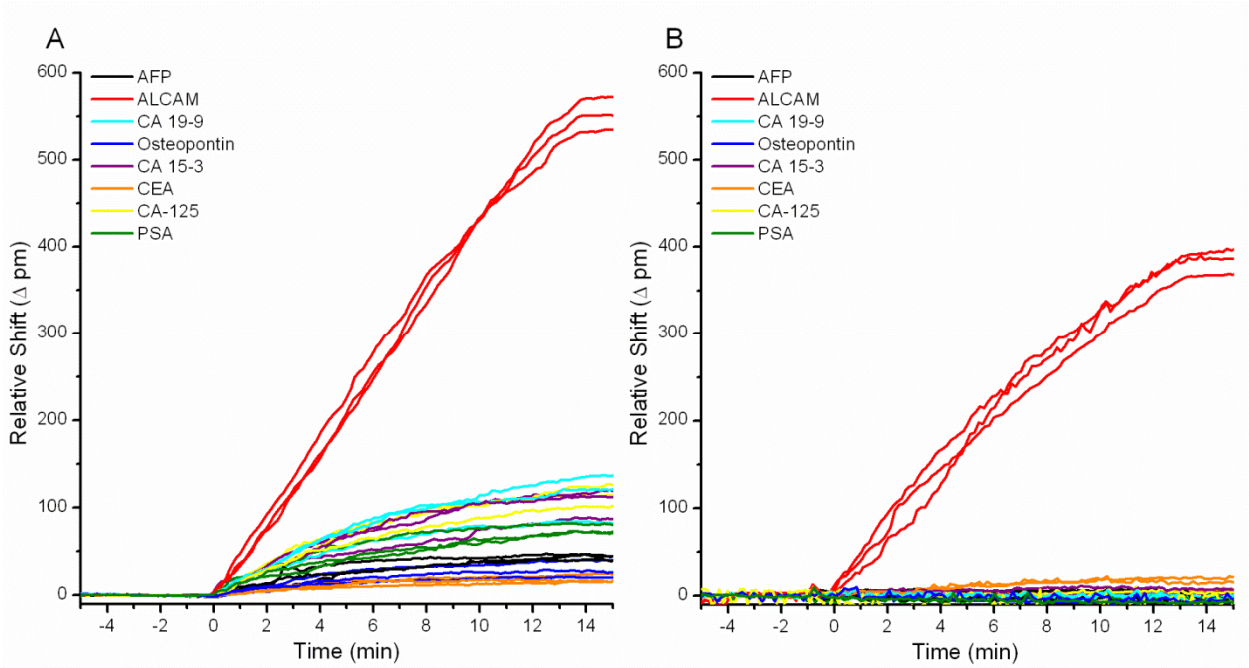

Figure 7.3 Graphs from an eight-plex sensor chip showing the streptavidin-coated bead response following addition of all eight antigens followed by the appropriate secondary antibodies. In this example, only the anti-ALCAM antibody is biotinylated. (A) Response before optimizing the parameters for non-specific binding. (B) Response when the antigens are added within a serum matrix and the running buffer contains 1% Starting Block.

anti-ALCAM-functionalized rings giving a ~550 pm shift. However, almost all of the other rings also respond even though no biotinylated secondaries specific to those rings were added to the chip. Obviously the 30-100 pm background shift significantly reduces the signal to noise ratio of the system and raises the limit of detection for each antigen.

To overcome this limitation, we explored the source of the non-specific bead sticking and determined that main culprits were the biotinylated secondary antibodies. In general, the non-specific bead sticking only occurred when a biotinylated secondary antibody was added, regardless of whether there was target antigen added or not. Thus, our challenge was to reduce the non-specific binding of the biotinylated secondary antibodies. We found the best method for preventing non-specific binding was to perform antigen analyses out of a serum sample and to use blocking protein in the running buffer. By flowing a serum sample across the chip, the high concentration protein components of the serum sample functioned remarkably well in blocking the surface from the non-specific adsorption of biotinylated secondary antibodies—even though each chip surface was previously blocked with a commercial blocking solution (Starting Block). Fortunately, since the project goal is to measure biomarker levels in serum samples, this requirement is met without any additional changes to our assay design. We also found than the addition of 1% Starting Block to the running buffer significantly reduced non-specific binding of biotinylated secondaries. Figure 7.3B shows what happens when the same experiment as in Figure 7.3A is run, but where the ALCAM is initially dissolved in a serum sample (fetal bovine serum) and Starting Block is used in the running buffer. As can be seen in the graph, the amount of non-specific binding of beads was drastically reduced.

7.3.3 Layer-by-layer Amplification Method

Although the streptavidin-bead binding method has proven successful as a signal amplification technique,[8] it still suffers from two major drawbacks. First, the binding of beads to the microring surface increases the noise present in the signal. Second, to obtain consistent responses between different runs, the beads must be buffer exchanged just prior to being flowed over the chip surface to minimize the amount of free streptavidin in solution. This streptavidin is presumably desorbed from the beads as they incubate in solution. Due to the ability of free streptavidin to diffuse faster than the 100-nm streptavidin-coated beads, the free streptavidin can

outcompete the beads for binding sites at the surface, thus reducing the overall signal amplification of the assay. Because of the requirement to exchange beads just prior to use (within 5 minutes), it makes it more challenging to automate the analysis of dozens of human serum samples which is the goal of this project.

As an alternate signal amplification strategy, we utilized a multilayer antibody amplification method. This method is similar to what our group[29] and Gauglitz et al.[30] have used for creating protein multilayers on a surface. Except for a limited use (one bilayer of fluoresecence amplification) by Anderson et al. in a Luminex assay,[31] this technique has not been applied to amplifying the signal of an immunoassay in the literature. Figure 7.4 illustrates this methodology on the microring resonator silicon surface. Initially, the microring silicon surface is functionalized with a capture antibody. Then primary antigen binding and biotinylated secondary antibody binding occur according to standard sandwich assay protocols. For the amplification step, instead of adding streptavidin-coated beads, an anti-biotin antibody conjugated to phycoerythrin (anti-biotin PE) is added to bind to the biotinylated secondaries. Because biotinylated secondaries usually have two or more biotins per antibody, it is possible to add two or more anti-biotin antibodies. Next, biotinylated anti-PE (anti-PE biotin) antibodies are added that bind to the anti-biotin PE antibodies. As a further amplification, anti-biotin PE can be added again, with amplification due to the multiple biotins per anti-PE biotin antibody. This process can be repeated over and over to grow a large, branching antibody agglomeration on the surface.

Figure 7.5 shows some data illustrating the layer-by-layer amplification process. The figure shows amplification based on the initial binding response to 1 µg/mL AFP (red trace) and 10 ng/mL CEA (black trace). Upon addition of the antigen at t = 7 min, a noticeable response is generated from AFP binding. However, the CEA concentration is low enough that no noticeable response is visible from the CEA binding. Similarly, at t = 18 min when the biotinylated secondary antibodies are added, there is a visible shift from the anti-AFP functionalized ring, but not from the anti-CEA functionalized ring. Subsequently, anti-biotin (PE) and anti-PE (biotin) are added alternately. Each additional step increases the signal for the anti-AFP trace. For the anti-CEA trace, only a small response is measured at first, but then this response grows into a significant (~50 pm) shift by the end of the amplification steps. Importantly, it is noted in both processes that the additional signal for each step of the amplification process increases with each step. Thus the anti-biotin (PE) addition at t = 40 min generates a larger shift than what is seen at

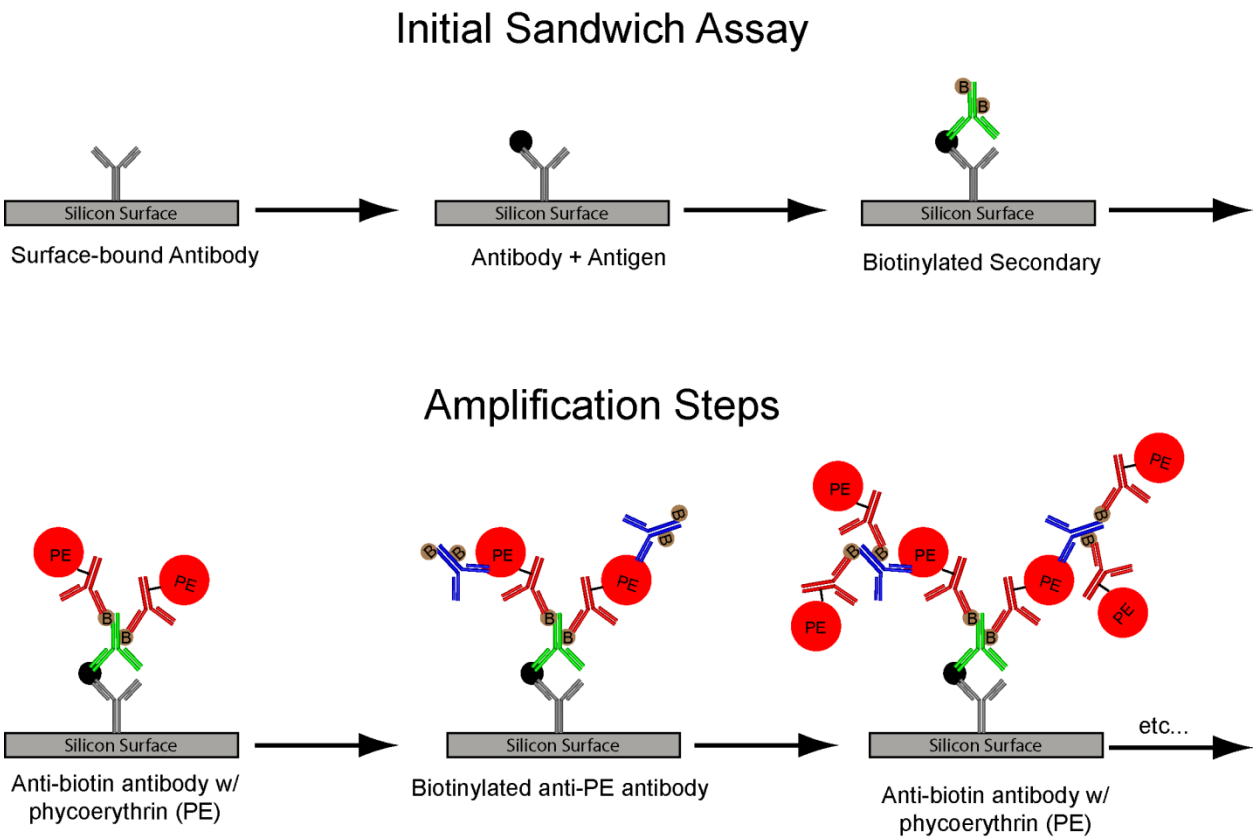

Figure 7.4 Layer-by-layer amplification strategy. The first steps involve primary binding of antigen followed by addition of the biotinylated secondary antibody. The amplification step involves using a pycoerythrin (PE) conjugated anti-biotin antibody binding to the biotinylated secondary antibody. This then is followed by addition of a biotinylated anti-PE antibody. This process can be repeated multiple times to create a branching antibody agglomeration.

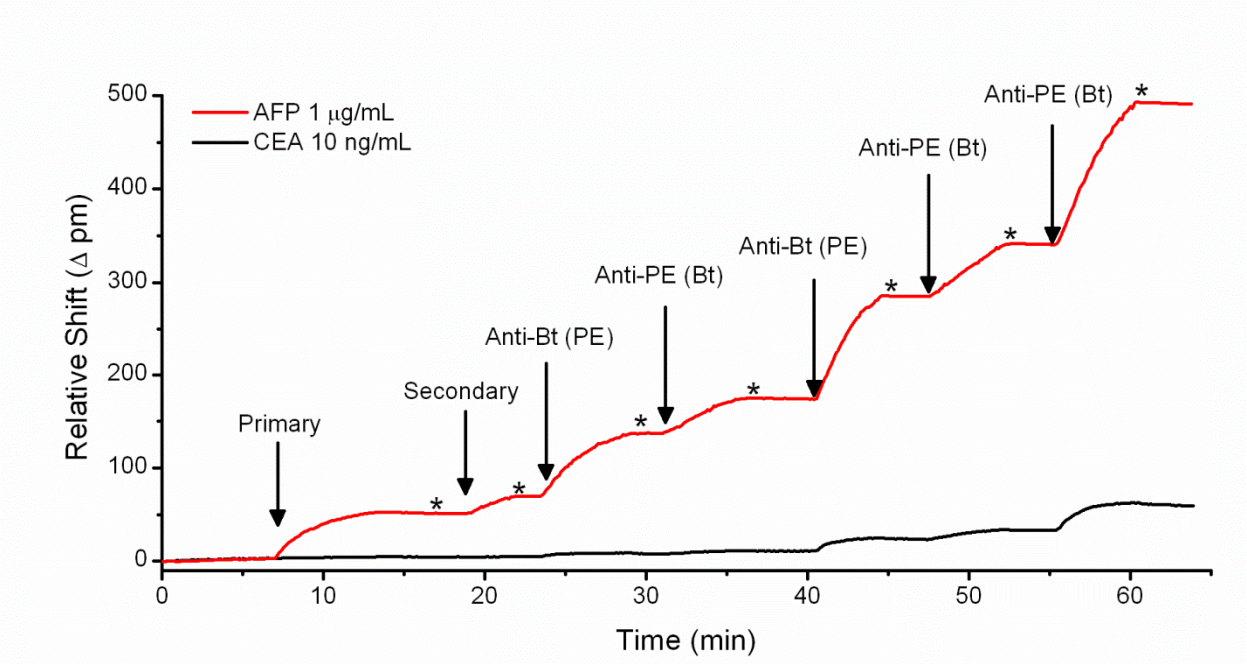

Figure 7.5 Real-time data showing layer-by-layer amplification with AFP (red) and CEA (black). Antigen is added at t = 7 min and a noticeable response is generated from AFP but not CEA. Biotinylated secondaries are added at t = 18 min, and again the anti-AFP sensor shows signal, but not the anti-CEA sensor. Subsequently, anti-biotin (PE) and anti-PE (biotin) are added alternately. This amplification steps increase the signal for the AFP trace significantly and give a visible signal for the CEA trace.

the t = 24 min addition. This indicates that not only are additional antibodies being added, but that there is an exponential growth factor leading to more signal with each layer. This effect is more pronounced in the CEA trace than in the AFP trace, presumably because the AFP trace has a greater surface coverage of antibodies and thus there are larger steric hindrances to antibody layer-by-layer growth at a particular antigen binding site than would be present at the lower density CEA sensor.

In comparing this method to the streptavidin-bead method, we found that amplification responses tend to be similar, but that additional signal can be gained in the layer-by-layer approach by adding additional amplification steps. In contrast, adding time to the bead-binding amplification step usually results in diminishing marginal returns. In addition, there is no requirement for consistent reagent preparations (exchanging the beads) just prior to the amplification step. Finally, the baseline noise of the sensors is lower when using the antibodies as opposed to the beads. Thus, with all these reasons combined, it has proven advantageous to use the layer-by-layer approach rather than the bead approach.

7.3.4 Human Serum Analysis from Cancer Patients

After developing the amplification method that we would use for the cancer biomarker analysis, we proceeded to do some preliminary analyses on six different human blood samples. Five of these samples were commercially available blood serum samples from cancer patients with ovarian, breast, colorectal, lung, and prostate tumors. The sixth sample was a fresh plasma sample collected from a healthy donor. Figure 7.6 shows the sensor plots showing the addition of the serum sample at t = 5 minutes followed by rinsing with buffer at t = 35 min and then adding the secondary antibody at t = 55 min. The amplification step proceeds after the secondary antibody step, and each analysis used a total of 6 amplification bilayers (12 steps altogether) over the course of 30 minutes. Since most of the information is contained within the amplification step, Figure 7.7 was plotted to show only the amplification step with each ring re-zeroed at the time the amplification step started.

Although at the information presented at the current time is not quantitative, it does provide some interesting insights into cancer biomarker levels among various patients. One obvious insight from Figure 7.7 is that in all of the samples, CEA and ALCAM levels are readily

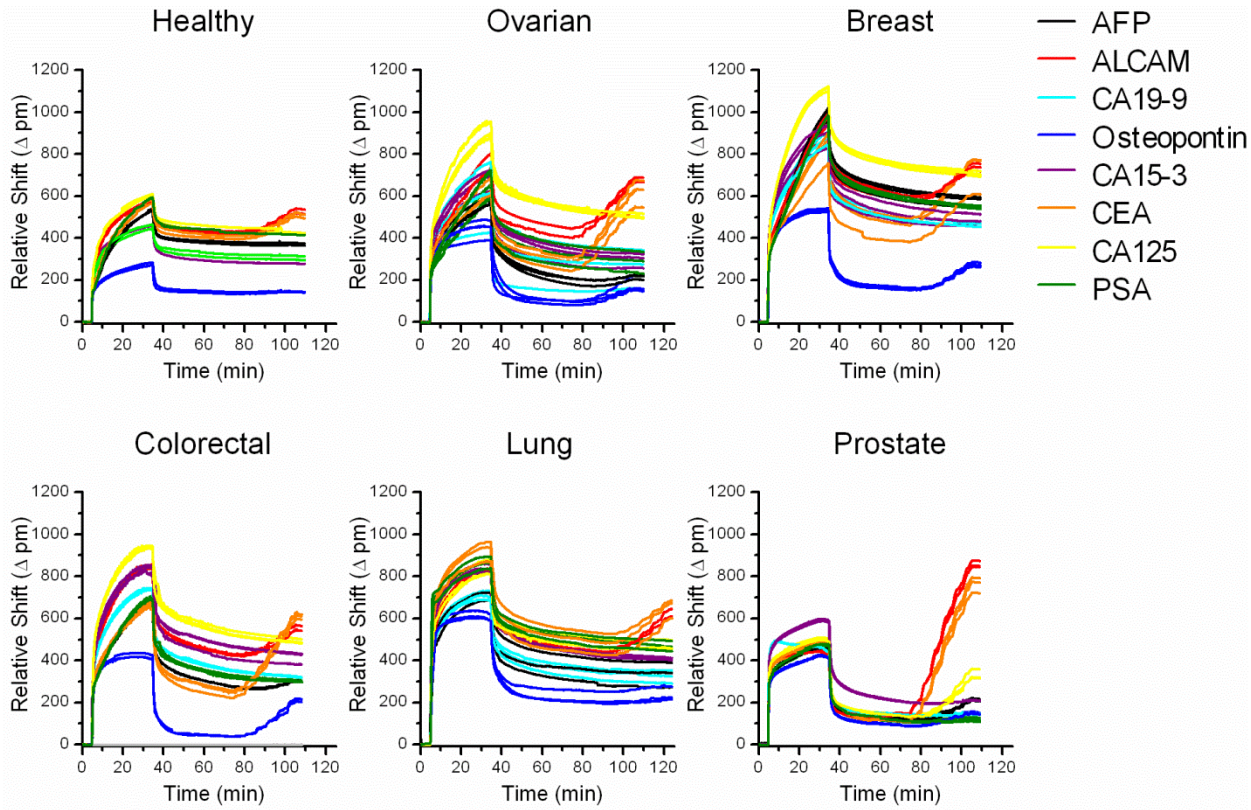

Figure 7.6 Real-time data showing the addition of human serum at t = 5 minutes followed by a buffer rinse at t = 35 minutes. Biotinylated secondaries are added at t = 55 minutes and then the layer-by-layer amplification begins at t = 60 minutes. The title above the graph indicates the tumor type found in the particular patient from which the blood serum was obtained. The healthy patient was actually a freshly collected sample of blood plasma from a healthy donor.

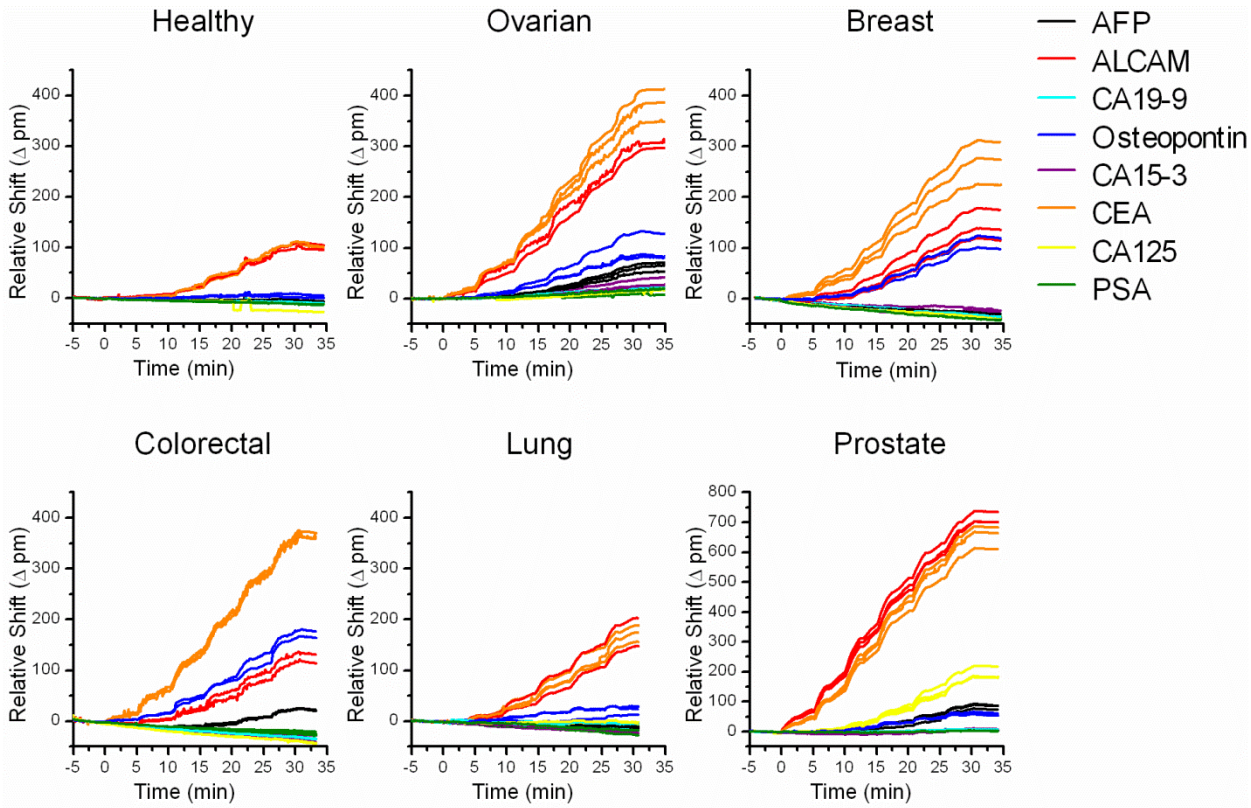

Figure 7.7 Layer-by-layer amplification data from Figure 7.6 with each microring sensor data re-zeroed at the point of addition of the amplification antibodies.

detected for all patients—including the healthy donor. Another observation is that the biomarkers associated with a particular disease are not always the ones to be elevated significantly in a particular patient's sample. For example the patient with prostate cancer would be expected to have elevated levels of PSA, and he could be clinically diagnosed or treated based on that PSA level. However, Figure 7.7 indicates that PSA levels are almost unobservable. This low level of PSA is confirmed by patient history information provided from the serum vendor indicating that that PSA levels were ~0.1 ng/mL—a level far below standard basal PSA levels, and near the detection limit for our assay. However, CEA, ALCAM, AFP, and CA-125 are significantly higher in the prostate cancer patient sample than in all the other patient samples (note that the scale is different in the prostate cancer patient data than in all the other 5 data plots). Similarly, the breast cancer patient has near negligible levels of CA15-3, a breast cancer biomarker, whereas the ovarian cancer patient serum sample has the highest levels of CA15-3 as compared to the other five. Meanwhile, the ovarian cancer patient sample has osteopontin levels that aren't quite as high as the osteopontin levels in the breast cancer patient sample even though osteopontin is a purported ovarian cancer biomarker.

In addition to the observations for the tertiary amplification portion of the biomarker detection, it was also interesting to observe the primary binding upon addition of the serum samples. For example, in the ovarian, breast, and colorectal patient samples, the anti-CA125 functionalized rings (yellow) all gave the highest response in the serum binding region of the curve, but subsequent addition of secondary antibody and amplification steps revealed no significant CA125 response. Clearly, something in the human serum samples was binding to the anti-CA125-coated rings that was not CA125. Similarly, in the prostate cancer patient sample, the anti-CA19-9 rings display an initial shift upwards following addition of the serum sample and then proceed to gradually slope downward, in contrast with the behavior of the other sensors. Although these responses aren't necessarily indicative of cancer biomarkers, it is possible that they are the result of other protein-protein interactions from unknown components in the blood serum samples. Future work may reveal whether these observations are significant or not, but at present, it is important to note that this behavior is only observable on a label-free, real-time platform such as microring resonators.

7.4 Conclusions and Future Work

Moving forward on the multiplex analysis of human serum samples, several tasks will need to be accomplished. First of all, a standard calibration curve will have to be established for each antigen using the multilayer amplification strategy. This can be accomplished in a multiplex fashion for several of the anlaytes for which there is not interference. However, for CA19-9, CEA, and CA15-3, the antigen calibration curves will likely have to be calculated independently to avoid interference effects from cross-reactivity and antigen contamination between standards. To verify the reproducibility of the calibration on multiple chips, it will be important to run the calibration curve with several replications to ensure that similar results can be derived from multiple microsensor chips.

Following generation of calibration curves, human serum analysis can proceed. To verify the calibration curve, standard addition will be performed on several samples to see how the values from a calibration analysis compare to that of standard addition. For a quantitative analysis this will be important to ensure that matrix effects from serum samples do not overly skew the results of the biomarker analysis. Additionally, several standard single-plex enzyme-linked immunosorbent assays (ELISAs) will probably have to be utilized for some of the samples to verify the results with another commercially available method. However, since running 8 ELISAs on a single sample will be rather tedious (hence the need for multiplex chip analysis), probably only a few samples will be analyzed.

After analyzing ~50 human serum samples, it will then be important to understand how to process the data for clinical utility. Although it may be true that our specific panel of antibodies will not be the right selection to fully develop a diagnostic test for making clinical decisions, it will be important to understand how to treat multiplexed data derived from such a panel. As a result, we will use statistical methods such as principal component analysis[32, 33] or hierarchical clustering[23, 34] to analyze the data as has been used previously.

Overall, this initial work has demonstrated the feasibility of designing an eight-plex biomarker panel and then performing eight-plex biomarker analysis on human serum samples. In the near future multiple human serum samples will be analyzed via the biomarker chips illustrating the potential of microring resonators for multiplexed diagnostics design and implementation.

7.5 References

(1) Etzioni, R.; Urban, N.; Ramsey, S.; McIntosh, M.; Schwartz, S.; Reid, B.; Radich, J.; Anderson, G.; Hartwell, L. *Nature Reviews Cancer* **2003**, *3*, 243.

(2) Petricoin, E. F.; Ardekani, A. M.; Hitt, B. A.; Levine, P. J.; Fusaro, V. A.; Steinberg, S. M.; Mills, G. B.; Simone, C.; Fishman, D. A.; Kohn, E. C.; Liotta, L. A. *The Lancet* **2002**, *359*, 572-577.

(3) Sawyers, C. L. *Nature* **2008**, *452*, 548-552.

(4) Arnaud, C. H. In *Chem. Eng. News*; American Chemical Society, 2011; Vol. 89, pp 40-43.

(5) Boja, E. S.; Jortani, S. A.; Ritchie, J.; Hoofnagle, A. N.; Tezak, Z.; Mansfield, E.; Keller, P.; Rivers, R. C.; Rahbar, A.; Anderson, N. L.; Srinivas, P.; Rodriguez, H. *Clin. Chem.* **2011**, *57*, 560-567.

(6) Hsu, H.-Y.; Joos, T. O.; Koga, H. *Electrophoresis* **2009**, *30*, 4008-4019.

(7) Rissin, D. M.; Kan, C. W.; Campbell, T. G.; Howes, S. C.; Fournier, D. R.; Song, L.; Piech, T.; Patel, P. P.; Chang, L.; Rivnak, A. J.; Ferrell, E. P.; Randall, J. D.; Provuncher, G. K.; Walt, D. R.; Duffy, D. C. *Nat Biotech* **2010**, *28*, 595-599.

(8) Luchansky, M. S.; Washburn, A. L.; McClellan, M. S.; Bailey, R. C. *Lab Chip* **2011**, *11*, 2042-2044.

(9) Washburn, A. L.; Gomez, J.; Bailey, R. C. *Anal. Chem.* **2011**, *83*, 3572-3580.

(10) Washburn, A. L.; Luchansky, M. S.; Bowman, A. L.; Bailey, R. C. *Anal. Chem.* **2010**, *82*, 69-72.

(11) Sturgeon, C. *Clin. Chem.* **2002**, *48*, 1151-1159.

(12) Schiemann, U.; Günther, S.; Gross, M.; Henke, G.; Müller-Koch, Y.; König, A.; Muders, M.; Folwaczny, C.; Mussack, T.; Holinski-Feder, E. *Cancer Detect. Prev.* **2005**, *29*, 356-360.

(13) Szymendera, J.; Nowacki, M.; Szawlowski, A.; Kamińska, J. *Dis. Colon Rectum* **1982**, *25*, 46-52.

(14) Wang, J. Y.; Tang, R. P.; Chiang, J. M. *Dis. Colon Rectum* **1994**, *37*, 272-277.

(15) Rhea, J. M.; Molinaro, R. J. *MLO. Med. Lab. Obs.* **2011**, *43*, 10-18.

(16) Mor, G.; Visintin, I.; Lai, Y.; Zhao, H.; Schwartz, P.; Rutherford, T.; Yue, L.; Bray-Ward, P.; Ward, D. C. *Proc. Natl. Acad. Sci. U. S. A.* **2005**, *102*, 7677-7682.

(17) Berger, A. C.; Meszoely, I. M.; Ross, E. A.; Watson, J. C.; Hoffman, J. P. *Ann. Surg. Oncol.* **2004**, *11*, 644-649.

(18) Andriole, G. L.; Crawford, E. D.; Grubb, R. L., III; Buys, S. S.; Chia, D.; Church, T. R.; Fouad, M. N.; Gelmann, E. P.; Kvale, P. A.; Reding, D. J.; Weissfeld, J. L.; Yokochi, L. A.; O'Brien, B.; Clapp, J. D.; Rathmell, J. M.; Riley, T. L.; Hayes, R. B.; Kramer, B. S.; Izmirlian, G.; Miller, A. B.; Pinsky, P. F.; Prorok, P. C.; Gohagan, J. K.; Berg, C. D.; the PLCO Project Team *N. Engl. J. Med.* **2009**, *360*, 1310-1319.

(19) Kulasingam, V.; Zheng, Y.; Soosaipillai, A.; Leon, A. E.; Gion, M.; Diamandis, E. P. *Int. J. Cancer* **2009**, *125*, 9-14.

(20) Iqbal, M.; Gleeson, M. A.; Spaugh, B.; Tybor, F.; Gunn, W. G.; Hochberg, M.; Baehr-Jones, T.; Bailey, R. C.; Gunn, L. C. *IEEE J. Sel. Top. Quantum Electron.* **2010**, *16*, 654-661.

(21) Washburn, A. L.; Gunn, L. C.; Bailey, R. C. *Anal. Chem.* **2009**, *81*, 9499-9506.

(22) ***Caution!*** *Piranha solutions are extraordinarily dangerous, reacting explosively with trace quantities of organics*.

(23) Fan, R.; Vermesh, O.; Srivastava, A.; Yen, B. K. H.; Qin, L.; Ahmad, H.; Kwong, G. A.; Liu, C.-C.; Gould, J.; Hood, L.; Heath, J. R. *Nat. Biotechnol.* **2008**, *26*, 1373-1378.

(24) Budiu, R. A.; Mantia-Smaldone, G.; Elishaev, E.; Chu, T. J.; Thaller, J.; McCabe, K.; Lenzner, D.; Edwards, R. P.; Vlad, A. M. *Cancer Immunology Immunotherapy* **2011**, *60*, 975-984.

(25) Cappelli, G.; Paladini, S.; D'Agata, A. *Tumori* **1999**, *85*, S19-S21.

(26) Lan, M. S.; Bast, R. C.; Colnaghi, M. I.; Knapp, R. C.; Colcher, D.; Schlom, J.; Metzgar, R. S. *Int. J. Cancer* **1987**, *39*, 68-72.

(27) Duffy, M. J.; Shering, S.; Sherry, F.; McDermott, E.; O'Higgins, N. *Int. J. Biol. Markers* **2000**, *15*, 330-333.

(28) Kuriyama, M.; Kawada, Y.; Arai, Y.; Maeda, H.; Egawa, S.; Koshiba, K.; Imai, K.; Yamanaka, H. *Jap. J. Clin. Oncol.* **1998**, *28*, 661-665.

(29) Luchansky, M. S.; Washburn, A. L.; Martin, T. A.; Iqbal, M.; Gunn, L. C.; Bailey, R. C. *Biosens. Bioelectron.* **2010**, *26*, 1283-1291.

(30) Spaeth, K.; Brecht, A.; Gauglitz, G. *J. Colloid Interface Sci.* **1997**, *196*, 128-135.

(31) Anderson, G. P.; Taitt, C. R. *Sensor Lett.* **2008**, *6*, 213-218.

(32) Alvarez-Chaver, P.; Rodriguez-Pineiro, A. M.; Rodriguez-Berrocal, F. J.; Garcia-Lorenzo, A.; Paez de la Cadena, M.; Martinez-Zorzano, V. S. *Journal of Proteomics* **2011**, *74*, 874-886.

(33) OuYang, D.; Xu, J.; Huang, H.; Chen, Z. *Appl. Biochem. Biotechnol.* **2011**, *165*, 148-154.

(34) Dwek, M. V.; Alaiya, A. A. *Br. J. Cancer* **2003**, *89*, 305-307.